Single-molecule analysis and engineering of chitinase A from *Serratia marcescens*

Serratia marcescens 由来 chitinase A の １分子解析とエンジニアリング

Akasit VISOOTSAT

Doctor of Philosophy

Department of Functional Molecular Science

School of Physical Sciences

The Graduate University for Advanced Studies, SOKENDAI

Summary of Doctoral Thesis

Chitin is a water-insoluble polysaccharide which is a component of the shells of crustaceans, the exoskeleton of insects, and the cell walls of some fungi. Chitin degradation is not only important in nature but also industrial applications such as biomass conversion. Chitinase A from the Gram-negative bacterium *Serratia marcescens* (*Sm*ChiA) is a processive enzyme that hydrolyzes crystalline chitin as it moves linearly along the substrate surface. In a previous study, the catalytic activity of *Sm*ChiA against crystalline chitin was found to increase after the tryptophan substitution of two phenylalanine residues (F232W and F396W), located at the entrance and exit of the substrate-binding cleft of the catalytic domain, respectively. In this thesis, I used single-molecule analysis to understand the mechanism of this high-catalytic-activity mutant of *Sm*ChiA, and further improved chitin hydrolytic activity by generating a new mutant with engineering approach based on bioinformatics, site-saturation mutagenesis, and robot-based automated screening.

The thesis consists of 5 Chapters. Chapter 1 is a general introduction of chitin and chitinase. In Chapter 2, single-molecule fluorescence imaging and high-speed atomic force microscopy were applied to understand the mechanism of high-catalytic-activity F232W/F396W mutant. A reaction scheme including processive catalysis was used to reproduce the properties of *Sm*ChiA wild-type and F232W/F396W, in which almost all of the kinetic parameters were experimentally determined. High activity of F232W/F396W mutant was caused by a high processivity and a low dissociation rate constant after productive binding. An alignment of amino acid sequences of 258 *Sm*ChiA-like proteins revealed that tryptophan, not phenylalanine, is predominant at the corresponding positions (Phe-232 and Phe-396 for *Sm*ChiA).

In Chapter 3, I optimized the design of degenerate oligonucleotides for saturation mutagenesis and robot-based automated screening procedures for *Sm*ChiA purification and activity measurement. In order to optimize the degenerate oligonucleotides for saturation mutagenesis, the loss-of-function mutant of green fluorescence protein, GFPMut3-Y66H, was used for introducing NNN or NNB codon. Although the ratios of gain-of-function mutant (H66Y) in both colony counting and deep sequencing analysis were similar, I found that the ratios of nucleotides in the primers were highly biased among the suppliers. Biases for NNB were less severe than for NNN. The supplier which showed the least-bias for NNB primer was

used in Chapter 4.

The alignment in Chapter 2 also showed that several amino acid residues in both catalytic domain and chitin binding domain are not conserved in *Sm*ChiA. This strongly suggests that although *Sm*ChiA is the most studied processive chitinase, the amino acid sequence is not optimized for high hydrolytic activity. In Chapter 4, I combined bioinformatics, site-saturation mutagenesis, and robot-based automated screening to further improve chitin hydrolytic activity of F232W/F396W mutant. This method allows us to reduce the number of mutation trials and shortens the screening time. As a result, I identified F232W/F396W/S538V mutant. Interestingly, valine was not found in the multiple sequence alignment at the Ser538 residue. This result indicates that my method can generate an active mutant that cannot be achieved only by the introduction of mutation which is dominant in the multiple sequence alignment.

Finally, I conclude this thesis in Chapter 5. My results highlight the importance of the combination of single-molecule analysis with biochemical analysis to understand the mechanism of *Sm*ChiA. Although I successfully identified F232W/F396W/S538V which shows high catalytic activity, the single-molecule analysis and the structure analysis will be required in the future to understand its mechanism in detail. This thesis will be helpful for understanding the kinetic mechanisms and further improvement of the crystalline chitin hydrolytic activity of *Sm*ChiA mutants. Moreover, both the single-molecule analysis and protein engineering method developed in this thesis will be also applicable to other enzymes.

Table of Contents

List of Figures

List of Tables

List of Abbreviations

AFM: atomic force microscopy

AuNP: gold (Au)-nanoparticle

BLAST: basic local alignment search tool

CBD: chitin-binding domain

CD: catalytic domain

cryo-EM: cryogenic electron microscopy

DDA: degree of deacetylation

DMSO: dimethyl sulfoxide

DTT: dithiothreitol

FaXa: factor Xa

fps: frame per second

GFP: green fluorescence protein

GlcNAc: *N*-acetyl glucosamine

HS-AFM: high-speed atomic force microscopy

IPTG: isopropyl-D-1-thiogalactopyranoside

IVA: in vivo assembly

k_{cat}: turnover number

K_d: dissociation constant

K_m: Michaelis constant

k_{off}: dissociation rate constant

k_{off}^{NP}: non-productive dissociation rate constant

k_{off}^{P}: productive dissociation rate constant

k_{on}: binding rate constant

k_{on}^{NP}: non-productive binding rate constant

k_{on}^{P}: productive binding rate constant

k_{pc}: processive catalysis rate constant

k_{tr}: translational velocity

LB : Luria-Bertani

LED: light-emitting diode

Ni-NTA: nickel-nitrilotriacetic acid

NMR: nuclear magnetic resonance

n^{NP}: the number of nonmoving molecules

n^{P}: the number of moving molecules

OBD: optical beam deflection

*Of*Chi-h: *Ostrinia furnacalis* chitinase-h

PCR: polymerase chain reaction

PID: proportional-integral-derivative

SB: super broth

S.D.: standard deviation

SLiCE: seamless ligation cloning extract from *Escherichia coli*

SOC: super optimal broth with catabolite repression

*Sm*ChiA: *Serratia marcescens* chitinase A

TIM barrel: triosephosphate isomerase barrel

TIR: total internal reflection

TIRF: total internal reflection fluorescence

WT: wild-type

Chapter 1

General Introduction

1. Chitin

Chitin is one of the most abundant polysaccharides found in nature, only secondary to cellulose. Chitin is a water-insoluble polysaccharide and it is mostly found as crystalline microfibrils that form the structural components in the shells of crustaceans, the exoskeleton of insects, and the cell walls of some fungi[1-3] with the fact that it does not appear in organisms producing cellulose. Similar to cellulose, the natural function of chitin is that of a structural polysaccharide, but its properties are different from cellulose. Chitin is a linear polymer chain of β-1,4 glycosidic linkages of the monomer *N*-acetyl glucosamine (GlcNAc) which are rotated 180° to each other (Figure 1A). Chitin has the disaccharide N,N′-diacetylchitobiose [$(GlcNAc)_2$] as the structural subunit[4]. Similar to cellulose, chitin can be found in three various polymorphic forms (α, β, and γ) which differ in their polymeric chain arrangement[5] (Figure 1B). In α-chitin, the polymeric chains are arranged anti-parallel to each other. In β-chitin, they are arranged parallel to each other. The polymeric chains of γ-chitin are randomly arranged. The source of α-chitin mainly comes from crustaceans such as crabs and shrimps, whereas β-chitin is from squids and tube worms, and γ-chitin is derived from loligo[6].

The characteristic features of chitin, namely degree of deacetylation (DDA) and molecular mass, can vary with the method of isolation, the process, and origin of chitin. The DDA index is used to differentiate between chitin and chitosan. If the DDA index is less than 50%, it is then defined as chitin and if the DDA index is greater than 50%, it is defined as chitosan. DDA index is an important factor which relates to the properties of chitin such as solubility, flexibility, polymer conformation, and viscosity.

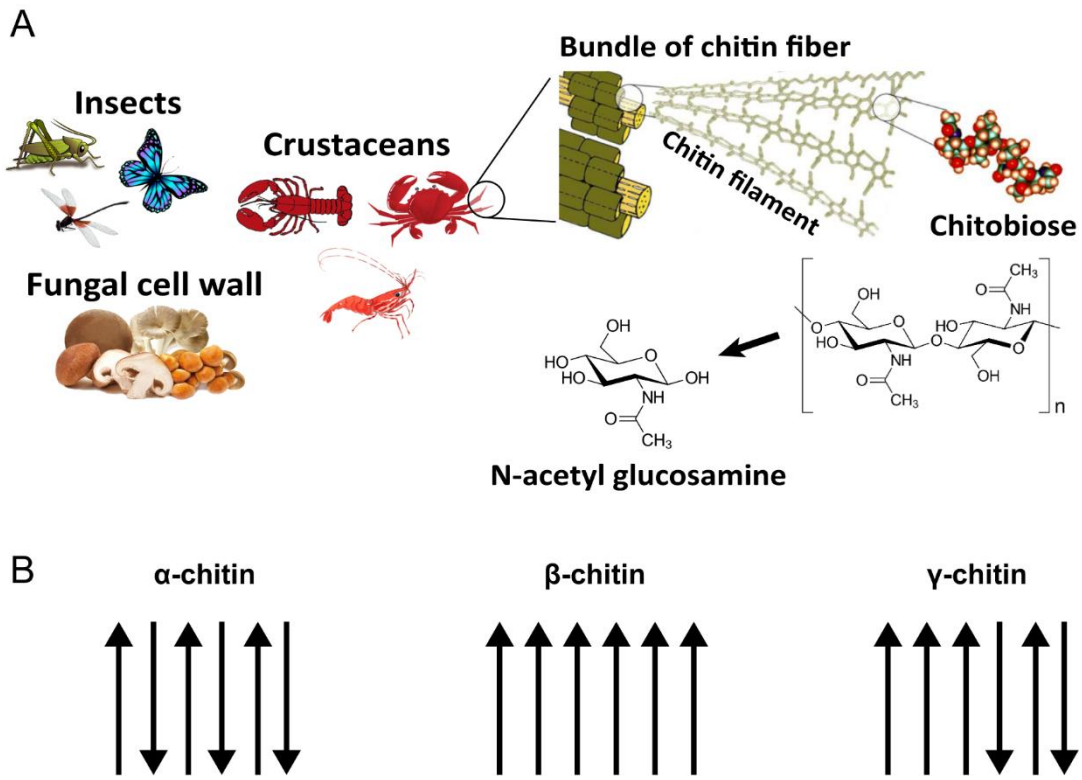

Figure 1. Schematic model of chitin (A) The schematic shows the sources of chitin and its monomeric subunit. The images in Figure1A are obtained from the sites on Google with the copyright download and modified with Adobe Illustrator. (B) The schematic representation of three different polymeric configurations (α, β, and γ) of chitin.

Every year, approximately 8 million tons of crustaceans shell waste are produced worldwide[7]. Different from cellulose, chitin is not only the carbon-source but also the nitrogen-source of biomass conversion in both nature and industry[4, 7]. As a nitrogen-containing compound, chitin has potential applications in agriculture, biotechnology, and the pharmaceutical industry[7-8]. For this reason, chitin degradation is important in nature as well as industrial applications. Due to its stable crystalline structure, chitin is very durable, only decomposing at very high temperatures and under high pressure[9]. However, there are many naturally occurring organisms that possess the ability to degrade chitin under mild conditions (room temperature and normal pressure) by using enzymes called chitinases[10].

2. Chitinase

Chitinases are widespread in nature and have been found in bacteria, fungi, plants, invertebrates (mainly nematodes, insects, and crustaceans) and all classes of vertebrates[11]. The roles of chitinases in these organisms are diverse and subject to intensive investigation. In vertebrates, chitinases are usually part of the digestive tract or the immune system. In insects and crustaceans, chitinases are associated with the need for partial degradation of the old cuticle, and their secretion is controlled by a complex hormonal mechanism. In plants, a major part of the inducible defense response against exogenous pathogenesis is the secretion of proteinase inhibitors, glucanases, and chitinases. Chitinases in fungi are thought to have autolytic, nutritional, and morphogenetic roles[11]. Finally, bacteria secrete chitinases that catalyze the degradation of chitin, the products of which act as a source of energy[12].

According to the CarbohydrateActive enZYmes database (CAZY: http://www.cazy.org/)[13], chitinase is classified in the glycoside hydrolase family 18 (EC 3.2.1.14) and functions to catalyze the hydrolysis of the β-1,4 glycosidic bonds of chitin. This hydrolysis occurs on the crystalline surface of chitin. The primary product of chitinases in the GH18 family is chitobiose, which is converted to GlcNAc by a family GH20 beta-N-acetylhexosaminidase (known as chitobiase)[14]. The GH family 18 chitinases are retaining and maintaining the configuration of the β-anomeric carbon of substrates in products (Figure 2). This mechanism is attained by a substrate-assisted type of double displacement hydrolytic mechanism involving a simply DXDXE (D-aspartic acid, E-glutamic acid, and X-any other amino acids) motif in the catalytic site[15-16]. The general mechanism of GHs is known to involve two carboxylic acid residues, one serving as the general acid/base and the other as the nucleophile that stabilizes the oxazolinium intermediate in retaining enzymes or serves as a water-activating base in inverting enzymes. In GH family 18, the substrate and not necessarily a second carboxylic acid residue plays the

nucleophilic role, while the highly conserved glutamate residue positioned above the TIM barrel serves as the general acid/base, protonating the glycosidic oxygen and initiating the cleavage of the glycosidic bond.

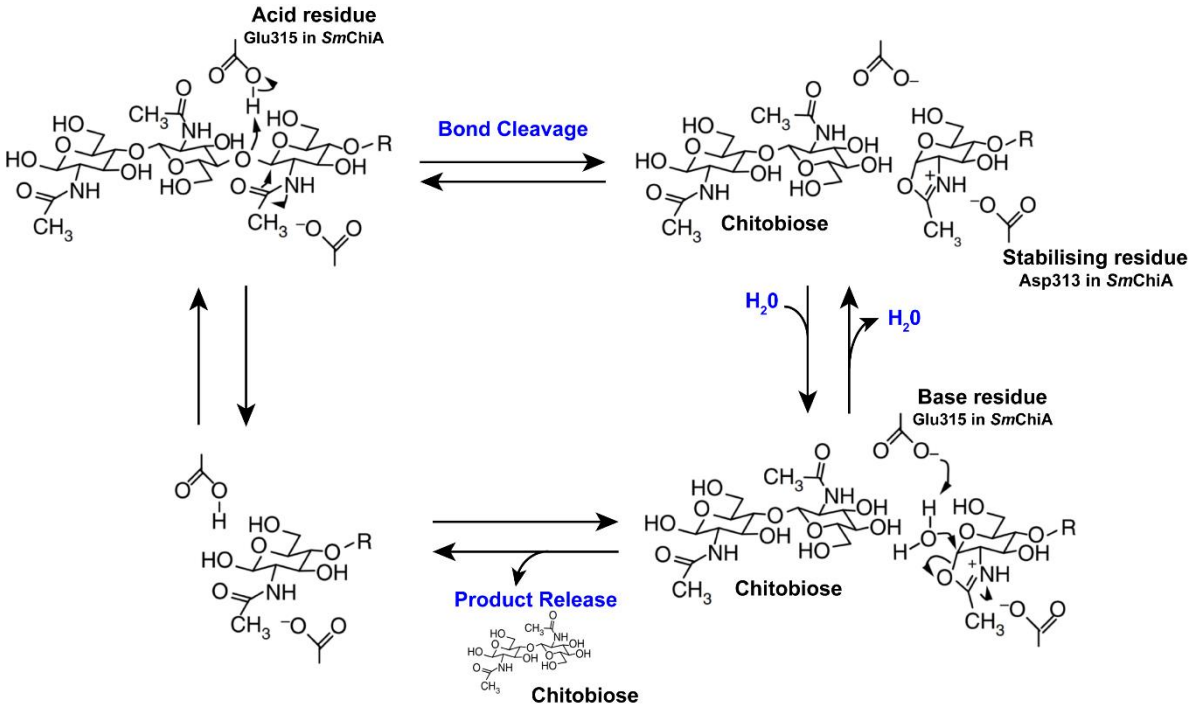

Figure 2. Mechanism of hydrolysis of glycosidic bonds in chitin (modified from Akihiko Nakamura et al.[17], *Nat. Commun.*, 2018).

The chitinases of the bacterium *Serratia marcescens* are a well-known model for the study of chitin degradation. When grown on chitin, this bacterium secretes two exo-processive chitinases, *Sm*ChiA and *Sm*ChiB, that hydrolyze β-1,4 glycosidic bonds from the reducing and non-reducing ends, respectively, a non-processive endo-chitinase (*Sm*ChiC), a chito-oligosaccharide-attacking N-acetylhexosaminidase (Chitobiase; *Sm*CHB), and a lytic polysaccharide monooxygenase (*Sm*LPMO10A; also known as "CBP21")[18]. *Sm*ChiA, *Sm*ChiB, and *Sm*ChiC belong to the GH family 18 and share the $(\beta/\alpha)_8$ TIM-barrel structure of the

catalytic domain. According to the previous reports, *Sm*ChiA is the most powerful enzyme among the *S. marcescens* chinolytic enzymes in the hydrolysis of crystalline chitin[19-20].

*Sm*ChiA is a linear molecular motor enzyme that hydrolyzes chitin from the reducing end and works in the extracellular environment without the need for ATP. *Sm*ChiA is composed of two domains: a catalytic domain (CD) and a chitin-binding domain (CBD)[12] (Figure 3). Both the substrate-binding cleft of CD and the chitin-binding surface of CBD have aromatic residues lined along them. These aromatic residues play important roles in both substrate binding and the hydrolytic activity and processivity of the *Sm*ChiA[21-22]. The details information of *Sm*ChiA will be explained and discussed in Chapter 2.

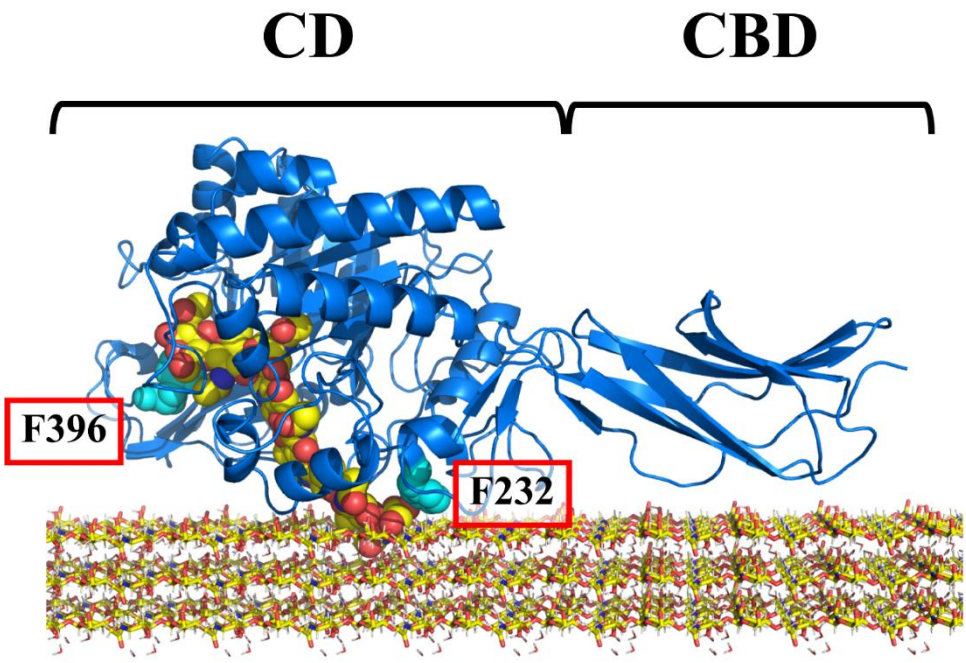

Figure 3. Schematic model of *Sm*ChiA. A crystal structure of *Sm*ChiA (PDB ID: 1CTN) complexed with $(GlcNAc)_7$ (sphere model) and crystalline chitin (stick model). The schematic shows the CD and CBD. Phe-232 and Phe-396 (sphere model, colored with cyan) are located at the entrance and exit of the substrate-binding cleft, respectively.

3. Single-molecule Total Internal Reflection Fluorescence Microscope

To understand the nature of protein function, structure and dynamics are two important factors. In order to solve the structure of the protein, X-ray crystallography, nuclear magnetic resonance (NMR) spectroscopy, and cryogenic electron microscopy (cryo-EM) have been developed[23-25]. On the other hand, optical trap nanometry[26], single-molecule fluorescence microscopy[27-28], and atomic force microscopy (AFM)[24] also have been developed to study the dynamics of the protein. A single-molecule fluorescence microscope is one of the famous methods to visualize the dynamics or the movement of proteins. An important limitation of standard fluorescence microscopy is its resolution limit (~0.2 μm) that is too large to distinguish the single molecule or single complex of the proteins. Recently, several techniques such as deconvolution or confocal microscopy have been developed to improve the resolution. However, these methods still have problems in rapid photobleaching and out-of-focus of light which increases the background of noise. The total internal reflection fluorescence (TIRF) microscope has significantly eliminated this out-of-focus fluorescence problem. It limits the excitation of light to a very thin area near the coverslip which makes it achieve the single-molecule or particle observation and also suppresses the photobleaching of fluorophores in observation area[28].

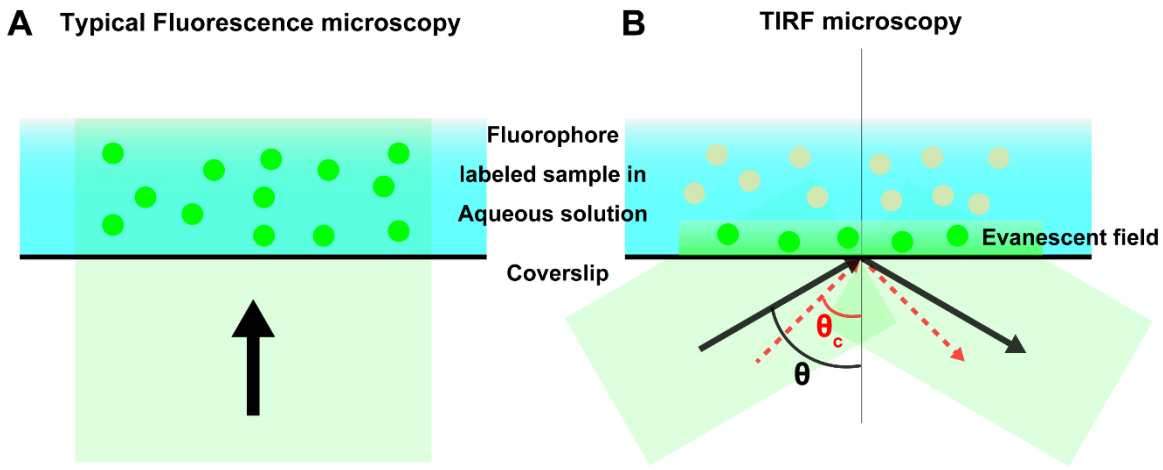

Figure 4. Optical basis of TIRF microscope (modified from Sheng-Wen Chiu et al.[29], *Int. J. Mol. Sci.*, 2011) In the typical fluorescence microscopy (A), the light directly excite the sample. All of the fluorophores are excited (bright green circles). In the TIRF microscopy (B), the excitation light is totally internally reflected from the coverslip/sample interface at the critical angle, θ_c (red). When the excitation light travels at a high incident angle θ (black), which is greater than θ_c, an evanescent field is generated on the opposite side of the interface. Only fluorophores very near to the surface are significantly excited.

The basic properties of optical physics have been applied to a typical fluorescence microscope in order to generate an electromagnetic field to excite fluorophores instead of direct illumination. When light passes through two adjacent materials, one with a higher refractive index (glass coverslip) and another with a lower refractive index (sample solution), it is reflected and refracted depending on the angle of incidence. If a critical angle has been reached, all the light is reflected and the phenomenon called total internal reflection (TIR) occurs (Figure 4). Once the excitation light travels at a high incident angle greater than the critical angle, light no longer passes through the lower refractive index material, the reflection light generates the electromagnetic field, typically called an evanescent field, with the thickness about 100 nm. The fluorophores are excited only inside the evanescent field very near to the glass coverslip and the excitation of the fluorophore molecules far from the glass coverslip is eliminated. This limited excitation significantly reduces the out-of-focus background fluorescence and also

improves the photobleaching problem or prevents harmful light damage from direct illumination as well[28].

4. High-speed Atomic Force Microscopy (HS-AFM)

Although single-molece fluorescence microscopy can observe the dynamic property of proteins, this is the indirect observation, as the protein molecules themselves are invisible[24]. Atomic force microscopy (AFM) has been developed to directly obtain the high-resolution image of biological molecules under the nearest physiological condition without staining or labeling the sample[23-25]. The basic principle of AFM is that a very sharp tip at the end of a flexible micro-cantilever is scanned over the sample surface. The deflections of the cantilever are measured, then the sample stage (cantilever base) is moved in the z-direction to keep constant of the mechanical state of the cantilever at an assigned state through the feedback controller (dynamic proportional-integral-derivative (PID) controller). This feedback controller represses or eliminates the complete detachment of the tip from the sample surface at the slope region of the sample, also called parachuting effect. The height information over many points of the sample is acquired to form an image and visualize by the computer[23-25].

However, the conventional AFM lacks a high temporal resolution of the image which is inappropriate in the analysis of most biological dynamic processes. High-speed AFM (HS-AFM) has been developed to increase the imaging rate of AFM. HS-AFM can observe the image of biological dynamics at sub-100 ms temporal resolution (5-20 frames per second; fps) without disturbing the function of fragile proteins by the interaction of cantilever[23-25]. The setting of the HS-AFM system is shown in Figure 5. The HS-AFM system includes a fast scanner, a feedback controller, fast electronics, and an optical beam deflection (OBD) detector for detecting deflection of this small cantilever. A long working distance objective lens which

is used for the optical microscope is a part of the OBD detector and is also used for viewing the cantilever and sample stage under the optical microscope via a digital camera or a CCD camera. A cantilever chip is installed in the holder in which tip points upward that is opposite to the conventional AFM. A sample stage, connected to the z-scanner and facing opposite to the tip, is placed over the cantilever. An incident laser beam passing through the objective lens is focused onto the small cantilever, and the light reflected back from the cantilever is collected and collimated by the same objective lens and guided to a quadrant-cell Si PIN photodiode. The incident and reflected laser beams are separated using a quarter-wavelength (λ/4) plate and a polarization beam splitter[23, 25].

Another important factor to success imaging with HS-AFM is a substrate surface. The surface of the sample stage should be flat as much as possible because AFM visualizes the sample only one direction perpendicular to the substrate surface. Nowadays, five types of substrate surfaces have been applied for imaging of biological molecules with HS-AFM: (1) bare mica or chemically modified mica, (2) supported lipid bilayers, (3) two-dimensional crystals of streptavidin grown on planar lipid bilayers containing biotin lipid, (4) highly oriented pyrolytic graphite, and (5) DNA origami tiles placed on mica surface. In order to observe the movement of chitinases[23, 25], in this thesis, we immobilized crystalline chitin on the chemically modified mica surface. The mica surface was freshly cleaved and coated with fluoro surf (FS-1010S135-0.5, Fluoro Technology) to modify the hydrophobicity of surface for increasing the affinity to the chitin.

With its high-speed and minimal invasiveness, HS-AFM was used in several studies to directly visualize the dynamics of proteins, protein-protein interaction, and DNA-protein interaction[23-25, 30-31]. In this thesis, we used HS-AFM to observe and analyze the velocity, run length, and moving time of processive chitinase, *Sm*ChiA, on crystalline chitin (Chapter 2).

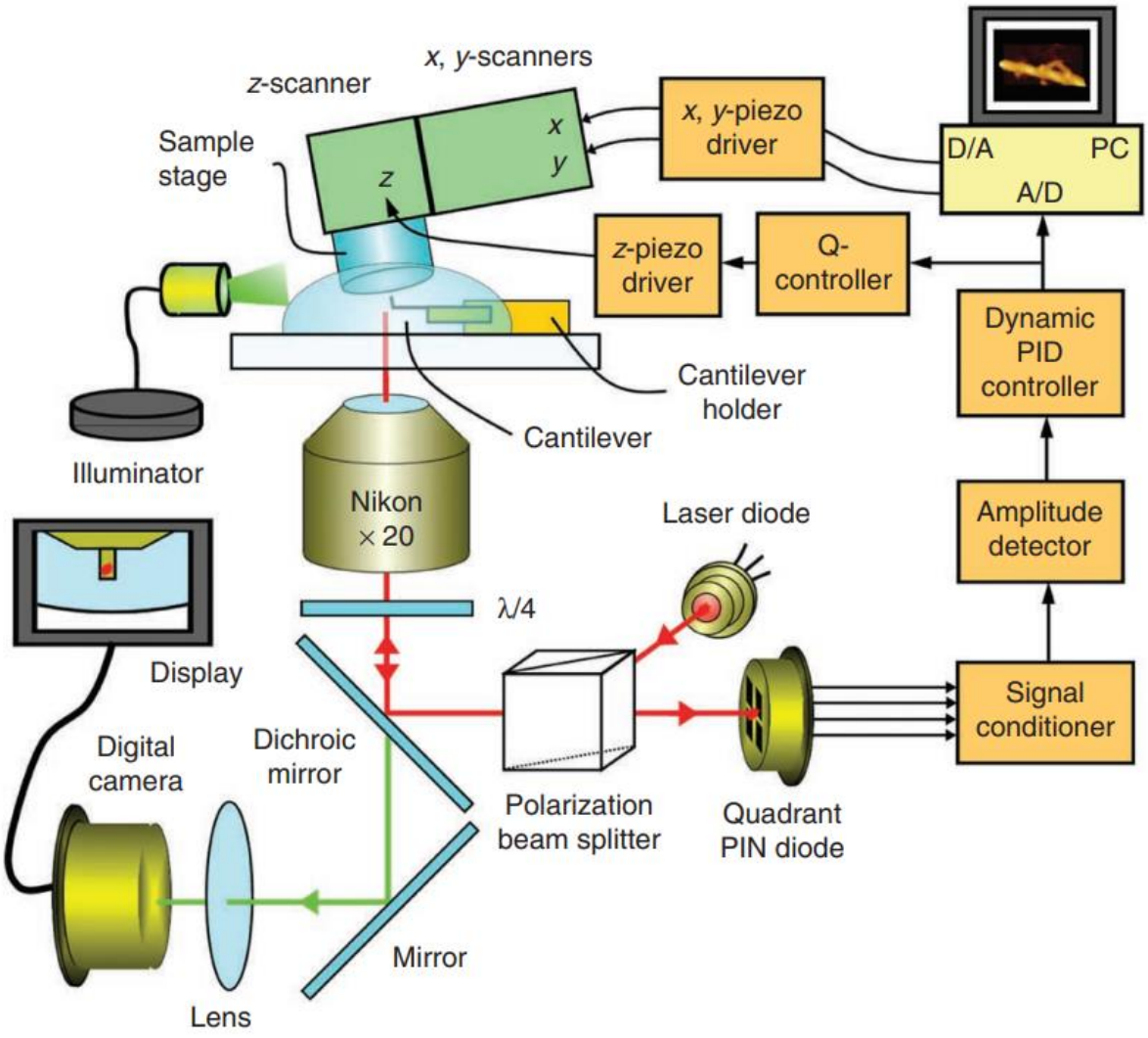

Figure 5. Schematic of the HS-AFM system. (Takayuki Uchihashi et al., *Nat. Protoc.*, 2012)[23]

Chapter 2

Single-molecule analysis of high-catalytic activity mutant F232W/F396W

1. Introduction

Processivity and Processive enzymes

Processive enzymes play important roles in various biological activities such as DNA/RNA synthesis[32-33], cargo transport[34-35], and protein[36-37] and polysaccharide[38-40] degradations. Once processive enzymes bind to their substrates, they can repeat multiple cycles of catalysis without dissociation[41-42]. Processive cellulases and chitinases are well-known examples of the processive enzymes that perform multiple rounds of hydrolytic cleavage of cellulose and chitin, respectively[38-40]. Processivity prevents the dissociation/reassociation process once the enzyme binds to the end of a single polymer chain, thereby reducing the number of times the enzyme rebinds to the end of the same substrate chain[40, 43]. Processive cellulases and chitinases share a similar feature of a long and deep substrate-binding cleft and substrate-binding surface, which contain aromatic amino acid residues[38, 40, 44]. These aromatic residues play an important role in the carbohydrate-protein interaction by which hydrophobic stacking (CH-π interaction) is formed between the aromatic side chain and sugar ring. This interaction is thought to be beneficial for processivity by reducing the sliding energy of the polymer carbohydrate chain[40, 45-48]. Studies on processivity of the cellulases and chitinases using biochemical methods, such as the fluorescence labeling of the substrate [49-50] and ^{14}C-labeled chitin[51], or via the use of biosensors[52] have been performed extensively. However, they often involve complicated procedures and have some limitations. Furthermore, processivity cannot be directly measured using a biochemical assay as it requires interpretations and is usually estimated from the dissociation rate. Recently, single-molecule imaging methods with fluorescence microscopy or high-speed atomic force microscopy (HS-AFM) have been used to directly visualize the processive movement of the enzymes because they are more straightforward than biochemical methods[17, 31, 53-54]. In our previous study[54], we reported not only the processivity but also the

kinetic parameters of *Sm*ChiA-WT (His_6-tagged), including the binding rate constant (k_{on}), dissociation rate constant (k_{off}), translational velocity (k_{tr}), and productive binding ratio, obtained using single-molecule fluorescence imaging.

_Sm_ChiA high-catalytic-activity mutant (F232W/F396W mutant)

Recently, Liu *et al.*[55] reported the structure alignment of the substrate-binding cleft of *Ostrinia furnacalis* chitinase-h (*Of*Chi-h) and *Sm*ChiA. As a result, two different aromatic residues, Phe-232 and Phe-396 for *Sm*ChiA and Trp-225 and Trp389 for *Of*Chi-h, were found in the beginning and end of the cleft (at the chitin-binding subsites 6 and 2)[55-56], respectively, as shown in Figure 6.

In addition, the mutation of these two positions of *Sm*ChiA into those of *Of*Chi-h (F232W/ F396W) showed higher hydrolytic activity against crystalline chitin compared with the *Sm*ChiA WT. However, the details of the mechanism for improved activity have not yet been reported. In the present study, I performed detailed biochemical analysis and single-molecule imaging analysis using fluorescence microscopy and HS-AFM to understand the mechanism by which F232W/F396W mutant showed higher catalytic activity than WT. A reaction scheme including processive catalysis was used to explain the properties of *Sm*ChiA WT and F232W/F396W, in which all the kinetic parameters were experimentally determined. I also performed amino acid sequence alignment of 258 *Sm*ChiA-like proteins and revealed the predominant aromatic amino acid residues responsible for the chitin binding.

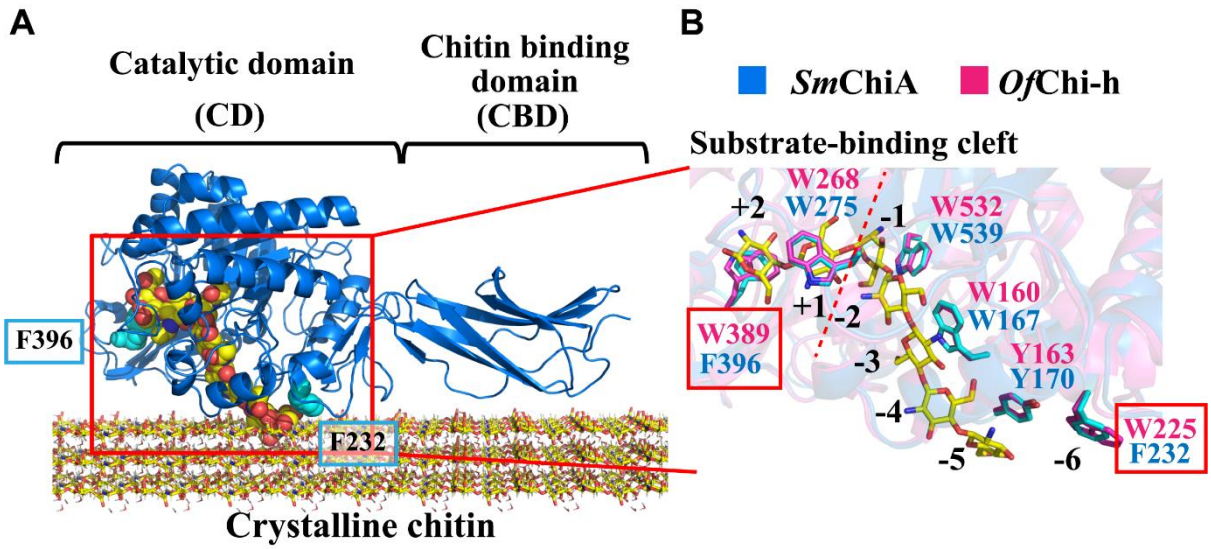

Figure 6. Schematic structure and structural superimposition of *Sm*ChiA and *Of*Chi-h bound with $(GlcNAc)_7$, (A) A crystal structure of *Sm*ChiA complexed with $(GlcNAc)_7$ (sphere model) and crystalline chitin (stick model). The schematic shows the CD and CBD. Phe-232 and Phe-396 (sphere model, colored with cyan) are located at the entrance and exit of the substrate-binding cleft, respectively. (B) Structural superimposition to compare the aromatic residues inside the substrate-binding cleft of *Sm*ChiA (blue and side chain highlighted with cyan; PDB entry 1CTN) and *Of*Chi-h bound with $(GlcNAc)_7$ (pink; PDB entry 5GQB) in side view. The red boxes indicate the two different aromatic residues in *Sm*ChiA and *Of*Chi-h. The numbers (-6 to +2) represent the substrate-binding subsites of *Sm*ChiA according to the standard nomenclature[55-56]. The red dashed lines in (B) show the position of the bond cleavage.

2. Materials and Methods

Preparation of enzymes

The *Sm*ChiA WT gene (including the D415C mutation for fluorescent labeling)[54] in the expression plasmid pET27b with the C-terminal Factor Xa (FaXa) recognition sequence and His_6 tag was used as the template to introduce the F232W/ F396W mutation by PCR. The PCR product was treated with 1 µL of DpnI (New England Biolabs) to reduce the template background at 37 °C for 15 min. After DpnI treatment, 1% agarose gel electrophoresis was performed. The target fragments were extracted and purified using a gel extraction kit (Promega). The purified DNA fragments were ligated using the NEBuilder Assembly Tool (New England Biolabs). The DNA fragments and reagent were mixed at a ratio of 1:1 (v/v) and then incubated at 50 °C for 30 min. After the ligation reaction, the samples were immediately used for transformation using *E. coli* (Tuner™ DE3) as a host. Transformed cells were incubated for 1 hour at 37 °C and spread on an LB plate with 25µg/mL kanamycin. Single colonies were inoculated into 10 mL of LB medium with 25µg/mL kanamycin and incubated overnight at 37 °C and 250 rpm. The plasmid containing the mutant gene was purified from the harvested cell and the sequence was verified. The *E. coli* colonies carrying *Sm*ChiA F232W/F396W or WT expression plasmids were cultured in 10 mL of LB medium with 25µg/mL kanamycin at 37 °C and 250 rpm until $O.D._{600}$ = 1. Then 5 mL of the culture was added to 1 liter of LB medium with 25µg/mL kanamycin in a 3-liter flask and cultured at 37 °C and 130 rpm until $O.D._{600}$ = 1.8. Then the media were cooled on ice water for 10 min, isopropyl-D-1-thiogalactopyranoside (IPTG) was added at a final concentration of 500 µM, and cells were further cultured at 20 °C and 130 rpm overnight. The culture was then centrifuged at 6,000 × *g* for 10 min. Ten times the volume of the cell weight of 50 mM sodium phosphate (pH 7.0), containing 100 mM NaCl, was added and supplemented with protease inhibitor mixture

(cOmplete Mini, EDTA-free, Roche Applied Science). The cell suspension was sonicated on ice for 20 min at 3-s intervals. The disrupted cells were then centrifuged at 4 °C and 30,000 × *g* for 10 min. The supernatant was incubated with Ni-NTA Superflow (Qiagen) and equilibrated with 50 mM sodium phosphate (pH 7.0) containing 100 mM NaCl for 15 min at room temperature under gentle rotation. Then the Ni-NTA resin was packed into an open column and washed with 0 and 50 mM imidazole in 50 mM sodium phosphate (pH 7.0) containing 100 mM NaCl and eluted with 100 mM imidazole in 50 mM sodium phosphate (pH 7.0) containing 100 mM NaCl. The eluted fractions were pooled and concentrated to 500 µL using a 30,000 molecular weight cut-off VIVASPIN Turbo 50 (Sartorius). The sample was then injected into a Superdex 200 10/300 GL column (GE Healthcare) and eluted with 50 mM Tris-HCl (pH 8.0) containing 100 mM NaCl. The fractions were collected at a flow rate of 0.5 mL/min. The eluted fractions were mixed and concentrated to 200 µL using a 30-kDa molecular mass cut-off VIVASPIN Turbo 15 (Sartorius). Protein concentrations were estimated from the absorbance at 280 nm and the molar extinction coefficients (ε_{280} = 107,050 and 118,050 M^{-1} cm^{-1} for WT and F232W/F396W, respectively). The molar extinction coefficients were calculated by using the ProtParam in the Expasy bioinformatics resource portal web service (https://web.expasy.org/protparam/). One hundred microliters of 100 µM sample were incubated with 5 µL of 1 mg/mL FaXa protease (New England Biolabs) and 2 µL of 100 mM calcium chloride at 23 °C overnight to digest C-terminal His_6. Then 10 µL of sodium phosphate (1 M, pH 7.0) was added to the FaXa treated sample, and the sample was centrifuged at 4 °C and 16,000 × *g* for 10 min to precipitate calcium phosphate. The supernatant was applied to the Ni-NTA column to remove the cleaved His_6 tag and undigested samples. The column was washed, and the flow-through fractions were collected with 50 mM sodium phosphate (pH 7.0) containing 100 mM NaCl. The collected fractions were mixed and concentrated to 500 µL

using a 30-kDa molecular mass cut-off membrane (VIVASPIN Turbo 15, Sartorius). DTT at a final concentration of 10 mM was added to the sample to prevent the formation of disulfide bonds between D415C. The sample was then loaded onto a Superdex 200 10/300 GL column (GE Healthcare) with 50 mM sodium phosphate (pH 7.0) containing 100 mM NaCl to remove FaXa protease and DTT. Cy3-maleimide (GE Healthcare) was dissolved in DMSO and mixed with the sample at the same molar concentration as the enzyme before incubating for 1 hour at room temperature. The unreacted Cy3-maleimide was removed using a NAP-5 column (GE Healthcare). The labeling ratio of Cy3 to the enzyme (97% for WT and 83% for F232W/F396W mutant) was calculated from the absorbance at 280 and 550 nm, the molar extinction coefficient of the enzyme as described above, and the Cy3-maleimide (ε_{280} = 12,000 $M^{-1}cm^{-1}$ and ε_{550} = 150,000 $M^{-1}\,cm^{-1}$). The samples were then stored at 80 °C until further use. In this study, WT (D415C-Cy3) and F232W/F396W/D415C-Cy3 are described as WT and F232W/F396W, respectively. Crystalline β-chitin was purified from *Satsuma* tubeworms (*Lamellibrachia satsuma*), as described in a previous study[31](also explained in the Appendix).

Biochemical measurement of chitinase hydrolytic activity

I used a liquid-handling robot, Beckman Coulter Biomek 4000, to measure the hydrolytic activity of all of the samples (blank, WT, and F232W/F396W). The samples were measured in triplicate simultaneously in 96-well plates. The purified enzymes were diluted to 100 nM using 100 mM sodium phosphate (pH 6.0) in a low-protein-binding microtube. In 96-well reaction plates, the diluted enzymes were incubated with crystalline chitin (0–6 mg/mL) at 25 °C for 30 min in a reaction mixture volume of 150 µL (1:1 (v/v) enzyme/substrate ratio) without shaking. The reactions were stopped with 200 µL of the Schales' reagent (500 mM sodium carbonate, 1.5 mM potassium ferricyanide). Insoluble chitin was separated on 96-well 1.2-m hydrophilic

low-protein-binding Durapore membrane filter plates (Merck Millipore). The filtered solution was heated at 95 °C for 15 min, and 100 µL of the samples were transferred to 384-well clear plates. Absorbance at 420 nm was measured using a multimode microplate reader (SpectraMax iD3, Molecular Devices). The amounts of soluble products were calculated from the standard curve with chitobiose. The error bars shown in Figure 7 (A and B) represent the S.D. values of the sextupled experiments.

Biochemical bound fraction analysis

Bound fraction analysis was performed manually using a multichannel pipette. Each measurement condition was measured in triplicate. *Sm*ChiA WT and F232W/F396W were diluted to 100 nM using 100 mM sodium phosphate (pH 6.0) in a low-protein-binding microtube and transferred to a 96-well low-binding plate (Eppendorf). Then 100 nM enzyme was incubated with various concentrations of crystalline chitin (final concentration 0–6 mg/mL) at a 1:1 (v/v) enzyme/substrate ratio at 25 °C for 15 min. The 96-well plate was then centrifuged at 4400 rpm for 15 min at 25 °C. Then 100 µL of the supernatant (unbound fraction) was transferred to a 96-black well plate to measure the fluorescence. The fluorescence intensity was measured using a microplate reader (SpectraMax iD3, Molecular Devices). The excitation and emission wavelengths were 550 and 610 nm, respectively, optimized by fluorescence spectral scanning. The intensities of the blank (no enzyme) were subtracted, and signal intensities were compared with that of the positive control (enzymes without chitin, 100% intensity). The percentages of the bound fractions were calculated, plotted, and fitted using Langmuir's equation. The error bars shown in Figure 7C represent the S.D. values of the triplicate experiments.

Single-molecule fluorescence imaging analysis.

The coverslips used for the single-molecule fluorescence imaging were cleaned with ethanol and sonicated for 10 min before rinsing with MilliQ water and cleaned with 10 M potassium hydroxide overnight to remove any contaminants on the glass surface. Before using, the coverslips were rinsed with MilliQ water. Then 60 µL of 0.01 mg/mL crystalline chitin suspension was spin-coated on the coverslip before placement on the microscope stage. The observation area was determined using bright-field microscopy. Then 20 µL of 50 pM *Sm*ChiA WT or F232W/F396W in 50 mM sodium phosphate (pH 6.0) was dropped onto the coverslip.

For k_{on} and k_{off} analysis, fluorescence images of single molecules were recorded at 4 fps at a laser power of 0.14 µW/µm^2 with localization precisions of 8.6 and 8.4 nm in x and y directions, respectively. After observation, 10 µL of 10 nM WT was dropped onto the coverslip to strain the crystalline chitin. The values of k_{on} were calculated from the number of *Sm*ChiA molecules bound to the single crystalline chitin divided by the *Sm*ChiA concentration, chitin length, and observation time ($M^{-1}\mu m^{-1}\ s^{-1}$). Binding events were counted for 40 s after focusing. The length of the microfibrils was measured from the fluorescence images of crystalline chitin stained with 10 nM WT using ImageJ. The distributions of k_{on} were fitted using double Gaussian functions. The binding time distribution was fitted with the double exponential decay function, according to the following equation,

$$y = \mathrm{a} \cdot \exp(-\mathrm{bt}) + \mathrm{c} \cdot \exp(-\mathrm{dt})$$

where a, b, c, and d are the fitting parameters and t is the binding time. The productive binding ratio was estimated from the ratio of the number of moving molecules and the number of nonmoving molecules in the initial 40-s movies after focusing. The observation condition was

1 μW/μm^2 with 3 fps to improve the moving molecule–finding efficiency. The localization precisions in the x and y directions were 4.3 and 3.8 nm, respectively. For the analysis, I defined moving molecules as the molecules that showed movements larger than 20 nm (~5 times larger than the localization precision) for 3 or more frames. Eight independent images were used to analyze and calculate the average value of the productive binding ratio. Before performing the detailed analysis of the image sequences, the trajectory of non-moving molecules was verified to confirm whether there was any drift in the image sequences. If the image sequences showed any drift, they were not used for analysis.

High-speed Atomic force microscopy (HS-AFM)

HS-AFM observations were carried out using the system described previously[31], except for the preparation of stage. The mica surface on the stage was freshly cleaved and coated with 2 μL of fluoro surf FS-1010S135-0.5 (Fluoro Technology) to make the surface hydrophobic and to have high affinity to the crystalline chitin. Then 10 μL of crystalline chitin suspension was dropped onto the surface before incubating at room temperature (~25 °C) for 10 min and covered with a moisture cap. The surface was rinsed twice with 80 μL of 50 mM sodium phosphate (pH 6.0). Immobilized crystalline chitins were initially observed without the *Sm*ChiA in 78 μL of 50 mM sodium phosphate (pH 6.0). After that, 2 μL of chitinase was added to obtain an enzyme at a final concentration of 2 μM. The solution was then mixed gently, and the images were recorded at 5 fps.

Home-built software based on Igor Pro (WaveMetrics) was used for the visualization and analysis of the HS-AFM images. I analyzed moving molecules that showed movements for 3 or more frames. A linear tracking function was used to track the moving molecules. First, the region of interest was selected manually at the first and last frame of each individual moving

molecule. The center of the region of interest was calculated using the software to obtain the position at each frame of tracking molecules. The translational velocity (k_{tr}) of the moving molecules was calculated using the following equation,

$$k_{\mathrm{tr}} = \frac{\sqrt{\Delta \mathrm{x}^2(\mathrm{nm}^2) + \Delta \mathrm{y}^2(\mathrm{nm}^2)}}{\text{moving time (s)}}$$

where Δx and Δy denote the difference between the start and the end positions of a moving molecule in the x and y direction, respectively. The distributions of k_{tr} were fitted with the Gaussian function. The processive catalysis rate constant (k_{pc}) was calculated by dividing k_{tr} by the step size of *Sm*ChiA (1.04 nm, the length of chitobiose). The distribution of the run length was fitted with the single-exponential decay function. The processivity was estimated from the obtained run length constant on the assumption that the *Sm*ChiA step size was 1.04 nm. The distribution of the moving time was fitted with the single-exponential decay function, and the inverse of the obtained moving time constant was used as the productive dissociation rate constant (k_{off}^{P}).

Structure and sequence alignment by bioinformatics

The sequence of *Sm*ChiA and *Sm*ChiA-like proteins from the different organisms were obtained using the Protein BLAST tool in the NCBI database (http://blast.ncbi.nlm.nih.gov). After the download of sequences, the signal sequences were removed according to the prediction of SignalP 5.0 (http://www.cbs. dtu.dk/services/SignalP)[57], with the appropriate organism group for prediction. The sequences for which SignalP could not predict the signal sequence were excluded from the alignment. The amino acid sequences of 258 chitinases were aligned and visualized using Clustal Omega (Clustalω : http://www.ebi. ac.uk/Tools/msa/clustalo)[58] and WebLogo (http://weblogo. threeplusone.com)[59], respectively.

The structure of SmChiA (PDB entry 1CTN) was superimposed with *Of*Chi-h (PDB entry 5GQB) and *Vh*ChiA (PDB entry 3B8S) using the alignment function of PyMOL.

3. Results and Discussion

*Sm*ChiA F232W/F396W mutant showed higher k_{cat} than WT

The previous study by Liu *et al*.[55] compared the hydrolytic activity of *Of*Chi-h, *Sm*ChiAWT, and *Sm*ChiA F232W/F396W. They found that the *Sm*ChiA F232W/F396W mutant showed higher hydrolytic activities against several insoluble chitin substrates than *Sm*ChiA WT; however, these results were obtained at only one substrate concentration[55]. In our previous study[54], we used a range of crystalline chitin concentrations (0–2 mg/mL) to estimate the k_{cat} and K_m values of *Sm*ChiA WT. In the present study, to confirm the high catalytic activity of the F232W/F396W mutant and estimate k_{cat} and K_m, I measured the hydrolytic activity of *Sm*ChiA WT and F232W/F396W at various crystalline chitin concentrations (0–6 mg/mL) using a liquid-handling robot, developed in our previous report[60]. The measurement was performed in two independent experiments carried out in triplicate. It is worth noting that contrary to the previous study[54], in the present study, His_6 tags were removed from the C terminus of the constructs during purification. This was done as positive charges of His_6 may change the binding/dissociation dynamics of *Sm*ChiA against the crystalline chitin immobilized on the surface of a negatively charged glass surface. Furthermore, fluorescently labeled enzymes (Cy3-D415C WT and F232W/F396W) were used for all biochemical measurements as these enzymes were also used for the single-molecule imaging analysis described later. Note that in our previous study[54], I confirmed that there is no significant difference between hydrolytic activities of Cy3-labeled and unlabeled enzymes.

As a result, F232W/F396W was found to show higher hydrolytic activity than WT in all of the crystalline chitin concentrations tested (Figure 7A). At a high crystalline chitin concentration (defined as more than 1 mg/mL), the hydrolytic activities of WT and F232W/F396W tended to show a degree of inhibition and were not appropriate within the

Michaelis–Menten equation. Thus, I used the hydrolytic activity at a low chitin concentration range (0–1 mg/mL) to ensure fit within the Michaelis– Menten equation (Figure 7B). The turnover number (k_{cat}) and Michaelis constant (K_m) for WT and F232W/F396W on crystalline chitin were subsequently estimated to be 3.1 ± 0.21 and 3.9 ± 0.21 s^{-1} and 0.32 ± 0.045 and 0.19 ± 0.030 mg/mL, respectively (Table 1). Furthermore, the values of k_{cat}/K_m for WT and F232W/F396W were 10 and 21 $mLmg^{-1}s^{-1}$, respectively. This result suggests a 2 times larger rate constant of productive binding for F232W/F396W than that for WT.

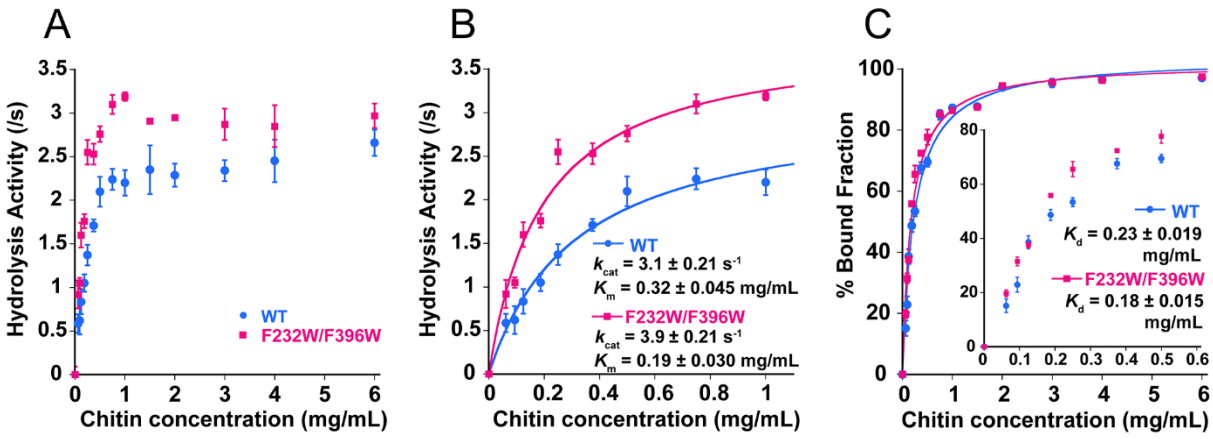

Figure 7. Biochemical analysis of *Sm*ChiA WT and F232W/F396W mutant. A, hydrolytic activity of *Sm*ChiA WT (blue) and F232W/F396W (pink) at various concentrations of crystalline chitin (0–6 mg/mL). B, same as A at a low concentration range (0 –1 mg/mL). The data points were fitted with the Michaelis–Menten equation to estimate k_{cat} and K_m of WT and F232W/F396W. The hydrolytic activity was measured in 50 mM sodium phosphate (pH 6.0) at 25 °C. C, the bound fraction of WT and F232W/F396W at various concentrations of crystalline chitin (0–6 mg/mL). Inset, the low chitin concentration range (<0.6 mg/mL). The amount of free enzymes was used to calculate the bound fraction percentage. The distribution was fitted with the Langmuir equation to estimate the dissociation constant (K_d). Error bars, S.D. of the sextupled (A and B) or triplicate (C) measurements.

In addition, I performed a biochemical binding assay to compare the ratio of bound fractions between WT and F232W/ F396W at various crystalline chitin concentrations. The free enzymes in the solution were used to calculate the percentage of the bound fraction. The plot was fitted using Langmuir's equation to estimate the dissociation constant (K_d) (Figure

7C). At a crystalline chitin concentration below 0.6 mg/mL, the binding affinity of F232W/F396W was found to be slightly higher than that of the WT (Figure 7C, inset). At a concentration of 2 mg/mL crystalline chitin, almost all of the enzymes of both the WT and F232W/F396W were found to be bound to the crystalline chitin surface (over 90%). The values of K_d for WT and F232W/ F396W were 0.23 ± 0.019 and 0.18 ± 0.015 mg/mL, respectively (Table 1). These results indicate that the binding affinity increased slightly as a result of the mutation of two phenylalanine residues into tryptophan residues.

Table 1. Summary of kinetic parameters determined by biochemical analysis.

Kinetic parameters	k_{cat} [1] s^{-1}	K_m [1] mg/mL	k_{cat}/K_m $mL mg^{-1}s^{-1}$	K_d [2] mg/mL
WT	3.1 ± 0.21	0.32 ± 0.045	10	0.23 ± 0.019
F232W/ F396W	3.9 ± 0.21	0.19 ± 0.030	21	0.18 ± 0.015

[1] k_{cat} and K_m were estimated from the biochemical activity measurement at a low chitin concentration range (0-1 mg/mL) with the fitting by the Michaelis-Menten equation.
[2] K_d was estimated from the bound fraction analysis with the fitting by Langmuir's equation.

Biochemical analysis confirmed that the F232W/F396W mutant of *Sm*ChiA has a higher hydrolytic activity than the WT, as shown previously[55] (Figure 7). I found that F232W/ F396W showed higher hydrolytic activity than WT at all chitin concentrations ranging from 0.063 to 6 mg/mL. Hydrolytic activities were slightly inhibited for both WT and F232W/ F396W at chitin concentrations higher than 1 mg/mL and could not be fitted using the Michaelis–Menten equation (Figure 7A). This inhibition can be either the product or substrate inhibition, and additional experiments are required to understand the mechanism.

At low chitin concentration range (0–1 mg/mL), the Michaelis–Menten equation could be applied to obtain an estimate of the k_{cat} and K_m (Figure 7B). The k_{cat} value for F232W/ F396W (3.9 s^{-1}) was higher than that for WT (3.1 s^{-1}) (Table 1). The K_m value for F232W/F396W (0.19 mg/mL) was lower than for WT (0.32 mg/mL), indicating that the affinity of the productive binding to the crystalline chitin of this mutant was higher than that of the WT. Actually, the F232W/F396W slightly increased the binding affinity to crystalline chitin, including productive and nonproductive bindings, as demonstrated by the results of biochemical bound fraction analysis, especially at low chitin concentrations (Figure 7C). The K_d values for WT and F232W/F396W were consistent with the K_m values (Table 1). Because Phe was mutated to Trp at two positions, the surface area that engages the CH-π interactions and the electronegativity of the π-system can be increased[61].

No significant differences in binding and dissociation rate constants and productive binding ratio for WT and F232W/F396W

To further clarify the mechanism responsible for the higher hydrolytic activity in the F232W/F396W mutant compared with the WT, I first performed single-molecule fluorescence imaging according to the methods described in our previous study[54]. Note that in the single-molecule fluorescence imaging and HS-AFM observation, it is difficult to define the chitin concentrations because the chitin microfibrils are attached on the glass or mica surface. Both the k_{on} and k_{off} of the WT and F232W/F396W were found to be similar (Figure 8). The distributions of k_{on} were fitted using the double Gaussian function (Figure 8, top). The values of the peak positions for the WT were $8.2 \pm 0.30 \times 10^8$ and $1.4 \pm 0.43 \times 10^9$ $M^{-1}\mu m^{-1}s^{-1}$, whereas those of the F232W/F396W were $9.1 \pm 0.43 \times 10^8$ and $1.8 \pm 0.29 \times 10^9$ $M^{-1}\mu m^{-1}s^{-1}$, respectively. The multiple peaks of k_{on} were related to the bundles of chitin microfibrils, wherein the first

peak was represented by k_{on} for a single crystalline chitin microfibril, as explained in our previous study[54]. Essentially, no significant differences in overall k_{on} between WT and F232W/F396W were obtained (Table 2).

The distribution of k_{off} was fitted using a double-exponential decay function (Figure 8, bottom). The slow and fast dissociations were associated with the bindings of the *Sm*ChiA to the hydrophobic and hydrophilic surfaces of crystalline chitin, respectively[54]. The ratios of the slow and fast dissociations were calculated from the area under the fitting curves. The slow dissociation rate constants for WT and F232W/F396W were 0.089 ± 0.15 s^{-1} (14%) and 0.058 ± 0.12 s^{-1} (15%), respectively. The fast dissociation rate constants for WT and F232W/ F396W were 1.4 ± 0.089 s^{-1} (86%) and 1.2 ± 0.058 s^{-1} (85%), respectively. Subsequently, the average value of k_{off} was calculated from the summation of the k_{off} and the ratio of the slow dissociation fraction and that of the fast dissociation fraction. As a result, the average values of k_{off} for WT and F232W/F396W were 1.2 and 0.99 s^{-1}, respectively (Table 2). As described below, I used these values of k_{off} as those of k_{off} for nonproductive binding (k_{off}^{NP}).

Next, I measured the productive binding ratio. Productive binding only occurs when *Sm*ChiA binds to the reducing end of the chitin chain on the hydrophobic surface of crystalline chitin. Therefore, the productive binding ratio of *Sm*ChiA is low, as was determined by single-molecule imaging analysis in our previous study[54]. In the present study, the productive binding ratio was determined from the ratio of the number of moving molecules (n^{P}) and nonmoving molecules (n^{NP}) after the binding to the chitin surface. For measurement, I further improved the localization precision of single-molecule fluorescence imaging to identify the slowly moving molecules more precisely (4.3 and 3.8 nm in the x and y direction at 3 frames per second (fps), with a laser at 1 μW/m^2 power). The productive binding ratios for WT and F232W/F396W were 0.074 ± 0.0041 and 0.076 ± 0.0089, respectively, and approximately the

same (Table 2).

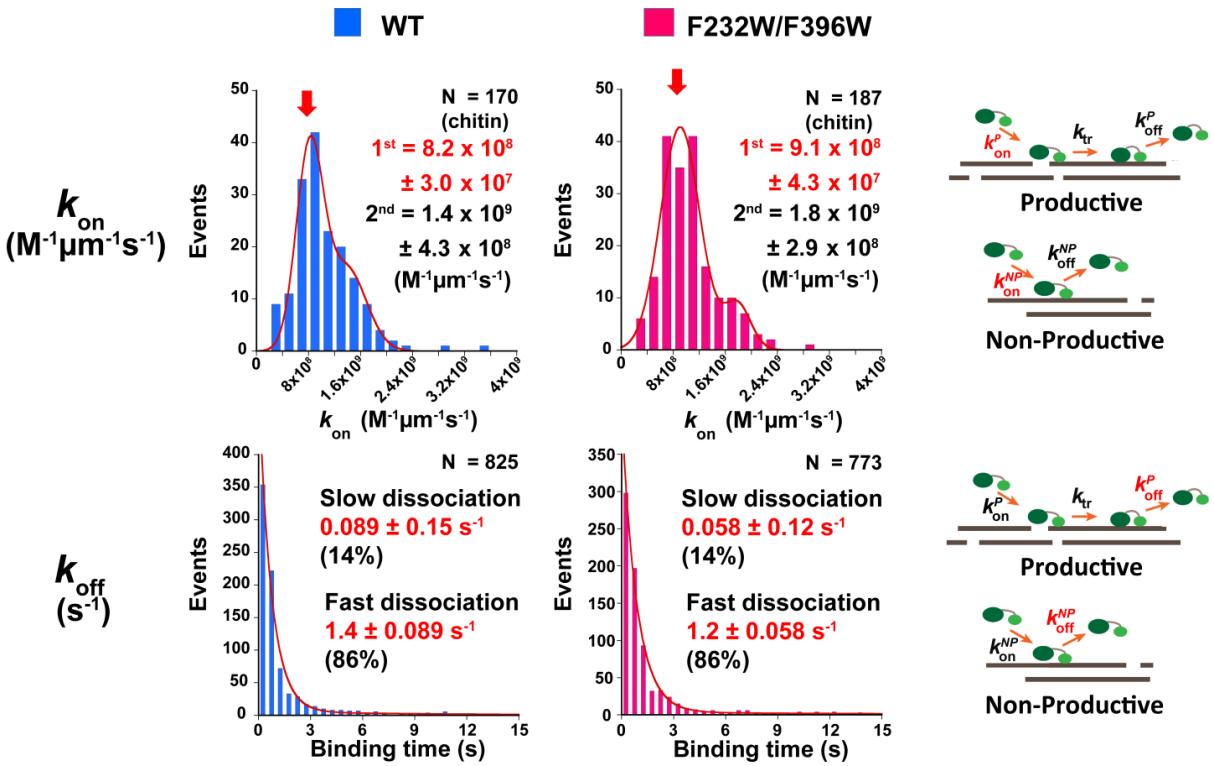

Figure 8. Comparison of the distribution of k_{on} and k_{off} of *Sm*ChiA WT (blue) and F232W/F396W (pink) obtained by single-molecule fluorescence imaging analysis. (Top) The distributions of k_{on} were fitted with the double Gaussian function. The first peak corresponds to the k_{on} against the single crystalline chitin microfibril. The sample number (N) in the distribution of k_{on} represents the number of crystalline chitins observed. (Bottom) The distributions of k_{off} were fitted with the double exponential decay function. A slow dissociation is associated to the binding of the enzyme to the hydrophobic crystalline chitin surfaces, while the fast dissociation is associated to the binding of the enzyme to the hydrophilic crystalline chitin surfaces. The sample number (N) in the distribution of k_{off} represents the number of *Sm*ChiA molecules observed.

F232W/F396W showed high processivity and low dissociation rate after productive binding

As no significant difference was found between the WT and F232W/F396W using single-molecule fluorescence imaging analysis, I then applied single-molecule imaging with HSAFM to improve the localization precision. Several chitin microfibrils were observed to avoid heterogeneity on the crystalline chitin surface. At least 10 molecules per chitin were observed

in order to estimate the translational velocity (k_{tr}), run length, and moving time (Figure 9). The distributions of k_{tr} were fitted with the single Gaussian function (Figure 9, left). As a result, the WT and F232W/F396W were found to have a similar k_{tr}, 52 ± 0.53 and 51 ± 0.72 nm/s, respectively. Then the processive catalysis rate constant (k_{pc}) was calculated from the k_{tr} divided by the step size 1.04 nm, which is same as the size of the reaction product, chitobiose[17]. The values of k_{pc} for WT and F232W/ F396W were 50 and 49, respectively. The distributions of run length (Figure 9, center) and moving time (Figure 9, right) were fitted with the single-exponential decay function. Note that the first bins (gray bars) of the run length were not included for fitting, because precise measurement of short run length was difficult. The values of run length for WT and F232W/F396W were 31 ± 2.6 and 54 ± 4.1 nm, respectively, and F232W/F396W showed a longer run length. Then the values of processivity (*P*, run length divided by step size) were calculated as 30 and 52 for WT and F232W/F396W, respectively. Because F232W/F396W showed longer run length than WT, its moving time was also longer. The values of moving time for WT and F232W/F396W were 0.69 ± 0.12 and 1.2 ± 0.13 s, respectively. Because I only analyzed moving molecules in the HS-AFM observation, the inverse of the moving time corresponds to the productive dissociation rate constant, k_{off}^{P}. The values of k_{off}^{P} for WT and F232W/F396W were 1.4 ± 0.26 and 0.82 ± 0.089 s^{-1}, respectively (Table 2).

Among the various kinetic parameters analyzed, processivity was the only one parameter for which F232W/F396W showed a higher value than the WT. The processivity of WT obtained by HS-AFM using β-chitin as a substrate was almost identical with that estimated in a previous report using HS-AFM[31] (values of 30 and 29 for the present and previous studies, respectively) (Figure 9). Moreover, the processivity of WT was also similar to the apparent processivity (36 ± 5) estimated by biochemical analysis using α-chitin[51].

For Phe-232 and Phe-396 of *Sm*ChiA, single point mutations have been reported previously. The mutation of Phe-232 to Ala dramatically decreased the hydrolytic activity. However, the binding affinity of F232A and WT against crystalline chitin were similar[21]. In addition, the Trp-231 of *Vibrio harveyi* chitinase A (*Vh*ChiA) corresponding to the Phe-232 in *Sm*ChiA (Figure 11), was mutated to Phe (W231F), which resulted in nondetectable levels of activity against the crystalline chitin substrate[62]. Phe-232 may be important in guiding the chitin chain into the substrate binding cleft not only in *Sm*ChiA but also in chitinase A in other organisms. Moreover, the mutation of F396A decreased the hydrolytic activity against the crystalline chitin. This F396A mutation increased the K_d value 2-fold and slightly reduced the processivity compared with WT[22, 63]. The slightly decreased K_m was also observed when Phe-396 was mutated to Trp with D313N[64-65]. Taken together, F232W/F396W mutation in *Sm*ChiA would be better in guiding the chitin chain, whereby the binding affinity was increased and the degree of processivity was improved as a result of the larger aromatic surface area of Trp compared with Phe. In previous studies, the hydrolytic activity of *Sm*ChiA against crystalline chitin was found to decrease after the introduction of an alanine mutation into the aromatic residues inside the substrate binding cleft (W167A, W275A, or F396A). These mutants showed reduced levels of processivity on the crystalline chitin[21, 51]. On the other hand, interestingly, these mutants were found to outperform *Sm*ChiA WT in the hydrolysis of soluble chitin and soluble chitosan[21-22]. Furthermore, recently, the F232W/F396W *Sm*ChiA mutant was found to increase hydrolytic activity for insoluble chitin (insect cuticle, α-chitin, and chitin nanowhisker), but a decreased activity in ethylene glycol chitin, which is a water-soluble chitin substrate[55]. In the present study, I found that high hydrolytic activity of the F232W/F396W against crystalline chitin resulted from high processivity. My results indicate that processivity is an important factor for the hydrolysis of crystalline substrates. On the other hand, it remains

elusive why the *Sm*ChiA alanine mutants (W167A, W275A, or F396A) and F232W/F396W, respectively, showed higher and lower hydrolytic activities than the *Sm*ChiA WT against the soluble substrates. To understand the mechanism and correlation with the processivity, measurements of the processivity of *Sm*ChiA WT and these mutants against the soluble substrates will be required.

The processivity (*P*) of *Sm*ChiA is related to k_{off}^{P} (Figure 9). If the value of *P* is high, that of k_{off}^{P} is low (Table 2). Several studies have reported largely different values of the dissociation rate [49-52]. The k_{off} from the chitin nanowhiskers was 0.012 ± 0.002 s^{-1}, whereas the k_{off} from the α-chitin after 10 min and 2 hour of incubation was 0.0028 ± 0.0003 and 0.0015 ± 0.0005 s^{-1}, respectively[51]. These values were much lower than those found in the present study and our previous study[54]. Because the previous studies of processive cellulases reported different k_{off} values measured with different methods[49, 52, 66-71], this difference could also occur in the case of processive chitinase. For chitinase, biochemical analysis revealed that the k_{off} value is also dependent on the type of substrate and the reaction time[51]. It is worth noting that in biochemical analysis, it is very difficult to distinguish productive and nonproductive bindings. On the other hand, in my single-molecule analysis, I have analyzed only productively bound *Sm*ChiA molecules moving on the surface of crystalline chitin.

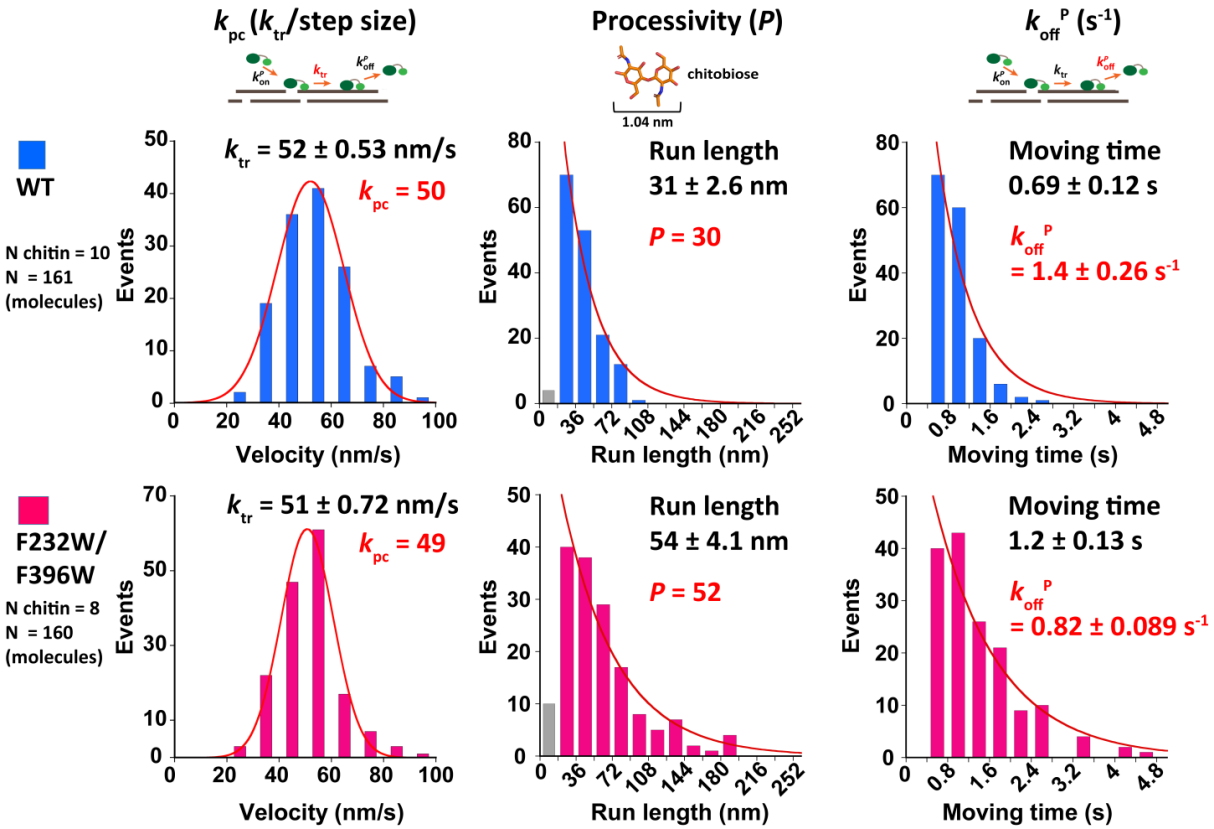

Figure 9. Comparison of the distribution of translational velocity (k_{tr}), run length, and moving time of WT (blue) and F232W/F396W (pink) obtained by HS-AFM. (Left) The distributions of k_{tr} were fitted with the single Gaussian function. The processive catalysis rate constant (k_{pc}) was calculated by dividing k_{tr} with the step size (product size: 1.04 nm). (Center and Right) The distributions of run length and moving time were fitted with the single exponential decay function. The processivity (P) was estimated by dividing the run length with the step size. The inverse of the moving time was determined as the productive dissociation rate constant (k_{off}^{P}), because all of the molecules analyzed by HS-AFM were moving molecules. The N and N chitin represent the number of *Sm*ChiA molecules and chitin microfibrils, respectively. The first bins (gray bars) of the run length were not included for fitting, because precise measurement of short run length was difficult.

Table 2. Summary of kinetic parameters determined by single-molecule analysis and reaction scheme.

Kinetic parameters	k_{on} [1] $M^{-1}\mu m^{-1} s^{-1}$	k_{off}^{NP} [1,2] s^{-1}	k_{on}^{P}/k_{on}^{NP} [1,3] (n^P/n^{NP})	k_{tr} [4,5] nm/s	k_{pc} [5] s^{-1}	P [4,6]	k_{off}^{P} [4] s^{-1}	k_{cat} [7] s^{-1}
WT	8.2×10^8 $\pm 3.0 \times 10^7$	1.2	0.074 $\pm$ 0.0041	52 $\pm$ 0.53	50	30	1.4 $\pm$ 0.26	2.9
F232W/ F396W	9.1×10^8 $\pm 4.3 \times 10^7$	0.99	0.076 $\pm$ 0.0089	51 $\pm$ 0.72	49	52	0.82 $\pm$ 0.089	4.1

[1] k_{on}, k_{on}^{P}/k_{on}^{NP} and k_{off}^{NP} values were obtained from single-molecule fluorescence imaging analysis.
[2] k_{off}^{NP}, which was the average k_{off}, was assumed to only contain non-productive binding.
[3] k_{on}^{P}/k_{on}^{NP} or n^P/n^{NP} was denoted as the productive binding ratio, where n^P and n^{NP} represent the number of moving and non-moving molecules for a total of 40 s observation, respectively. For this analysis, we defined moving molecules as the molecules which showed movements larger than 20 nm for 3 or more frames.
[4] k_{tr}, processivity (P) and k_{off}^{P} were obtained by HS-AFM observation. The molecules which showed movements for 3 or more frames were analyzed.
[5] k_{tr} was used to denote the translational velocity. k_{pc} was calculated by dividing the k_{tr} value by the step size (a product size, 1.04 nm).
[6] Processivity (P) was estimated from the run length divided by the step size (a product size, 1.04 nm).
[7] k_{cat} was calculated from the Equation 3.

Reaction scheme and calculation of k_{cat} from kinetic parameters obtained by single-molecule analysis

To calculate the k_{cat} from the kinetic parameters determined by single-molecule imaging analysis, a reaction scheme of *Sm*ChiA, including productive binding, nonproductive binding, and processive catalysis, is considered (Figure 10). As also described above, *Sm*ChiA has two binding modes: productive and nonproductive bindings. In the reaction scheme shown in Figure 10, these two modes are represented by four rate constants, the productive binding rate constant (k_{on}^{P}), the productive dissociation rate constant (k_{off}^{P}), the nonproductive binding rate constant (k_{on}^{NP}), and the nonproductive dissociation rate constant (k_{off}^{NP}). Furthermore, because *Sm*ChiA is a processive enzyme, another kinetic parameter is included, k_{pc}.

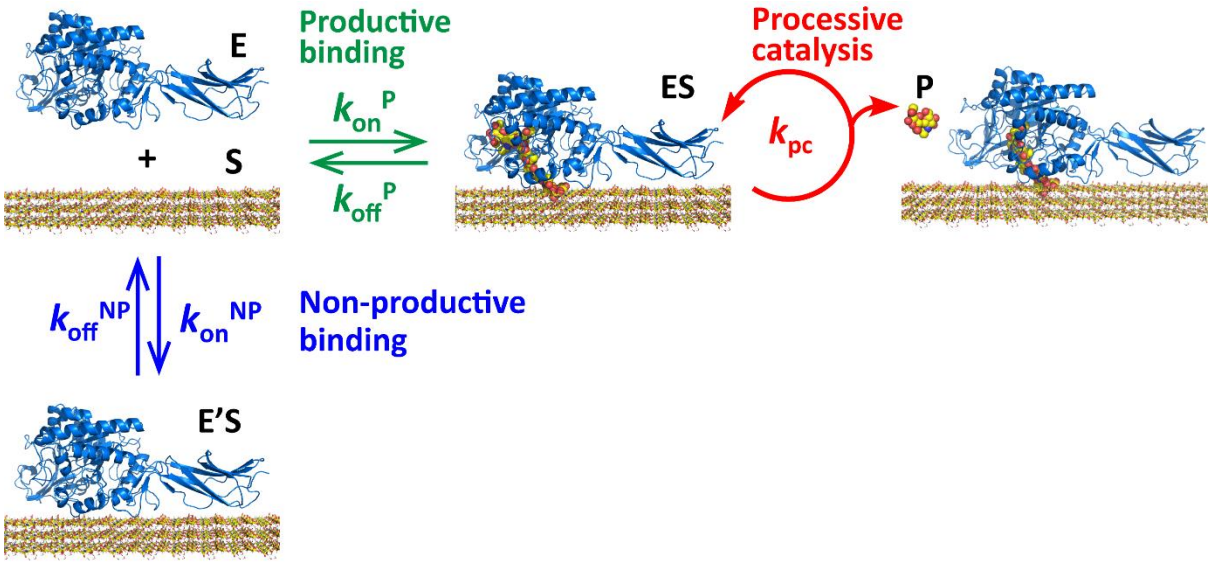

Figure 10. Reaction scheme of the processive catalysis of *Sm*ChiA described with the kinetic parameters obtained experimentally. The green, blue, and red arrows denote the productive binding/dissociation, nonproductive binding/dissociation, and processive catalysis (hydrolysis cycle), respectively. E, enzyme (*Sm*ChiA); S, substrate (crystalline chitin); ES, enzyme-substrate complex after productive binding; ES, enzyme-substrate complex after nonproductive binding; P, product (chitobiose).

From this reaction scheme, I can derive the equations to estimate k_{cat} and K_m as follow.

$$\text{rate} = \frac{\mathrm{dP}}{\mathrm{dt}} = k_{\mathrm{pc}} \cdot [\mathrm{ES}]$$

$$\mathrm{E0} = \mathrm{E} + \mathrm{ES} + \mathrm{E'S}$$

$$\frac{\mathrm{dE}}{\mathrm{dt}} = -(k_{\mathrm{on}}^{\mathrm{P}} + k_{\mathrm{on}}^{\mathrm{NP}}) \cdot [\mathrm{E}] \cdot [\mathrm{S}] + k_{\mathrm{off}}^{\mathrm{P}} \cdot [\mathrm{ES}] + k_{\mathrm{off}}^{\mathrm{NP}} \cdot [\mathrm{E'S}] = 0$$

$$\frac{\mathrm{dES}}{\mathrm{dt}} = k_{\mathrm{on}}^{\mathrm{P}} \cdot [\mathrm{E}] \cdot [\mathrm{S}] - k_{\mathrm{off}}^{\mathrm{P}} \cdot [\mathrm{ES}] = 0$$

$$[\mathrm{E}] = \frac{k_{\mathrm{off}}^{\mathrm{P}}}{k_{\mathrm{on}}^{\mathrm{P}}} \frac{[\mathrm{ES}]}{[\mathrm{S}]}$$

$$\frac{\mathrm{dE'S}}{\mathrm{dt}} = k_{\mathrm{on}}^{\mathrm{NP}} \cdot [\mathrm{E}] \cdot [\mathrm{S}] - k_{\mathrm{off}}^{\mathrm{NP}} \cdot [\mathrm{E'S}] = 0$$

$$[\mathrm{E}] = \frac{k_{\mathrm{off}}^{\mathrm{NP}}}{k_{\mathrm{on}}^{\mathrm{NP}}} \frac{[\mathrm{E'S}]}{[\mathrm{S}]}$$

$$[\mathrm{E'S}] = \frac{k_{\mathrm{off}}^{\mathrm{P}} \cdot k_{\mathrm{on}}^{\mathrm{NP}}}{k_{\mathrm{on}}^{\mathrm{P}} \cdot k_{\mathrm{off}}^{\mathrm{NP}}} [\mathrm{ES}]$$

$$\mathrm{E0} = \left(\frac{k_{\mathrm{off}}^{\mathrm{P}}}{k_{\mathrm{on}}^{\mathrm{P}}} \frac{1}{[\mathrm{S}]} + 1 + \frac{k_{\mathrm{off}}^{\mathrm{P}} \cdot k_{\mathrm{on}}^{\mathrm{NP}}}{k_{\mathrm{on}}^{\mathrm{P}} \cdot k_{\mathrm{off}}^{\mathrm{NP}}} \right) [\mathrm{ES}]$$

$$\mathrm{E0} = \left(\frac{k_{\mathrm{off}}^{\mathrm{P}} \cdot k_{\mathrm{off}}^{\mathrm{NP}} + (k_{\mathrm{on}}^{\mathrm{P}} \cdot k_{\mathrm{off}}^{\mathrm{NP}} + k_{\mathrm{off}}^{\mathrm{P}} \cdot k_{\mathrm{on}}^{\mathrm{NP}} \cdot [\mathrm{S}])}{k_{\mathrm{on}}^{\mathrm{P}} \cdot k_{\mathrm{off}}^{\mathrm{NP}} [\mathrm{S}]} \right) [\mathrm{ES}]$$

$$\mathrm{V} = \left(\frac{k_{\mathrm{on}}^{\mathrm{P}} \cdot k_{\mathrm{pc}} \cdot k_{\mathrm{off}}^{\mathrm{NP}} \, \mathrm{E0} \cdot [\mathrm{S}]}{k_{\mathrm{off}}^{\mathrm{P}} \cdot k_{\mathrm{off}}^{\mathrm{NP}} + (k_{\mathrm{on}}^{\mathrm{P}} \cdot k_{\mathrm{off}}^{\mathrm{NP}} + k_{\mathrm{off}}^{\mathrm{P}} \cdot k_{\mathrm{on}}^{\mathrm{NP}} \cdot [\mathrm{S}])} \right)$$

$$\mathrm{V} = \frac{\frac{k_{\mathrm{on}}^{\mathrm{P}} \cdot k_{\mathrm{pc}} \cdot k_{\mathrm{off}}^{\mathrm{NP}}}{k_{\mathrm{on}}^{\mathrm{P}} \cdot k_{\mathrm{off}}^{\mathrm{NP}} + k_{\mathrm{off}}^{\mathrm{P}} \cdot k_{\mathrm{on}}^{\mathrm{NP}}} \mathrm{E0} \cdot [\mathrm{S}]}{\frac{k_{\mathrm{off}}^{\mathrm{P}} \cdot k_{\mathrm{off}}^{\mathrm{NP}}}{k_{\mathrm{on}}^{\mathrm{P}} \cdot k_{\mathrm{off}}^{\mathrm{NP}} + k_{\mathrm{off}}^{\mathrm{P}} \cdot k_{\mathrm{on}}^{\mathrm{NP}}} + [\mathrm{S}]}$$

From Michaelis-Menten Equation;

$$\mathrm{V} = \frac{k_{\mathrm{cat}} \cdot [\mathrm{E}] \cdot [\mathrm{S}]}{K_{\mathrm{m}} + [\mathrm{S}]}$$

So;

$$k_{\mathrm{cat}} = \frac{k_{\mathrm{on}}^{\mathrm{P}} \cdot k_{\mathrm{pc}} \cdot k_{\mathrm{off}}^{\mathrm{NP}}}{k_{\mathrm{on}}^{\mathrm{P}} \cdot k_{\mathrm{off}}^{\mathrm{NP}} + k_{\mathrm{off}}^{\mathrm{P}} \cdot k_{\mathrm{on}}^{\mathrm{NP}}} \qquad \text{Equation 1}$$

And;

$$K_{\mathrm{m}} = \frac{k_{\mathrm{off}}^{\mathrm{P}} \cdot k_{\mathrm{off}}^{\mathrm{NP}}}{k_{\mathrm{on}}^{\mathrm{P}} \cdot k_{\mathrm{off}}^{\mathrm{NP}} + k_{\mathrm{off}}^{\mathrm{P}} \cdot k_{\mathrm{on}}^{\mathrm{NP}}} \qquad \text{Equation 2}$$

As described, the values of k_{off}^{P}, k_{off}^{NP}, and k_{pc} for WT and F232W/F396W in Equation 1 were already determined by the single-molecule imaging analysis. Because the ratio of productive binding was very low in the single-molecule fluorescence imaging, I approximated the values of k_{off}^{NP} with those of k_{off} (Figure 8 and Table 2). The values of k_{off}^{P} were obtained as the inverse of the moving time in the HS-AFM observation (Figure 9 and Table 2). The values of k_{pc} were also estimated from the k_{tr} divided by the step size (1.04 nm) in the HS-AFM observation (Figure 9 and Table 2). On the other hand, quantitative determinations of absolute values of k_{on}^{P} and k_{on}^{NP} were difficult even with single-molecule imaging analysis. The values of k_{on} that were obtained from the single-molecule fluorescence imaging included both productive and nonproductive bindings. I could not distinguish productive and nonproductive bindings because of low excitation laser power (0.14 μW/μm^2) and low localization precision (8.6 and 8.4 nm in x and y directions, respectively) under the experimental conditions used in the k_{on} and k_{off} measurements. Therefore, to calculate the values of k_{cat} from the kinetic parameters obtained, I modified Equation 1 and used the ratio of k_{on}^{P} and k_{on}^{NP} as follows.

$$k_{\mathrm{cat}} = \frac{\frac{k_{\mathrm{on}}^{\mathrm{P}}}{k_{\mathrm{on}}^{\mathrm{NP}}} \cdot k_{\mathrm{off}}^{\mathrm{NP}} \cdot k_{\mathrm{pc}}}{\frac{k_{\mathrm{on}}^{\mathrm{P}}}{k_{\mathrm{on}}^{\mathrm{NP}}} \cdot k_{\mathrm{off}}^{\mathrm{NP}} + k_{\mathrm{off}}^{\mathrm{P}}} \qquad \text{Equation 3}$$

The ratio of k_{on}^{P} and k_{on}^{NP} in Equation 3 corresponds to the productive binding ratio (n^{P}/n^{NP}) (Table 2), determined from the ratio of n^{P} and n^{NP} in the single-molecule fluorescence

imaging with high excitation laser power (1 μW/μm^2) and high localization precision (~4 nm for both x and y directions). The obtained values of k_{cat} for WT and F232W/F396W were 2.9 and 4.1 s^{-1}, respectively (Table 2). These values showed good agreement with those determined by the biochemical assay, which were 3.1 and 3.9 s^{-1} for WT and F232W/F396W, respectively (Table 1).

To gain further insight into the aromatic amino acid residues in the substrate-binding cleft, I then performed bioinformatics analysis. The amino acid sequence of *Sm*ChiA and those of 258 *Sm*ChiA-like proteins obtained by the BLAST analysis were aligned (Figure 11). As a result, I found that Phe-232 and Phe-396 of *Sm*ChiA were not conserved, and the Trp was predominant and higher than 80% at both positions. Interestingly, Hudson *et al.*[61] previously reported that, for most proteins that interact with carbohydrates, aromatic side chains are involved, and the most preferable amino acid residue is tryptophan. Furthermore, I also found that not only are the aromatic residues within the substrate binding cleft, but also many other amino acid residues in the substrate binding cleft are not conserved in *Sm*ChiA (Chapter 4, Figure18 and 20). My results strongly suggest that although *Sm*ChiA is the most studied processive chitinase, the amino acid sequence is not optimized for high hydrolytic activity. Bioinformatics analysis used in this study will be helpful to find the amino acid residues that are not conserved in *Sm*ChiA, and these amino acid residues can be targets of the mutation for further improvement of the crystalline chitin hydrolytic activity. Furthermore, my single-molecule imaging analysis and reaction scheme will make it possible to understand the mechanisms of the highly active mutants.

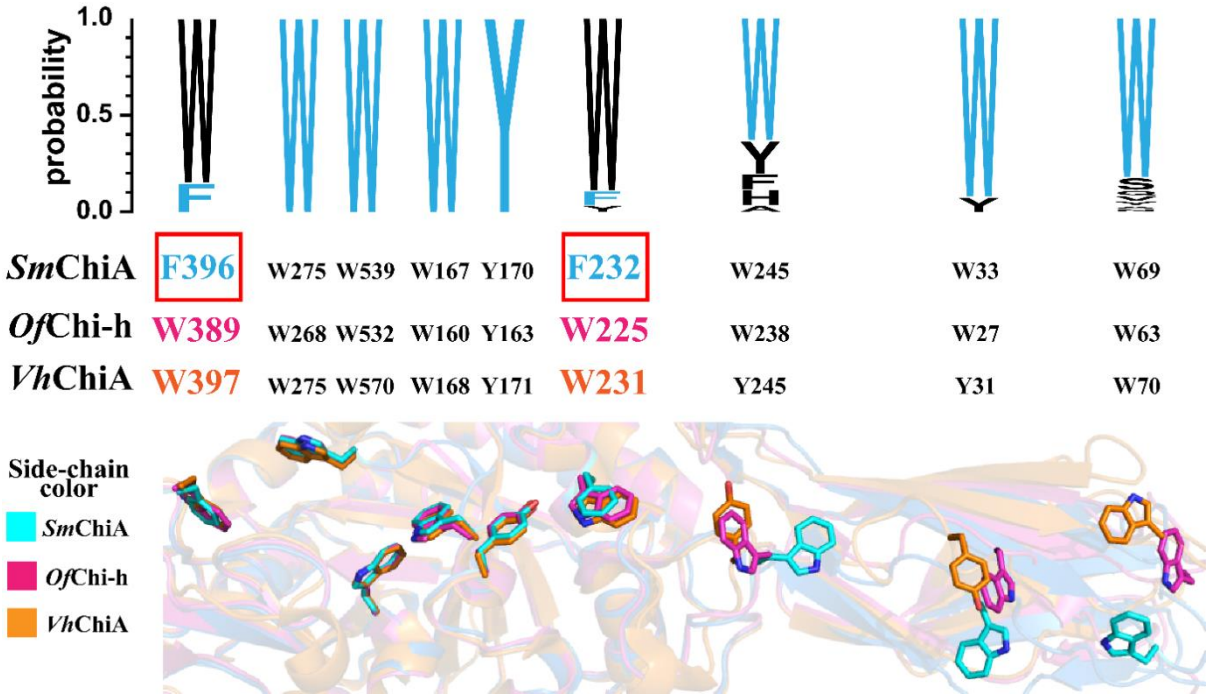

Figure 11. Comparison of the aromatic amino acid residues responsible for the binding to the crystalline chitin surface and chain sliding into the substrate binding cleft. The amino acid sequences of 258 *Sm*ChiA-like proteins were aligned and visualized by Clustal-Omega and WebLogo3. The aromatic amino acids of *Sm*ChiA are shown in cyan. The alignment shows the conservation of several aromatic amino acid residues involved in chitin binding. The structural alignment image was constructed by superimposing the crystal structure of *Sm*ChiA (PDB ID: 1CTN; blue; side chain highlighted with cyan), *Of*Chi-h (PDB ID: 5GQB; pink), and *Vh*ChiA (PDB ID: 3B8S; orange) using Pymol software. The side chains of aromatic amino acid residues are shown in stick models.

To conclude, the F232W/F396W mutant of *Sm*ChiA showed high processivity and low productive dissociation rate constant, which resulted in a k_{cat} value higher than that for WT. The values of k_{cat} for F232W/F396W and WT obtained by the biochemical analysis were well-reproduced by the kinetic parameters obtained by the single-molecule analysis, indicating the validity of the proposed reaction scheme. My results highlight the importance of the integration of biochemical analysis and single-molecule analysis to understand the mechanisms of *Sm*ChiA. To further clarify the mechanism in more detail, single-molecule analysis of the

*Sm*ChiA mutants with higher time resolution and higher localization precision probed with a gold nanoparticle will be very important[17].

Chapter 3

Optimization of primer design in site-saturation mutagenesis

1. Introduction

Site-saturation mutagenesis

A site-saturation mutagenesis is a powerful approach that allows for the generation of all possible mutations at the target site at once and widely used to improve enzyme thermostability, catalytic activity, and substrate specificity[72-78]. To increase the efficiency of randomization in saturation mutagenesis, primer design plays a critical role. Several methods such as 22c-trick[79], the Tang method[80], and the Max randomization[81] are developed nowadays to reduce the library size for the site-saturation mutagenesis. These methods are called as unbiased methods in which each amino acid is encoded by one codon (or two codons for valine and leucine in 22C-trick method). These methods can reduce the codon redundancy and bias, whereas various kinds of primers are required and can result in high cost as well as complications in primer design and PCR steps. In contrast, conventional degenerate oligonucleotides, such as NNN, NNB, and NNK/S, are more suitable for multisite saturation mutagenesis in terms of cost, simplicity of primer design, and reduced number of PCR primers.

In addition to the primer design methods, several molecular cloning techniques, such as QuickChange mutagenesis, In-Fusion[82], In vivo Assembly (IVA) cloning[83], Seamless Ligation Cloning Extract from *E.coli* (SLiCE)[84-85], and Gibson assembly[86-87], also have been developed to improve the mutagenesis procedure. These methods play an important role in simplifying and reducing the cloning processes.

In this Chapter, I evaluated a method of plasmid-based one-pot saturation mutagenesis employing the three techniques, namely conventional degenerate NNN or NNB codons for single-site saturation mutagenesis, IVA cloning for primer design, and SLiCE for ligating both ends of the fully amplified linear plasmid with homologous recombination in vitro. I optimized the design of degenerate oligonucleotides for saturation mutagenesis whether NNN or NNB

codon is better. In addition, since there are several suppliers that provide the degenerate codon generation, I also evaluate different primer set (NNN or NNB) from different three suppliers. In order to optimize the degenerate oligonucleotides for saturation mutagenesis, the loss-of-function mutant of green fluorescence protein, GFPMut3-Y66H[88], was used for introducing NNN or NNB codon. The colonies obtained from transformation step were analyzed with two different methods; colony counting and deep sequencing analysis. Colony counting is the easy, simple and low cost method that the ratio of gain-of-function mutant of GFP was immediately observed after getting colonies. On the other hand, deep sequencing method is the time consuming and high-cost method. However, the detailed information of nucleotide incorporated at the interested position can be obtained by this method.

2. Materials and Methods

All chemicals were purchased from Wako. The template plasmid pEDA5_GFPmut3_Y66H was a gift from Timothy Whitehead (Michigan State University, Addgene plasmid #80085). PrimeSTAR HS DNA polymerase was purchased from Takara. Plasmid extraction kit was purchased from NIPPON Genetics Co., Ltd. Wizard SV gel and PCR clean-up system was purchased from Promega. All primers (containing NNN or NNB, where B = T/G/C) were purchased from supplier 1 (Fasmac), supplier 2 (Eurofin), and supplier 3 (Integrated DNA Technologies).

Primer Design for Saturation Mutagenesis of Loss-of-Function GFP

All NNN degenerate codon primers contained all 64 codons, including three stop codons. The forward primer (5′-CACTTGTCACTACTTTCGGTNNNGGTGTTCAATGCTTTG CG-3′), containing one degenerate NNN motif, had a melting temperature (Tm) of 68 °C. The NNB primers included 48 codons, including one stop codon. The forward primer (5′-CACTTGTCACTACTTTCGGTNNBGGTGTTCAATGCTTTGCG-3′), containing one degenerate NNB motif, had a Tm of 68 °C. The concentration of all primers was adjusted to 10 pmol/μL for PCR. The following reverse primer was used for all saturation mutagenesis experiments: 5′-ACCGAAAGTAGTGACAAGTGTTGGCCATGGAACAGGTAG-3′.

PCR and DpnI Treatments

All three-step PCRs were carried out with PrimeSTAR HS polymerase. The PCR mixture was as follows: 10 μL of 5× PS buffer, 4 μL of 2.5 mM dNTP, 0.5 μL of PrimeSTAR HS DNA polymerase, 2 μL of 10 pmol/μL primer mix, and 1 ng of template plasmid, made up to a volume of 50 μL with sterilized water. The thermocycling protocol was as follows: 30 cycles

of 98 °C for 10 s, 55 °C for 5 s, and 72 °C for 4 min and 30 s. After amplification, all products were incubated with 1 μL of DpnI (NEB) for 15 min at 37 °C to digest the template plasmid in the reaction mixture. To increase the efficiency of SLiCE cloning, 1% agarose electrophoresis was performed, then each fragment was extracted, and purified by a gel clean-up system.

SLiCE Cloning and Transformation

SLiCE cloning uses homologous recombination to ligate DNA fragments from cellular extracts in vitro. SLiCE and 10× SLiCE reaction buffer (0.5 M Tris−HCl pH 7.5, 100 mM MgCl2, 10 mM ATP, and 10 mM DTT) were prepared as previously described.15 Briefly, the product (20 ng), 1 μL SLiCE, and 1 μL SLiCE reaction buffer were mixed in a reaction volume of 10 μL. The mixture was incubated at 37 °C for 30 min. After the SLiCE reaction, the samples were immediately used for transformation or stored at −30 °C. SLiCE reactant (5 μL) was added to 50 μL of Tuner (DE3) competent cells on ice and mixed moderately. Within 1 min, these mixtures were transferred to a cold cuvette, and transformation was carried out with a MicroPulser electroporator (Bio-Rad). Immediately after electroporation, 300 μL of iced super optimal broth with catabolite repression (SOC) was added. The transformed cells were incubated at 37 °C for 30 min. Finally, 150 μL of each transformant was spread on 15 cm LB-agar plates with 50 μg/mL ampicillin and incubated at 37 °C overnight.

Colony Counting

Colonies were counted under blue/ green LED (Handy Blue/Green LED). The recovery rate was represented as illuminated colonies normalized to all colonies from each primer set and supplier [(number of illuminated colonies/total number of colonies) × 100], respectively. For calculating the fraction of gain-of-function by deep sequencing, the number of TAT and

TAC codons was counted [(number of TAT and TAC/total number of counts) × 100]. For calculating the expected fraction of gain-of-function, the number of TAT and TAC codons were counted and divided by the number of codons in each primer set [(number of TAT and TAC/total number of codons) × 100].

Comparison of PCR Products with 64 Primers Encoding Different Codons

The pEDA5_GFPmut3_Y66H was amplified with 64 kinds of forward primers encoding different codons (5′-CACTTGTCACTACTTTCGGTXXXGGTGTTCAATGCTTTGCG-3′, where X is A, C, G, or T) and the same reverse primer as described above. Other conditions of PCR were the same as the saturation mutagenesis experiments. Products (2 μL) were electrophoresed in 1% agarose.

Deep Sequencing

All colonies on each plate were collected with 10 mL of LB medium and centrifuged at 4000g for 10 min. The number of transformants used for deep sequencing were supplier 1 (NNN: 1,453, NNB: 1,618), supplier 2 (NNN: 2,048, NNB: 1,573), and supplier 3 (NNN: 1,527, NNB: 2,128). Plasmid mixtures were extracted from each cell pellet by a plasmid extraction kit, diluted to 1 ng/μL, and amplified by PCR for deep sequencing. The forward primer was 5′-TCGTCGGCAGCGTCAGATGTGTATAAGAGACAG + ATATTCAGGGAGACCACAA CGGTTTC-3′, and the reverse primer was 5′-GTCTCGTGGGCTCGGAGATGTGTATA AGAGACAG + GTGTCTTGTAGTTCCCGTCATCTTTG-3′. Both primers had additional sequences (underlined) for deep sequencing. The PCR was performed in two steps, each with 30 cycles of 94 °C for 10 s and 68 °C for 4 min and 30 s, with PrimeSTAR HS DNA polymerase. All products were electrophoresed in 1% agarose and purified with a gel clean-up system. All

experiments described below were performed by Hokkaido System Science Co., Ltd. Additional adapter sequences were attached with KAPA HiFi DNA polymerase (HotStart Ready mix) by second index PCR (preincubation 95 °C for 3 min, 8 cycles of 95 °C for 10 s, 55 °C for 30 s, and 72 °C for 30 s, followed by 72 °C for 5 min). Nextera XT index primers N7xx and S5xx were used. All fragments were purified by AMPure XP beads (Beckman Coulter Genomics). Deep sequencing was performed with MiSeq system (Illumina) by Hokkaido System Science Co., Ltd. Processed codon counts data used for analysis were as follows: supplier 1 (NNN: 86,048, NNB: 82,657), supplier 2 (NNN: 83,927, NNB: 79,696), and supplier 3 (NNN: 80,325, NNB: 83,835). For calculation of the gain-of-function fraction from the results of deep sequencing, the numbers of TAT and TAC codons were counted and used [(number of TAT and TAC/total number of counts) × 100]. For calculation of the expected value of gain-of-function fraction, the number of TAT and TAC codons in each primer set were counted and divided by the total numbers of codons.

3. Results and Discussion

The fraction of Gain-of-Function GFP Mutants Analyzed by Colony Counting and Deep Sequencing

To assess one-pot saturation mutagenesis and to understand the efficiency of randomization, I applied the method to a non-fluorescent, loss-of-function green fluorescent protein (GFP) mutant, GFPmut3-Y66H[88], using NNN or NNB primers from three suppliers. First, I have designed a method to generate and screen a wide variety of mutant proteins. The bottleneck steps include the mutant construction and protein purification. To resolve these limiting steps, I combined one-pot saturation mutagenesis with robot-based small-scale purification of a large number of mutants. My experimental system is shown in Figure 12. To assess nucleotide and amino acid biases, one-pot saturation mutagenesis was performed with degenerate NNN and NNB codons from three different suppliers. The fractions of gain-of-function mutations of GFPmut3 were analyzed by colony counting and deep sequencing.

Prior to the comparison of NNN and NNB, I checked bias in DNA amplification efficiency of PCR depending on codons, using 64 primers encoding different codons (Figure 13). The amounts of PCR products (~4,500 bp) were basically similar among all codons except ATA, which did not show clear bands. This result indicates that the PCR step does not cause bias basically, at least when pEDA5-GFPmut3-Y66H is used as a template.

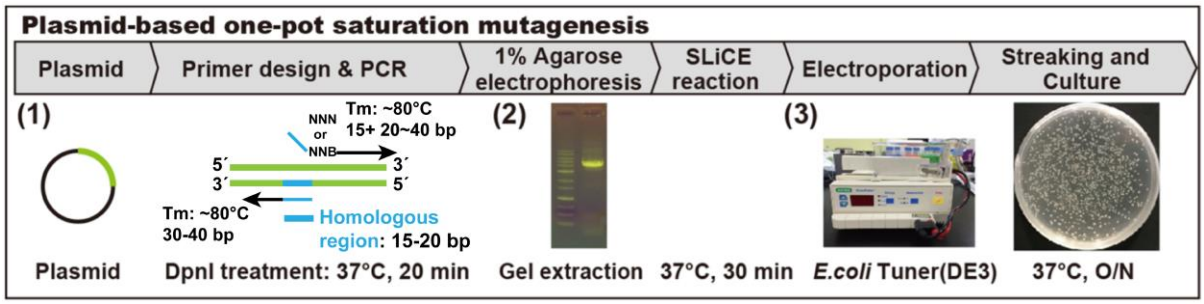

Figure 12. Overview of one-pot saturation mutagenesis used in this study. There were five steps from cloning to purification. (1) Single-site/multisite saturation mutagenesis. (2) Extraction/purification of fragments and SLiCE reaction (ligation). (3) Transformation into Tuner^{TM} (DE3) cells directly by electroporation for checking protein expression.

Then, to determine the recovery rate for each supplier's degenerate codons by colony counting, the pEDA5-GFPmut3- Y66H plasmid was amplified by PCR with primers containing either NNN or NNB codons. The linear products were ligated with SLiCE, transformed into *E. coli* cells, and cultured on agar plates at 37 °C overnight. Colonies were counted under visible light, and the number of fluorescent colonies (gain-of-function, H66Y mutants) was counted under a blue/green light-emitting diode (LED) light (Figure 14). The fractions of gain-of-function colonies are shown in Table 3. For both NNN and NNB primers, suppliers 1−3 showed gain-of-function fractions with values that were slightly lower or higher than expected. However, the differences were minor, ranging from −0.9 to 2.0% (Table 3). All experimental values were similar to expectation, showing no apparent biases.

To investigate the potential biases in more detail, all colonies were collected and plasmids were extracted and analyzed by deep sequencing. First, to estimate fractions of gain-of-function GFP mutants, tyrosine codons (TAT, TAC) were counted (Table 3). Again, for both NNN and NNB primers, suppliers 1−3 showed fractions of gain-of-function similar to the expected values, with differences ranging from −0.9 to 1.1% (Table 3). For each primer set and supplier, the value estimated by deep sequencing was similar to that from colony counting, indicating the validity of the deep sequencing (Table 3).

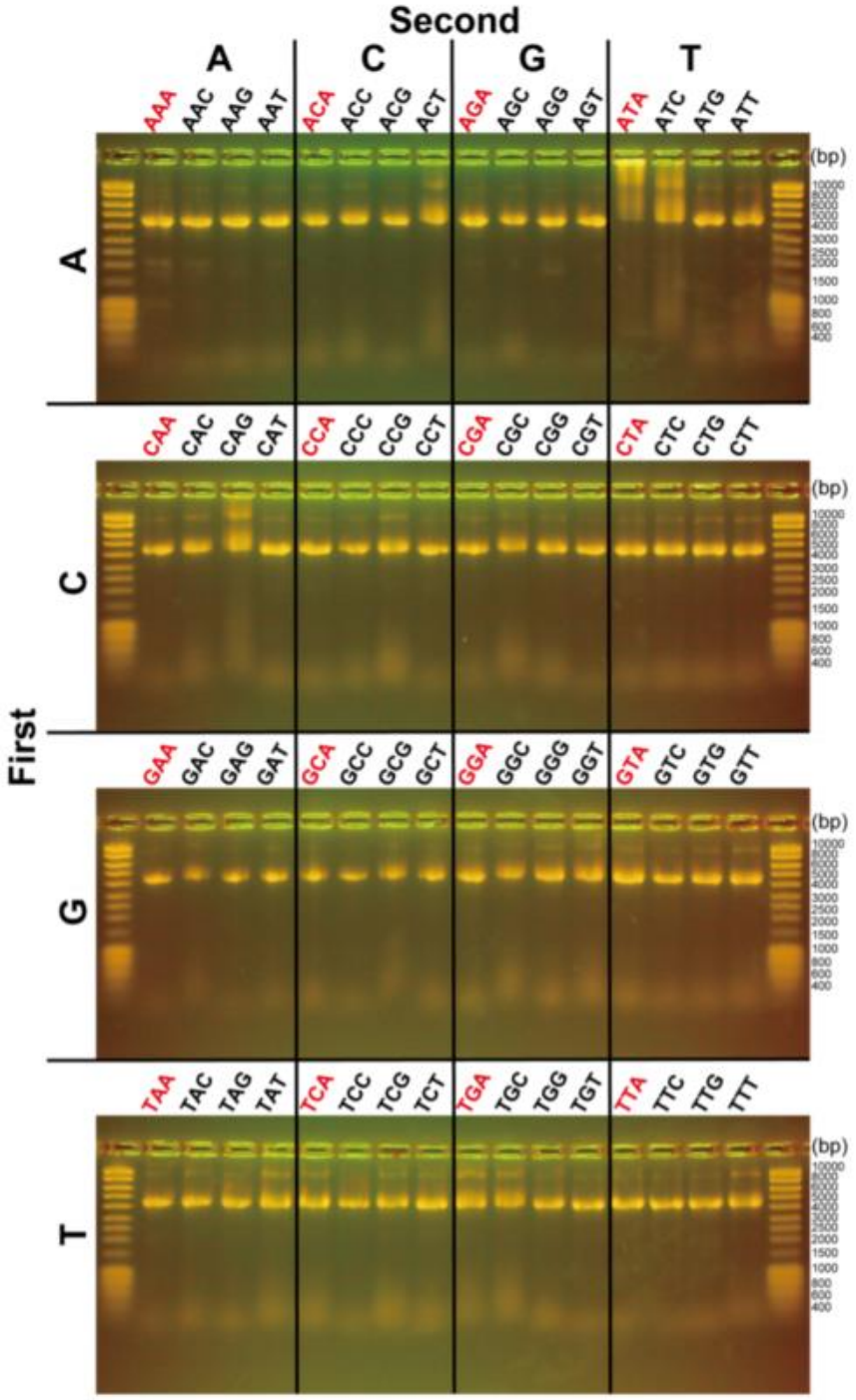

Figure 13. Comparison of PCR products of GFPmut3-Y66H mutant with 64 primers encoding different codons. The intensities of bands (~4,500 bp) of PCR products are basically similar in all codons except ATA, which did not show the clear band. The codons not included in NNB (A at third positions) are shown in red.

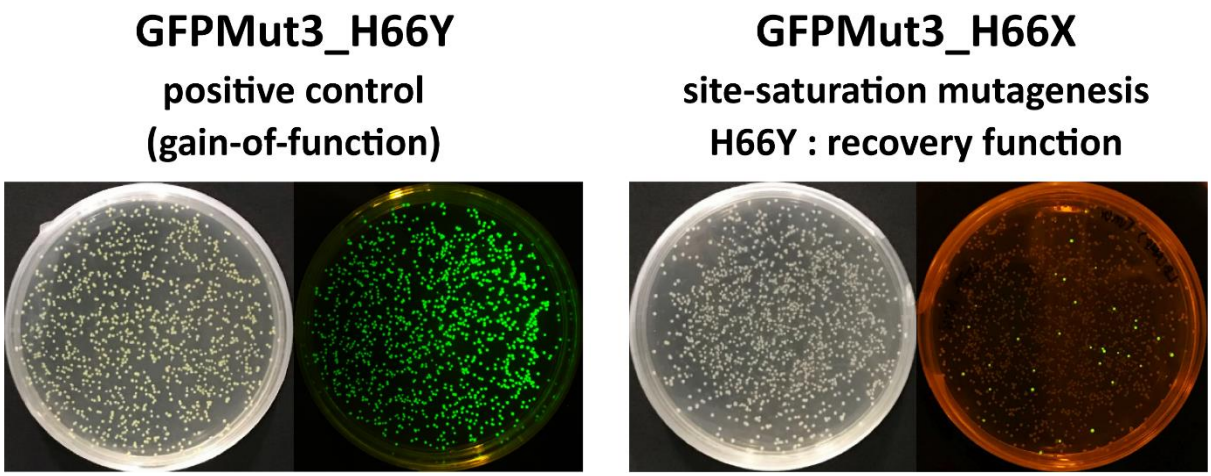

Figure 14. An example transformation plates of gain-of-function mutant of GFPMut3 for positive control (gain-of-function mutant, GFPMut3_H66Y) and the site-saturation mutagenesis experiments (GFPMut3H66X). The colonies obtained from site-saturation mutagenesis experiments were counted under visible light. The gain-of-function colonies (green colonies) were counted under the blue/green light-emitting diode (LED) light.

Table 3. Fractions of gain-of-function GFPMut3-H66Y mutants from each primer set and supplier determined by colony counting and deep sequencing.

primer set	supplier	colony counting	deep sequencing	expected value
NNN	1	2.2% (32/1,453)	2.2% (1,990/86,048)	3.1% (2/64)
	2	4.2% (86/2,048)	3.1% (2,571/83,927)	
	3	5.1% (78/1,527)	4.2% (3,364/80,325)	
NNB	1	4.5% (73/1,618)	4.2% (3,636/85,577)	4.2% (2/48)
	2	3.8% (60/1,573)	3.5% (3,078/88,751)	
	3	3.6% (77/2,128)	3.7% (3,201/86,419)	

Biases in Codons and Nucleotides Estimated by Deep Sequencing

Next, I determined the fraction of each codon from each primer set and supplier. Figure 15 shows the fraction of each codon, ordered from largest to smallest. Expected fractions of each codon from NNN and NNB are 1.6% (1/64) and 2.1% (1/48), respectively. However, NNN from suppliers 1 and 2 showed significantly larger fractions of the top 10 codons, whereas this bias was slightly less severe in NNB (Table 4).

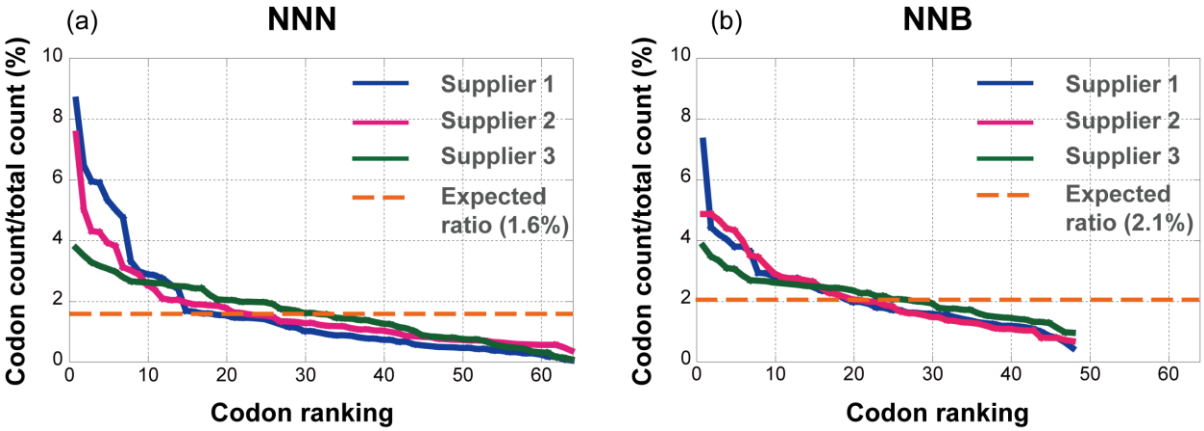

Figure 15. Ranking of codons in NNN and NNB from three suppliers, determined by deep sequencing. Fractions of each codon as determined by deep sequencing were estimated and ranked. (a) Degenerate NNN includes 64 codons. (b) NNB includes 48 codons. Results from suppliers 1, 2, and 3 are shown by blue, red, and green lines, respectively.

I then assessed the nucleotide bias more directly by estimating fractions of each nucleotide (Table 5). NNN primers from suppliers 1 and 2 had significantly higher fractions of T and G than those of A and C. Notably, NNN from supplier 1 showed an extremely low fraction of A. Proportions of A, T, G, and C in primers from supplier 3 were similar to the expected values (25%). In the case of NNB, the expected values were different because A was not present at the third position of NNB; therefore, the expected value of the fraction of A was 16% and those of T, G, and C were 28%. In primers from supplier 1, the value of the fraction of T was highest

and that of G was equal to the expected value. However, the value of the fraction of C was lower than expected. From supplier 2, the values of the fractions of T and G were higher than expected and that of C was lower than expected. In contrast, the fractions of A, T, G, and C were highly similar to expectations in both NNN and NNB primers from supplier 3. In the previous study, it has been reported that hand-mixed degenerate primers showed lower nucleotide bias than machine-mixed degenerate primers when used for PFunkel[89]. In my study, I have not used hand-mixed degenerate primers for both NNN and NNB codons from supplier 1 to 3. The biases observed in my study may be improved if hand-mixed degenerate primers are used.

Table 4. Top 10 rankings of the codons in NNN and NNB from three suppliers, determined by deep sequencing.

	Supplier 1 (codon, %)		Supplier 2 (codon, %)		Supplier 3 (codon, %)		expected (%)
NNN	TTT	8.6	TTT	7.5	GGG	3.7	1.6 (1/64)
	GTT	6.4	TGG	5.0	GGA	3.5	
	GGG	5.9	GTT	4.3	CAG	3.2	
	TGG	5.9	GGT	4.2	ACG	3.1	
	TTG	5.3	TGT	3.9	GGC	3.0	
	TGT	5.0	TTG	3.8	GCC	2.9	
	GTG	4.7	GGG	3.1	CTT	2.8	
	TTC	3.3	GTG	3.0	TAT	2.6	
	TCG	2.9	TTC	2.8	TCT	2.6	
	TCT	2.9	ATT	2.5	GTT	2.6	

Table 4-continued. Top 10 rankings of the codons in NNN and NNB from three suppliers, determined by deep sequencing.

	Supplier 1 (codon, %)		Supplier 2 (codon, %)		Supplier 3 (codon, %)		expected (%)
NNB	TTT	7.2	TTT	4.8	TTT	3.8	2.1 (1/48)
	GTT	4.4	TGG	4.8	GGG	3.4	
	TGG	4.2	TTG	4.6	TGG	3.3	
	TTC	4.0	GTT	4.4	GGC	3.1	
	GGT	3.8	TGT	4.3	CGG	3.0	
	ATT	3.8	GGG	3.9	GTT	2.8	
	TGT	3.6	ATT	3.5	GAG	2.6	
	GGG	2.9	GGT	3.4	GTG	2.6	
	TAT	2.9	GTG	3.1	CAG	2.6	
	TCT	2.8	GAG	2.9	ACG	2.6	

Table 5. Fractions of A, T, G, and C in each primer set, from each supplier, determined by deep sequencing.

primer	supplier	A	T	G	C
NNN[a]	1	**9%** (23,183/258,114)	**41%**(106,320/258,114)	**34%** (87,976/258,114)	**16%** (40,665/258,114)
	2	**16%** (40,428/251,781)	**38%** (95,853/251,781)	**31%** (76,807/251,781)	**15%** (38,691/251,781)
	3	**24%** (56,992/240,975)	**26%** (61,972/240,975)	**24%** (68,464/240,975)	**22%** (53,547/240,975)
NNB[b]	1	**13%** (33,350/256,731)	**39%** (98,622/256,731)	**28%** (72,912/256,731)	**20%** (51,847/256,731)
	2	**13%** (32,967/266,253)	**35%** (93,144/266,253)	**34%** (89,211/266,253)	**18%** (47,073/266,253)
	3	**15%** (39,392/259,257)	**29%** (74,528/259,257)	**31%** (81,671/259,257)	**25%** (63,666/259,257)

[a]In NNN, the expected fractions of A, T, G, and C were 25%.
[b]In NNB, the expected fractions were 16% A and 28% each of T, G, and C.

To examine the nucleotide bias in more detail, I analyzed the fractions of A, T, G, and C at each of the three positions of each codon (Table 6). NNN and NNB primers from suppliers 1 and 2 showed higher fractions of T and G than those of A and C at all three positions. In contrast, NNN from supplier 3 showed smaller biases than those from suppliers 1 and 2 at all

three positions. This was also the case for NNB primers from supplier 3. Overall, codon and nucleotide biases were lower in NNB than in NNN, although the effects of different template sequences and DNA polymerases were not evaluated in my study. To draw a general conclusion about the difference in the biases between NNN and NNB, further quantitative analysis of different target proteins will be required.

Table 6. Fractions of A, T, G, and C at the first, second, and third nucleotide positions of the codons in each primer set and supplier, determined by deep sequencing.

		first nucleotide (%) **(N)**				second nucleotide (%) **(N)**				third nucleotide (%) **(N or B)**			
primer set	supplier	**A**	**T**	**G**	**C**	**A**	**T**	**G**	**C**	**A**	**T**	**G**	**C**
expected ratio (NNN)		**25**	**25**	**25**	**25**	**25**	**25**	**25**	**25**	**25**	**25**	**25**	**25**
expected ratio (NNB)		**25**	**25**	**25**	**25**	**25**	**25**	**25**	**25**	**0**	**33.3**	**33.3**	**33.3**
NNN	1	**9**	**42**	**33**	**16**	**8**	**43**	**33**	**16**	**9**	**39**	**37**	**15**
	2	**16**	**38**	**30**	**16**	**17**	**38**	**30**	**15**	**16**	**39**	**31**	**14**
	3	**21**	**28**	**32**	**19**	**28**	**19**	**26**	**27**	**22**	**30**	**27**	**21**
NNB	1	**19**	**36**	**26**	**19**	**20**	**36**	**26**	**18**	**0**	**44**	**33**	**23**
	2	**18**	**34**	**30**	**17**	**19**	**33**	**31**	**17**	**0**	**39**	**41**	**20**
	3	**21**	**26**	**29**	**24**	**24**	**24**	**30**	**22**	**0**	**36**	**36**	**28**

Biases in Amino Acids

I also translated my deep sequencing results into amino acids (Figures 16 and 17). I found obvious biases in amino acids translated from NNN (Figure 16, top panels). Several amino acids with significantly higher and lower fractions than expected were observed for suppliers 1−3. Indeed, values more than twice as high from the expected values for valine, phenylalanine, and tryptophan were observed for both suppliers 1 and 2 (Figure 17, top panels). Furthermore,

the fractions of lysine, histidine, glutamic acid, threonine, asparagine, and glutamine were less than half of that expected from supplier 1, whereas no amino acids with significantly low fractions were observed with supplier 2. Codons from supplier 3 showed only one amino acid, glycine, with a ratio 2 times higher than expected, whereas three amino acids, lysine, arginine, and isoleucine, showed ratios significantly lower than expected. The amino acid analysis, therefore, revealed biases in NNN codons from all three suppliers (Table 7).

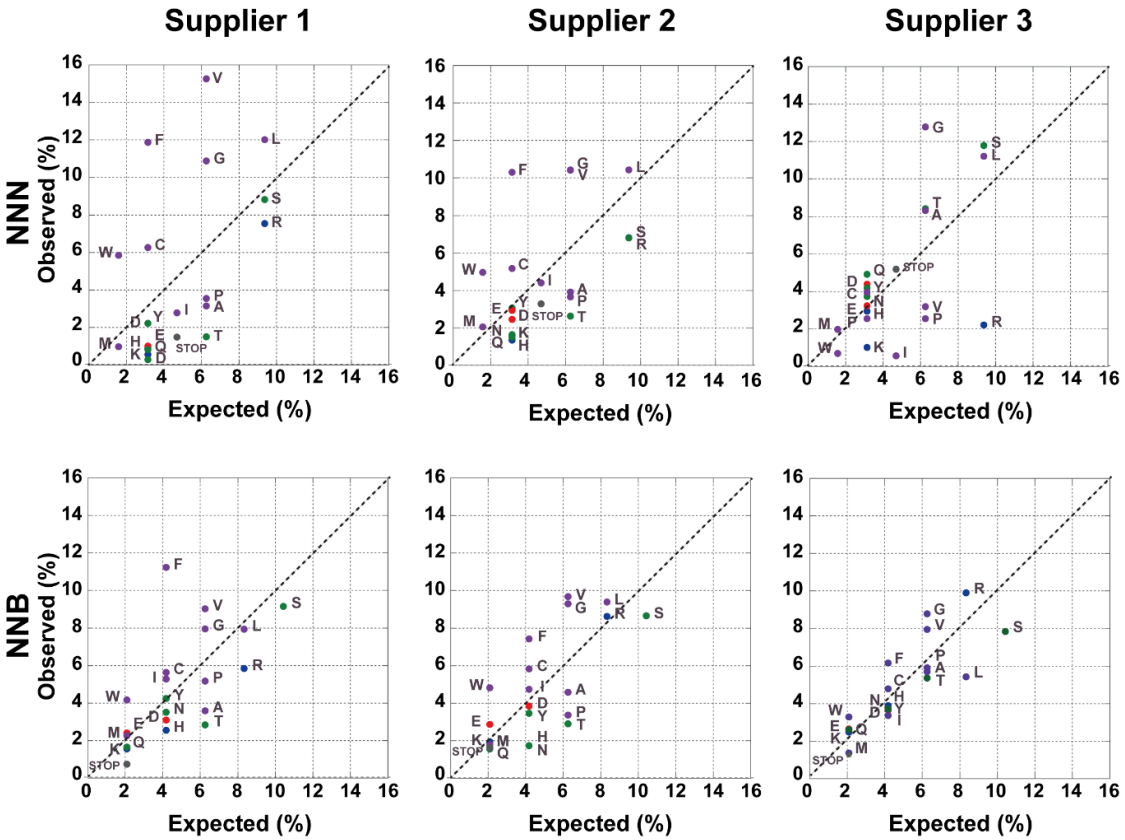

Figure 16. Observed vs expected fractions of 20 amino acids in primer sets from each supplier as determined by deep sequencing. The 20 amino acids were classified and colored on the basis of their properties. Basic amino acids lysine (K), arginine (R), and histidine (H) are colored blue. Acidic amino acids aspartic acid (D) and glutamic acid (E) are colored red. Uncharged polar amino acids serine (S), threonine (T), tyrosine (Y), asparagine (N), and glutamine (Q) are colored green. Nonpolar amino acids alanine (A), valine (V), leucine (L), isoleucine (I), proline (P), phenylalanine (F), methionine (M), tryptophan (W), glycine (G), and cysteine (C) are colored purple. Stop codons are colored gray.

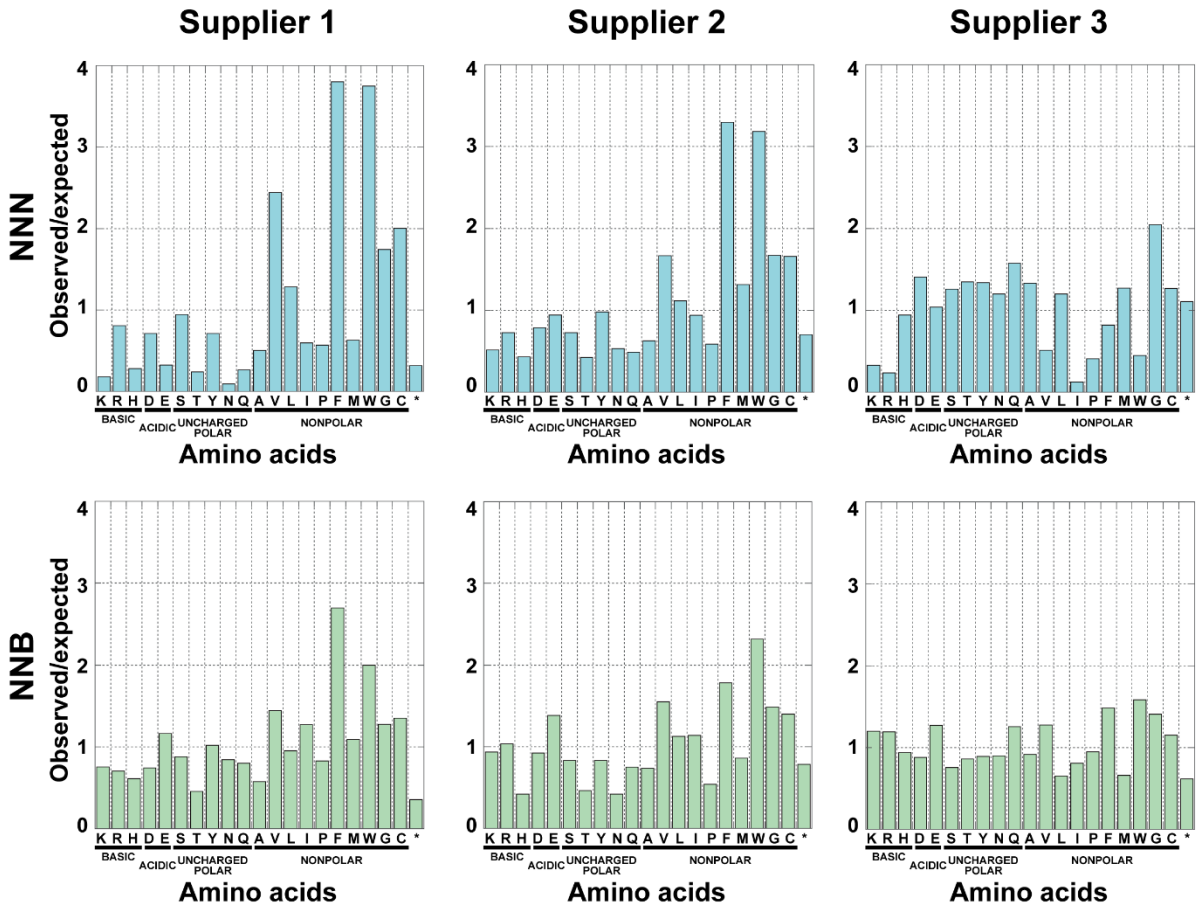

Figure 17. Observed/expected ratios for 20 amino acids in primer sets from each supplier determined by deep sequencing. All codons determined by deep sequencing were classified on the basis of 20 amino acids and stop codons. Observed/expected ratios are depicted in each histogram. The histograms of NNN and NNB primer sets are colored light blue (top) and light green (bottom), respectively.

Biases were relatively less severe in amino acids translated from NNB (Figures 16 and 17, bottom panels). Except for phenylalanine from supplier 1, and tryptophan, histidine, and asparagine from supplier 2, no amino acid ratios from NNB were more than twice as high or low from the expected values (Figure 17). The observed/expected ratios were nearly equal to 1 for each amino acid for supplier 3. Variances from NNB were lower than those from NNN, and, notably, the variance was lowest (0.08, Table 7) for supplier 3.

Table 7. Statistics of observed/expected ratios of 20 amino acids in each primer set, from each supplier, determined by deep sequencing.

primer	supplier	mean	variance	SD	median
NNN	1	1.06	1.20	1.10	0.63
	2	1.11	0.66	0.81	0.79
	3	1.01	0.25	0.50	1.20
NNB	1	1.04	0.29	0.53	0.88
	2	1.03	0.23	0.48	0.92
	3	1.03	0.08	0.28	0.94

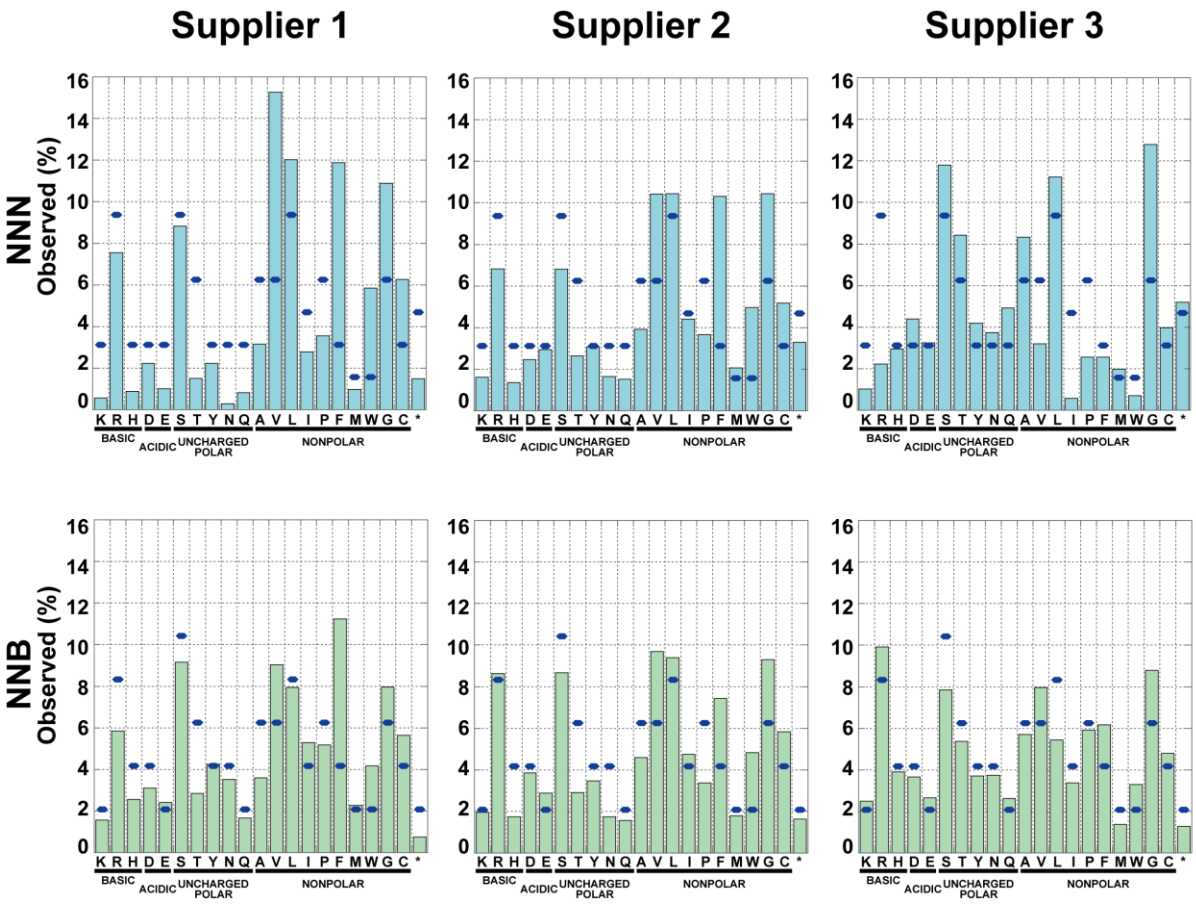

Figure 18. Observed fractions of each amino acid in NNN and NNB from three suppliers. All histograms show experimental amino acid fractions. Light blue: NNN (64 codons, top), green: NNB (48 codons, bottom). The thick horizontal lines (dark blue) on the histograms indicate expected amino acid fractions.

Overall, the observed and expected fractions of each amino acid from NNN and NNB codons showed wide variations (Figure 18). Ratios of mutations were significantly different among amino acids. However, observed fractions were relatively similar to the expected values in NNB codons from all three suppliers. Moreover, the variance among amino acid fractions was much lower for NNB than for NNN (Tables 7 and 8). As a result, frequencies of mutations from NNB were more uniform than from NNN. In terms of nucleotide, amino acid, and mutational biases, NNB codons were superior to NNN under the experimental conditions I evaluated. This was especially true of NNB from supplier 3.

In conclusion, the method of protein engineering evaluated in this chapter was based on one-pot saturation mutagenesis and robot-based automated screening. According to the nucleotide and amino acid biases in my gain-of-function GFP mutant experiments, the NNB primer was much more useful than the NNN primers for multisite saturation mutagenesis. The least-biased NNB primer was obtained from supplier 3 and this supplier was used to synthesize the degenerate primers in Chapter 4. In this study, I have not attempted to use other degenerate primers, such as NNK and NNS. The NNK and NNS primers contain only 32 codons, including one stop codon, therefore incorporating less redundancy than NNB. On the other hand, NNB is better in introducing a lower probability of stop codon (NNB = 1/48 and NNK or NNS = 1/32)[90]. However, it is unclear whether the NNB or NNK approach would be better.

Table 8. Statistics of each experimental fraction of 20 amino acids in each primer set, from each supplier, determined by deep sequencing.

primer	supplier	mean (%)	variance (%)	SD (%)	median (%)	stop codon (%)
NNN	1	4.93	21.4	4.63	2.90	1.49
	2	4.84	10.7	3.27	3.79	3.29
	3	4.74	13.9	3.73	3.50	5.19
NNB	1	4.96	7.78	2.79	4.21	0.74
	2	4.92	8.47	2.91	4.22	1.63
	3	4.94	5.31	2.30	4.35	1.28

Chapter 4

Combined screening approach to identify highly-active mutant of processive chitinase

1. Introduction

By using single-molecule imaging analysis, my group previously determined kinetic parameters of elementary reaction steps and chemo-mechanical coupling mechanism of the most studied processive chitinase, chitinase A from the gram-negative bacterium *Serratia marcescens* (*Sm*ChiA)[17, 54, 91]. As described in Chapter 2, I further revealed that the F232W and F396W mutations at the beginning and end of the substrate-binding catalytic cleft decrease dissociation rate constant of productively-bound enzyme and increase processivity, and result in high catalytic activity[55, 91]. Based on the multiple sequence alignment of the *Sm*ChiA and 257 *Sm*ChiA-like proteins, I also found that neither Phe232 nor Phe396 are predominant but tryptophan. Our previous study strongly suggested that, although *Sm*ChiA is the most studied processive chitinase, its amino acid sequence is not optimized for high hydrolytic activity.

Although the site-saturation mutagenesis is widely used, generally, only a few fractions of generated mutants are found to be improved as most of them show lower stabilities and activities than the wild-type, and low expressions and/or aggregations in the host cells. To improve this drawback, bioinformatics approach also plays an important role in mutation site designation and in reducing the number of mutation trials. For instance, a new method known as PROSS, which uses advanced bioinformatics analyses to design high protein expression and stability, has been reported recently[92]. This method can predict an optimal amino acid sequence of a target enzyme based on the multiple sequence alignment and calculation of the Gibbs free energy difference ($\Delta\Delta G$) between wild-type and single-site mutant by using the Rosetta software[93-94]. However, it only suggests the amino acid mutations found in the multiple sequence alignment of natural enzymes and does not explore the possibility of other amino acids which do not appear in the alignment.

In this Chapter, I combined multiple sequence alignment, site-saturation mutagenesis, and

automated screening with a liquid-handling robot to further improve the hydrolytic activity of *Sm*ChiA. By using previously reported high-catalytic activity mutant (F232W/F396W) as a template, I successfully identified S538V mutant among 8 positions tried (Figure 19). The F232W/F396W/S538V mutant showed higher hydrolytic activity than the F232W/F396W at all crystalline chitin concentrations tried, and higher turnover number (k_{cat}) than the F232W/F396W. Importantly, valine was not found in the multiple sequence alignment at the Ser538 position of *Sm*ChiA. These results indicate that my combination method is an effective approach for generating high-catalytic activity mutants of enzymes.

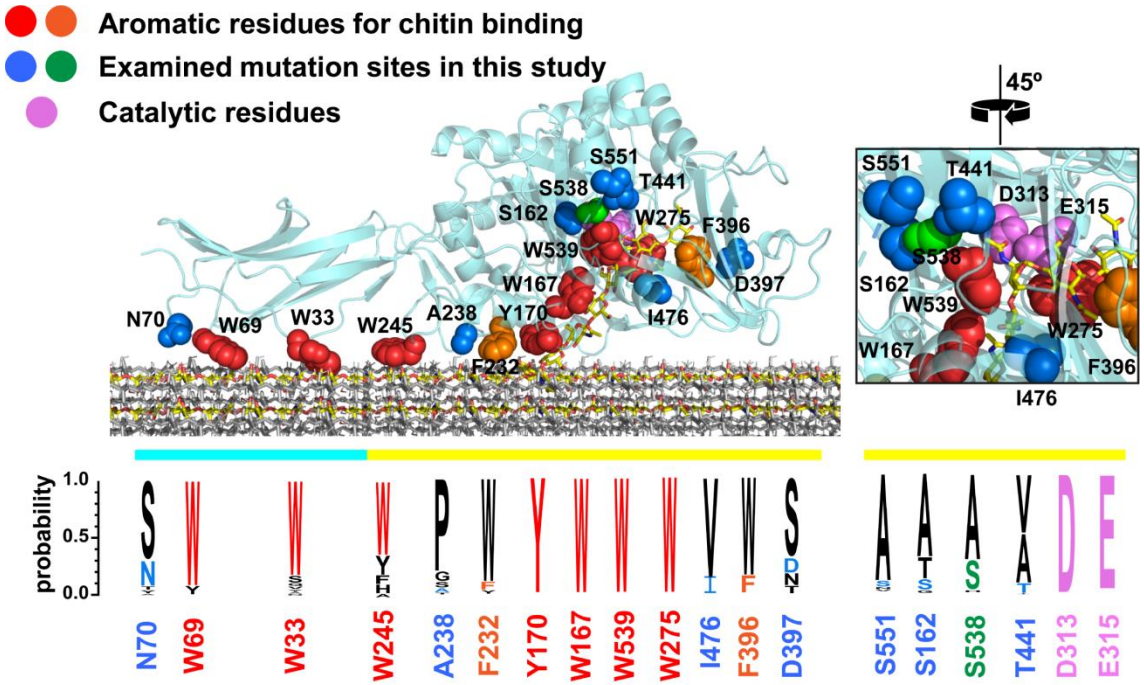

Figure 19. Model structure of *Sm*ChiA bound to crystalline chitin, important residues for binding and catalysis, and residues mutated in this study
(Top) A crystal structure of *Sm*ChiA (PDB entry 1CTN; ribbon model) aligned with the crystalline chitin chains (stick model). Amino acid residues responsible for binding to chitin (red and orange), catalytic residues (pink), and examined mutation sites (blue and green) are highlighted with sphere models. An expanded image around the catalytic site is also shown (right). The cyan and yellow bars under the structure indicate the binding and catalytic domains, respectively. (Bottom) Result of multiple sequence alignment for amino acid residues highlighted in top. The residues of *Sm*ChiA are shown in the same color as the top. The alignment result of the whole sequence is shown in Figure 21.

2. Materials and Methods

Figure 20 shows an overview of our combined method of screening. It consists of the preparation of site-saturated mutation library, expression in *E. coli*, protein purification with a liquid-handling robot, enzyme concentration estimation by SDS-PAGE, measurement of hydrolytic activity with the liquid-handling robot, and sequence analysis by using colony PCR. Single cycle of screening for each mutation site can be completed in 5-6 days.

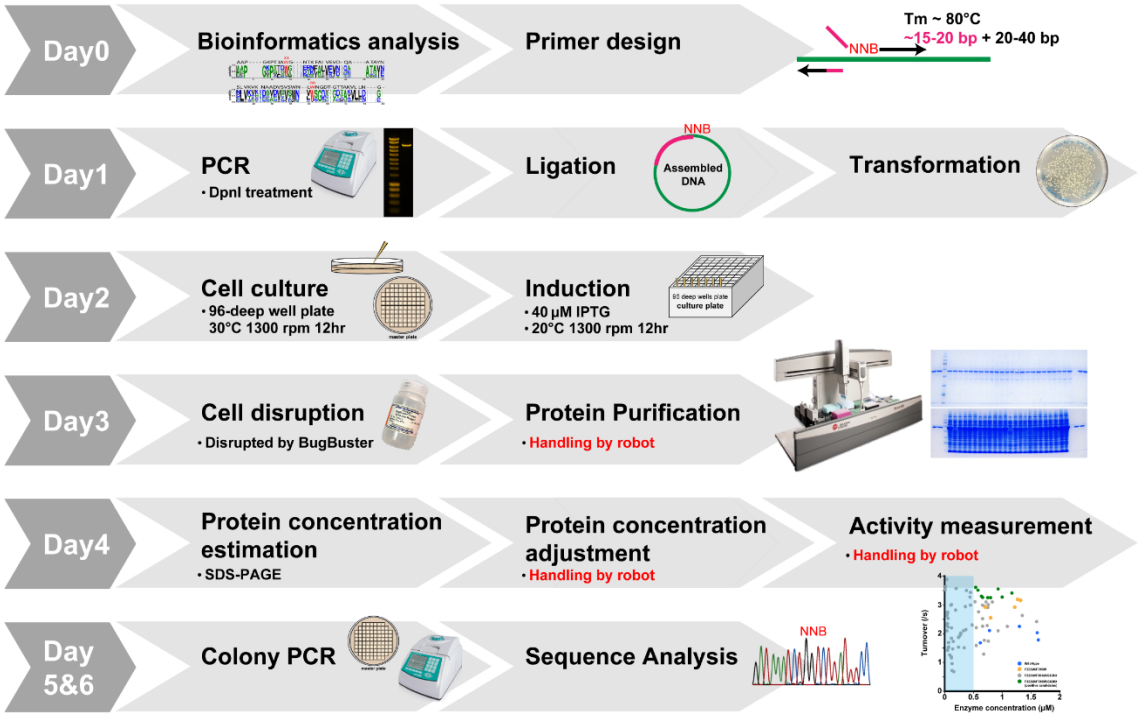

Figure 20. Overview of experimental procedures for site-saturation mutagenesis and robot-based screening.

Multiple sequence alignment

The multiple sequence alignment was performed as described previously[91]. Briefly, amino acid sequences of *Sm*ChiA and 257 *Sm*ChiA-like proteins from the different organisms were obtained using the NCBI database Protein BLAST tool (http://blast.ncbi.nlm.nih.gov). Before

alignment, signal sequences were removed according to the prediction of SignalP 5.0[57] (http://www.cbs.dtu.dk/services/ SignalP), with the appropriate organism group for prediction. The sequences for which SignalP could not predict the signal sequences were excluded from the alignment. The amino acid sequences of *Sm*ChiA and 257 *Sm*ChiA-like proteins were aligned and visualized using Clustal Omega[58] (Clustalω: http://www.ebi.ac.uk/Tools/msa/clustalo) and WebLogo[59] (http://weblogo.threeplusone.com), respectively.

Site-saturation mutagenesis

The primers were designed according to our previous report[60]. The PCR reactions were carried out using the KOD One™ PCR Master Mix (TOYOBO, Japan) as follows: 25 μL KOD One™ premix, 22 μL MilliQ water, 1 μL of each 10 pmol/μL forward and reverse primers, and 1 μL of 1 ng/μL DNA template plasmids (*Sm*ChiA_F232W/F396W with the C-terminal Factor Xa (FaXa) recognition sequence and 6-histidines tag and without signal peptide (23 amino acid residues) at the N-terminal in pET27b). A Life ECO thermocycler (Bioer Technology, China) was used with the following protocol: 30 s at 98 °C of initial denaturation followed by 25 cycles at 98 °C for 10 s, at 55 °C for 5 s, and at 72 °C for 1 min, finalized by a further extension cycle at 72 °C for 2 min. The PCR products were treated with 2 μL of DpnI (New England Biolabs, NEB, USA) for 40 min at 37 °C to eliminate the leftover DNA template. All DpnI-treated PCR products were loaded for electrophoresis on 1 % Agarose gel. The products of the expected size were extracted and purified using a commercial gel extraction kit (Promega, USA).

The purified DNA fragments were ligated using the NEBuilder® HiFi DNA assembly (NEB, USA). The DNA fragments and NEBuilder reagent were mixed at a 1:1 (v/v) ratio (the final DNA fragment concentration was 20 ng/μL), then incubated at 50 °C for 1 hour. One

microliter of the ligation reaction was added to 50 μL of Tuner DE3 *E. coli* competent cells and put on ice for 1 min before pulsing with electroporator (Micropulser, Bio-Rad, USA). Then, 200 μL of SOC medium was added to the suspension of transformed cells immediately after the electroporation, and cells were incubated at 37 °C for 1 hour before spreading on LB-Agar plates containing 25 μg/mL kanamycin. The plates were incubated overnight (approximately 16 hours) at 37 °C.

Small-scale culture and enzyme purification

Eighty-five colonies of freshly transformed *E. coli* were picked and cultured in 1 mL of Super Broth (SB) medium (3.2 % Bacto tryptone, 2 % yeast extract, and 0.5 % NaCl) supplemented with 25 μg/mL kanamycin in 96-deep-well plates (P-2ML-SQ-C, Axygen, USA). Prior to inoculation into the medium described above, all colonies were also inoculated on an LB-Agar plate containing 25 μg/mL kanamycin in order to prepare a master plate. Five colonies expressing the WT and five colonies expressing the F232W/F396W were also picked as the controls. The last well was left blank to check contamination across the well. The picked cells were cultured at 30 °C and shaken at 1,300 rpm for 12 hours. The cells were cooled down on iced water for 10 minutes before being induced with 0.4 mM. isopropyl β-D-1-thiogalactopyranoside (IPTG). Then the cells were cultured by shaking at 1,300 rpm at 20 °C for another 12 hours and harvested by centrifugation at 4,400 *g*, at 25 °C for 10 min. The supernatants were discarded.

The cell disruption and protein purification were performed using the Beckman Coulter Biomek 4000 liquid-handling robot (USA). Briefly, 300 μL of the BugBuster reagent (Novagen, Germany) supplemented with 10 units/mL of Benzonase (Novagen, Germany) was added to each well to disrupt the cells. Then the 96-deep-well plate was shaken at 1,000 rpm for 20 min

at 25 °C. The disrupted cells were then centrifuged at 4,400 *g* at 25 °C for 10 min. The supernatant was transferred into a new 96-deep-well plate, then 100 µL of Ni-NTA agarose (QIAGEN, Germany) was added to each well and mixed by shaking at 1,000 rpm for 5 min in order to facilitate binding of *Sm*ChiA mutants with 6-histidines tag. The Ni-NTA mixtures were then transferred to a filter plate (AcroPrep Advance Filter Plates for Aqueous Filtration - 30-40 µm PP/PE non-woven media, PALL, USA) on the collection plate. The liquid was filtered through the filter plate using vacuum. The Ni-NTA agarose was washed twice with 200 µL of 50 mM sodium phosphate buffer pH 7.0 with 100 mM sodium chloride and washed three times with 200 µL of 50 mM sodium phosphate buffer pH 7.0 with 100 mM sodium chloride and 50 mM imidazole. Before elution, the bottom of the filter plate was wiped with a paper, and the collection plate was replaced with the new 96-deep-well plate (P-2ML-SQ-C, Axygen, USA). Then the samples were eluted with 50 mM sodium phosphate buffer pH 7.0 with 100 mM sodium chloride and 100 mM imidazole.

SDS-PAGE, protein concentration estimation

Ten microliters of purified samples from each well were mixed with 5 µL of the sample buffer (62.5 mM Tris-HCl pH 6.8, 2.5% SDS, 0.002% bromphenol blue, 5% β-mercaptoethanol, and 10% glycerol). The cell pellets were shaken in the remaining BugBuster reagent at 1,300 rpm for 20 minutes to re-suspend. Two microliters of cell pellet suspension were mixed with 5 µL of the sample buffer. Both purified samples and cell pellets suspension mixtures were boiled at 95 °C for 5 min before loading them on 12% acrylamide gel. One or two micromolar WT *Sm*ChiA, purified separately from the large scale culture, was loaded in 4 lanes of each gel as references for concentration determination.

After the SDS-PAGE, gels were stained with a staining solution (100 mg Coomassie Brilliant Blue G-250 (Tokyo Chemical Industry), 3 mL hydrochloric acid, and 1 L MilliQ water), and then de-stained with clean water overnight to reduce the background level. Then images of the gel were taken using a gel documentation system (WSE-5400 Printgraph Classic, ATTO, Japan), and target protein concentrations were determined using an image analysis software (CS Analyzer 4, ATTO, Japan). The band intensities were analyzed and compared with the *Sm*ChiA-WT references to estimate the concentration of each sample.

Chitin hydrolytic activity measurement of each mutant

For chitin hydrolytic activity measurement, the protein concentration of each sample was diluted to 100 nM with 100 mM sodium phosphate buffer (pH 6.0) in a 96-well low-protein-binding plate (PCR plate 96 LoBind-semi-skirted, Eppendorf, Germany), by using the same liquid-handling robot used for cell disruption and protein purification. The hydrolytic activity was also measured using the same liquid-handling robot. Seventy-five microliters of 100 nM enzymes in sodium phosphate buffer (pH 6.0) were mixed with 75 μL of 1 mg/mL crystalline chitin suspension (prepared as described previously[31]) in a 96-well reaction plate (RTP 6001-20 Bio Chromato., Inc, Japan). Then, the plate was incubated at 25 °C for 30 min without shaking, and reactions were stopped with 200 μL Schales's reagent (500 mM sodium carbonate, 1.5 mM potassium ferricyanide). The crystalline chitin was separated on the 96-well 1.2 μm hydrophilic low-protein-binding Durapore® membrane filter plate (Merck Millipore, Germany). The filtered solutions were transferred to a PCR-96-well plate (PCR-96-PE2, BMBio, Japan), then incubated at 95 °C for 15 min. Then, 100 μL of the heated samples were transferred into a 384-well clear plate (784061, Greiner bio-one, USA). The absorbance at 420 nm was measured using a multimode microplate reader (SpectraID3, Molecular Devices, USA). The

concentration of reaction products was calculated from the standard curve prepared with chitobiose. The hydrolytic activities of each sample at each site were plotted against their concentrations and compared with those of the WT and the F232W/F396W. To assure the reliability of the measurement, the samples which showed a concentration below 0.5 μM were excluded from further analysis. To confirm the reproducibility of the measurement, average values, and standard deviations of the hydrolytic activities of the WT and the F232W/F396W were determined for each screening. The relative values of the standard deviations were typically about 10% of the average values.

High-activity mutant candidates were picked from the master plate for colony PCR using T7-promoter and T7-terminator primers. The colony PCR was carried out with KOD One™ PCR Master Mix (TOYOBO, Japan). The mixture consisted of 25 μL KOD One™ premix, 23 μL MilliQ water, 1 μL of each 10 pmol/μL T7-promoter and T7-terminator primers, and the designated colonies were picked into the mixture. Colony PCR products were purified using a commercial PCR clean-up system (Promega, USA) and the purified DNA sequences were then examined by FASMAC Co., Ltd (Japan).

The hydrolytic activities of the candidates with verified sequences were confirmed by repeating the cultivation, purification, and activity measurements. After the transformation of the plasmid containing each candidate mutant, 12 colonies were picked for each mutant and cultured in the 96-deep-well plate, and used for subsequent purifications and activity measurements by using the liquid-handling robot.

Large-scale culture and enzyme purification

The verified plasmid containing the WT, F232W/F396W, or F232W/F396W/S538V gene was transformed into Tuner (DE3) competent cells as described above. Single colonies were inoculated into 10 mL of LB medium supplemented with 25 μg/mL kanamycin and incubated overnight at 37 °C and 250 rpm. Then, all of the pre-culture was added to 1 L of LB medium supplemented with 25 μg/mL kanamycin in a 3-liter flask and cultured at 37 °C and 130 rpm until $O.D._{600}$ = 1.8. Then the media were cooled on iced water for 10 min before being induced with 500 μM IPTG. The cells were further cultured at 20 °C and 130 rpm overnight. The culture was then centrifuged at 6,000 *g* for 10 min. Ten times volume of the cell weight of 50 mM sodium phosphate buffer (pH 7.0) with 100 mM sodium chloride was added and supplemented with protease inhibitor cocktail (cOmplete Mini, EDTA-free, Roche Applied Science, Switzerland). The cell suspension was sonicated on ice for 20 min at 3-s intervals. The disrupted cells were centrifuged at 4 °C and 30,000 *g* for 20 min. The supernatant was collected, incubated with Ni-NTA agarose (QIAGEN, USA), and equilibrated with 50 mM sodium phosphate buffer pH 7.0 containing 100 mM sodium chloride for 15 min at 25 °C under gentle rotation. The Ni-NTA agarose was packed into an open column and washed with 0 and 50 mM imidazole in 50 mM sodium phosphate buffer (pH 7.0) containing 100 mM sodium chloride. Then the enzyme was eluted with 100 mM imidazole in 50 mM sodium phosphate buffer (pH 7.0) containing 100 mM sodium chloride. The designated eluted fractions were mixed and concentrated to 500 μL using a 30,000 molecular weight cut-off Vivaspin Turbo 50 (Sartorius). To further purify and remove the imidazole in solution, the samples were then injected into a Superdex 200 10/300 GL column (GE Healthcare, USA) and eluted with 50 mM sodium phosphate buffer (pH 7.0) containing 100 mM sodium chloride at a flow rate 0.5 mL/min. The eluted fractions were mixed, and their concentration was estimated from their absorbance at

280 nm (molar extinction coefficient of 107,050 $M^{-1}cm^{-1}$ was used for the WT, and that of 118,050 $M^{-1}cm^{-1}$ was used for both the F232W/F396W and F232W/F396W/S538V). The molar extinction coefficients were calculated from the ProtParam in the ExPASy bioinformatics resource portal web service. The samples were then divided into small fractions and stored at -80 °C until further use.

Hydrolytic activity measurement to estimate k_{cat} and K_m

The same liquid-handling robot was used to measure the hydrolytic activities of the WT, F232W/F396W, and F232W/F396W/S538V at various concentrations of the crystalline chitin to estimate k_{cat} and K_m. The samples were measured in triplicate simultaneously in 96-well plates. The purified enzymes were diluted to 100 nM with 100 mM Na-phosphate (pH 6.0) in a low-protein-binding microtube (MS-4215M Sumitomo Bakelite, Japan). In 96-well reaction plates, the diluted enzymes were incubated with crystalline chitin (0-6 mg/mL) at 25 ºC for 30 min in a reaction mixture with the volume of 150 μL (75 μL of enzyme solution and 75 μL crystalline chitin suspension were mixed) without shaking. The reactions were stopped with 200 μL of the Schaless reagent. Crystalline chitin was separated on the 96-well 1.2 μm Hydrophil low protein binding Durapore® membrane filter plate (Merck Millipore). The filtered solution was incubated at 95 ºC for 15 min and 100 μL of the samples were transferred to a 384-well clear plate. Absorbance at 420 nm was measured using a multi-mode microplate reader (SpectraMax iD3, Molecular Devices). The concentration of reaction products was calculated from the standard curve prepared with chitobiose. The error bars shown in Figure 32 represent the standard deviations of the triplicated measurements.

3. Results and Discussion

To identify amino acid residues which are not conserved in the binding and catalytic domains of *Sm*ChiA, I obtained amino acid sequences of the 257 *Sm*ChiA-like proteins from the BLAST analysis and aligned them with that of the *Sm*ChiA by Clustal-Omega. I found that the aromatic residues at the substrate-binding site of the binding and catalytic domains are highly conserved among *Sm*ChiA and *Sm*ChiA-like proteins. *Sm*ChiA has predominant aromatic residues such as tryptophan and tyrosine (Figure 19 and Figure 21, red), except for Phe232 and Phe396 (orange) as recently reported[91]. Interestingly, Tyr170, Trp167, Trp275, and Trp539 in the catalytic cleft of *Sm*ChiA were completely conserved among the 258 proteins. Furthermore, as expected, two catalytic residues Asp313 and Glu315 (pink) were also completely conserved.

In addition to the conserved and non-conserved aromatic residues described above, I also found several non-conserved amino acid residues both in the binding and catalytic domains of *Sm*ChiA. I selected 8 non-conserved residues close to the aromatic residues responsible for the chitin binding or near the catalytic site as potential mutation targets (Figure 19 and Figure 21, blue and green). Asn70 is next to an aromatic residue in the binding domain, Ala238 is near the aromatic residue at the entrance of the catalytic cleft, Asp397 is next to an aromatic residue at the product release site, Ser551 is at the surface of the catalytic domain, and Ser162, Thr441, Ile476, and Ser538 are inside the catalytic cleft. I also confirmed the suggestions by the PROSS for these target sites and compared them with our alignment (Table 9). Except for one site which was not suggested, the amino acid residues suggested by the PROSS were the predominant amino acids in the alignment. This result strongly suggests that only the sequence alignment without the Rosetta energy calculation could already be enough for the *Sm*ChiA mutation site designation.

Table 9. Comparison of predominant amino acid residues in the multiple sequence alignment and amino acid residue suggested by the PROSS.

*Sm*ChiA position	Predominant amino acid in the alignment	PROSS suggestion	High-activity mutant
N70	S	S	-
S162	A	A	-
A238	P	P	-
D397	S	-[1]	-
T441	V	V	-
I476	V	V	-
S538	A	A	V[2]
S551	A	A	-

[1]Not suggested by the PROSS for this amino acid residue

[2]Newly identified high-activity mutant in the present study

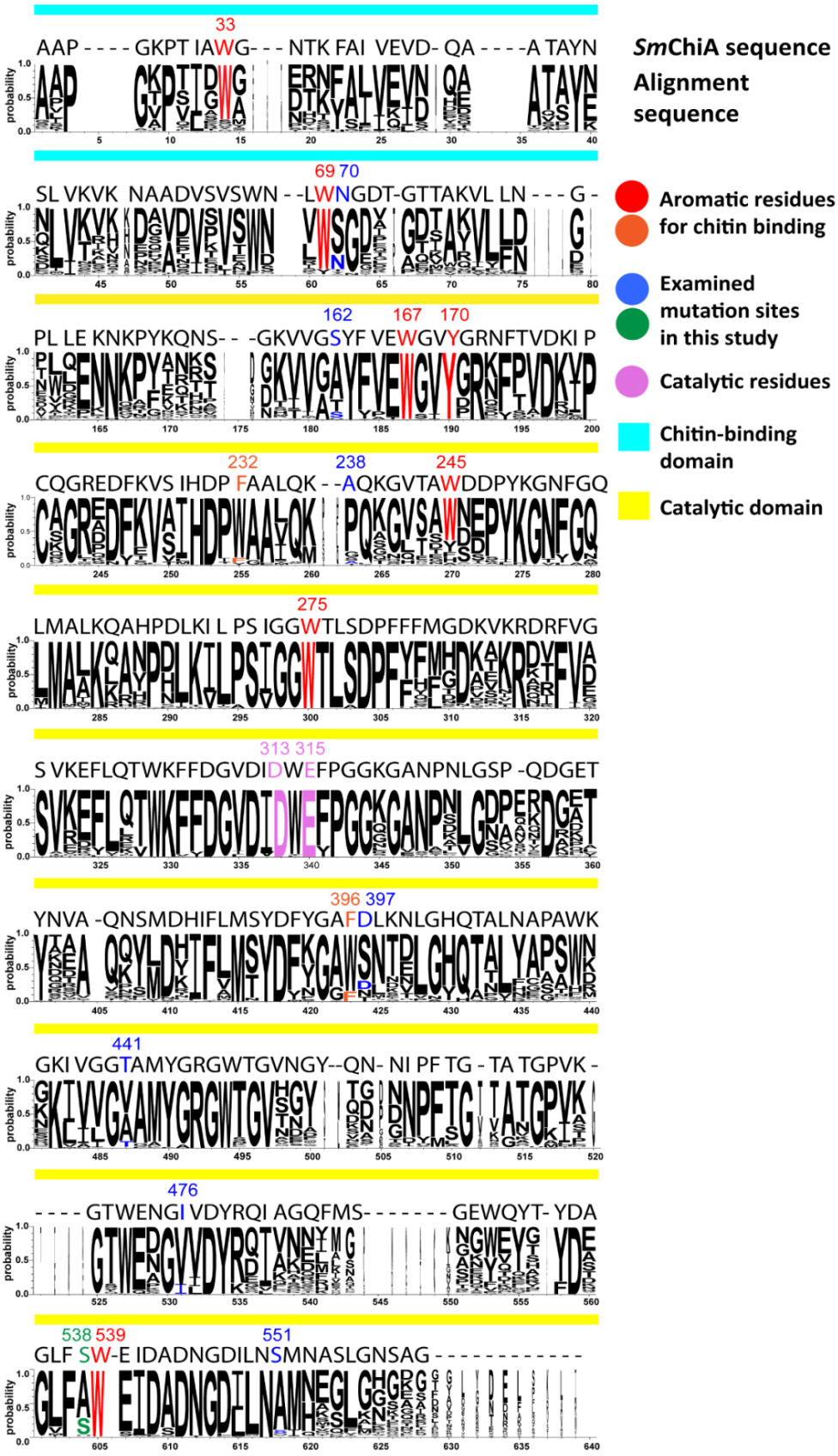
33
AAP - - - - GKPT IAWG- - - NTK FAI VEVD- QA - - - -A TAYN
69 70
SL VKVK NAADVSVSWN - -LWNGDT-GTTAKVL LN - - - G -
162 167 170
PL LE KNKPYKQNS- - -GKVVGSYF VEWGVYGRNFTVDKI P
232 238 245
CQGREDFKVS IHDP FAALQK - -AQKGVTAWDDPYKGNFGQ
275
LMALKQAHPDLKI L PS IGGWTLSDPFFFMGDKVKRDRFVG
313 315
S VKEFLQTWKFFDGVDIDWEFPGGKGANPNLGSP -QDGET
396 397
YNVA -QNSMDHIFLMSYDFYGAFDLKNLGHQTALNAPAWK
441
GKI VGGTAMYGRGWTGVNGY--QN- NI PF TG - TA TGPVK -
476
- - - - GTWENGI VDYRQI AGQFMS- - - - - - GEWQYT- YDA
538 539 551
GLF SW-E IDADNGDILNSMNASLGNSAG - - - - - - - - - - -
probability
*Sm*ChiA sequence
Alignment sequence
Aromatic residues for chitin binding
Examined mutation sites in this study
Catalytic residues
Chitin-binding domain
Catalytic domain

Figure 21. The multiple sequence alignment of *Sm*ChiA and 258 *Sm*ChiA-like proteins.
The amino acid sequences of the *Sm*ChiA and 257 *Sm*ChiA-like proteins were aligned and visualized by Clustal-Omega[58] and WebLogo3[59], respectively. The sequence above the alignments represents the sequence of the *Sm*ChiA. The aromatic amino acid residues responsible for the binding to the crystalline chitin chain are shown in red and orange. The orange indicates F232 and F396, the positions at which a high catalytic activity mutant (F232W/F396W) was identified in the previous studies[55, 91]. The catalytic residues (D313 and E315) are shown in pink, and the mutation sites examined in this study are shown in blue and green. The green indicates S538, the position at which new high catalytic activity mutant (F232W/F396W/S538V) was identified in this study. The cyan and yellow bars above the alignment indicate the chitin-binding and catalytic domains, respectively.

To generate site-saturated mutation libraries, I used NNB codon (where B = T/G/C) degenerate primers. The primers with degenerate codons were designed and ordered with the least bias supplier as described previously[60]. Since I aimed at covering all 20 amino acids, reducing the probability of stop codon (NNB is 1/48 while NNK is 1/32, where K = G/T)[90], and simplifying the protocol as much as possible, the NNB codon degeneracy seemed to be the best way. In Chapter 3 (our previous study[60]), I used the SLiCE[84-85] in the ligation step as it is simple and low cost. In this Chapter, I used the NEBuilder® HiFi DNA assembly[86-87] instead of the SLiCE as it showed higher efficiency in the ligation step in the process of protocol optimization (data not shown), although it has a higher cost than the SLiCE.

For purification of *Sm*ChiA mutants from *E. coli* colonies and hydrolytic activity measurements of purified mutants, I applied a liquid-handling robot which handles 96-well plates. As I aimed at covering all 20 amino acids at each site in my screening, I thought that four times the 20 amino acids or 80 colonies should be screened at least. As controls, I also used 5 WT and 5 F232W/F396W mutant colonies in each cycle of screening. In short, in one 96-well plate, I picked 85 colonies expressing the mutants, 5 colonies of the WT, 5 colonies of the F232W/F396W mutant, and 1 well was left blank. Note that my screening size (85 colonies) is consistent with the calculation of the TopLib analysis[90]; the expected screening size of 87

colonies in order to cover 95% probability to find the top one best mutant using NNB codon degeneracy.

After the protein purification by the liquid-handling robot, the purity of the soluble protein was confirmed by the SDS-PAGE (Figure 22 to 29). Although I used one-step affinity purification of the *Sm*ChiA mutants with 6-histidines tag at the carboxyl terminal, purity of the soluble protein was high. I also checked solubility of each mutant by the SDS-PAGE of the insoluble proteins in the cell pellets. I found that the mutations near the catalytic site (Ser538, Ser162, and Thr441) showed a higher appearance of the full-length insoluble proteins compared with the other positions (Figure 22A, 24A, and 27A). As these positions are located inside the catalytic cleft, the space for side-chain packing is limited. The mutation that resulted in a large amino acid side chain might affect its folding ability and cause aggregation.

Then, I also estimated the ratio of stop codon incorporation in the site-saturated mutation library. Note that because I added 6-histidines tag at the carboxyl terminal of the *Sm*ChiA, only full-length proteins with a single-site mutation will be purified in the soluble fraction. The truncated mutants generated by the introduction of the stop codon will be recovered in the insoluble fraction as aggregated proteins. As results, I obtained the stop codon ratios of 8.2% (A238X), 11.8% (D397X), 7.1% (T441X), 7.1% (I476X), 4.7% (S538X), and 5.9% (S551X). Note that in the case of N70X and S162X, it was difficult to distinguish between the presence of the truncated proteins and the lack of expression as the expected sizes are small (5 kDa and 14.5 kDa, respectively) (Figure 23 and 24). All of these values were larger than the expected value, 2.1% (1/48 × 100) for the NNB codon. This result is inconsistent with Chapter 3 that the stop codon ratio in the supplier I used was less than the expected value, suggesting that the bias changes depending on the order lot of the primers[60]. Another possible reason for high ratio is

PCR error, because some truncated mutants showed the sizes different from the expected ones (D397X and T441X, Figure 26 and 27).

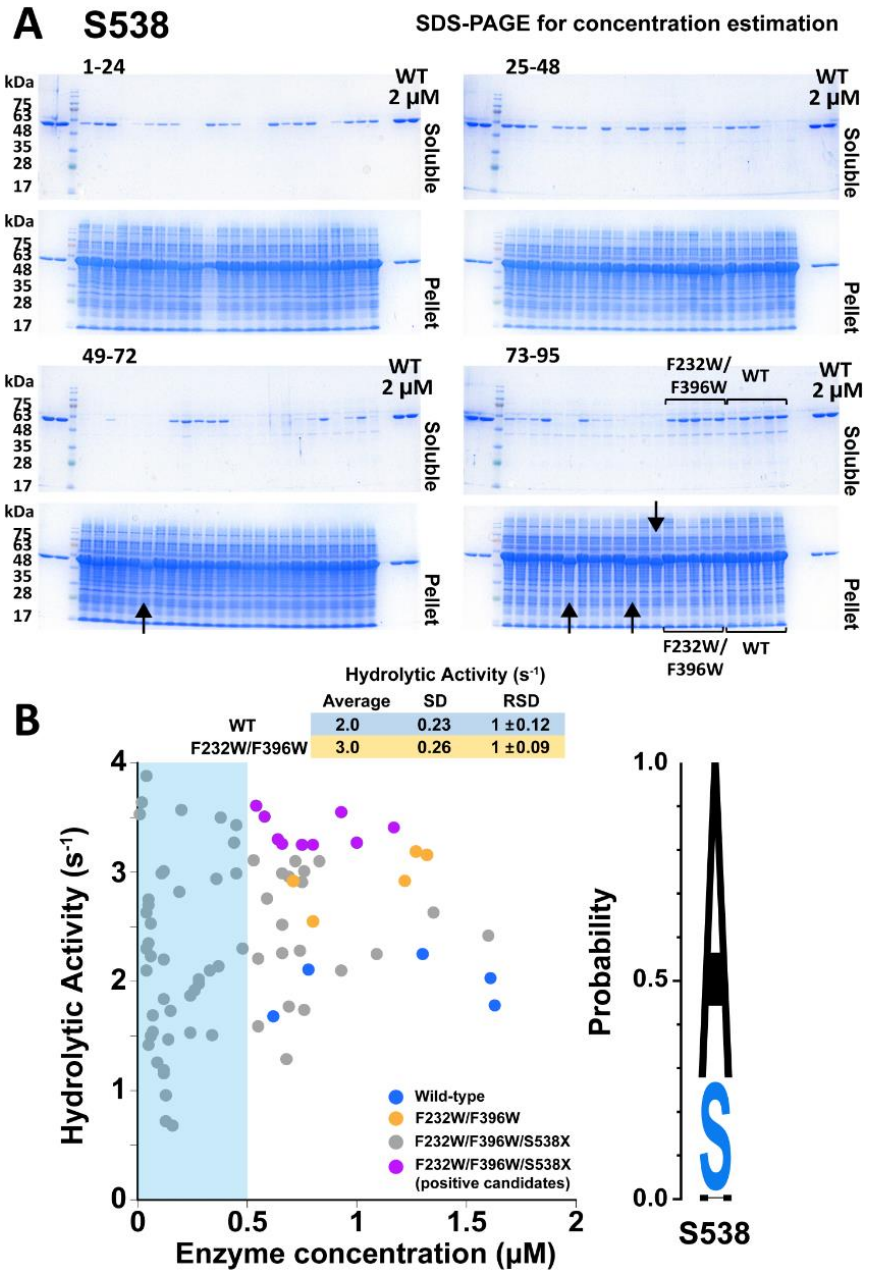

Figure 22. Screening result of S538 site.
(A) SDS-PAGE of purified protein (top, soluble) and cell pellet (bottom, pellet). The concentrations of the purified enzyme were estimated form the band intensity by comparing with that of the wild-type (WT) purified separately. The arrows indicate the truncated mutants in which the stop codons were incorporated. The stop codon ratio was 4.7% and higher than the expected ratio (2.1%). (B) Hydrolytic activity against purified enzyme concentration for each sample. Blue and orange dots represent the WT and F232W/F396W, respectively. Gray and purple dots represent F232W/F396W/S538X mutants and their high activity candidates, respectively. Crystalline chitin concentration was 0.5 mg/mL. Note that the enzyme concentration estimation is deemed unreliable at a concentration below 0.5 μM (region indicated by light blue box), and samples located in this region were excluded from further analysis.

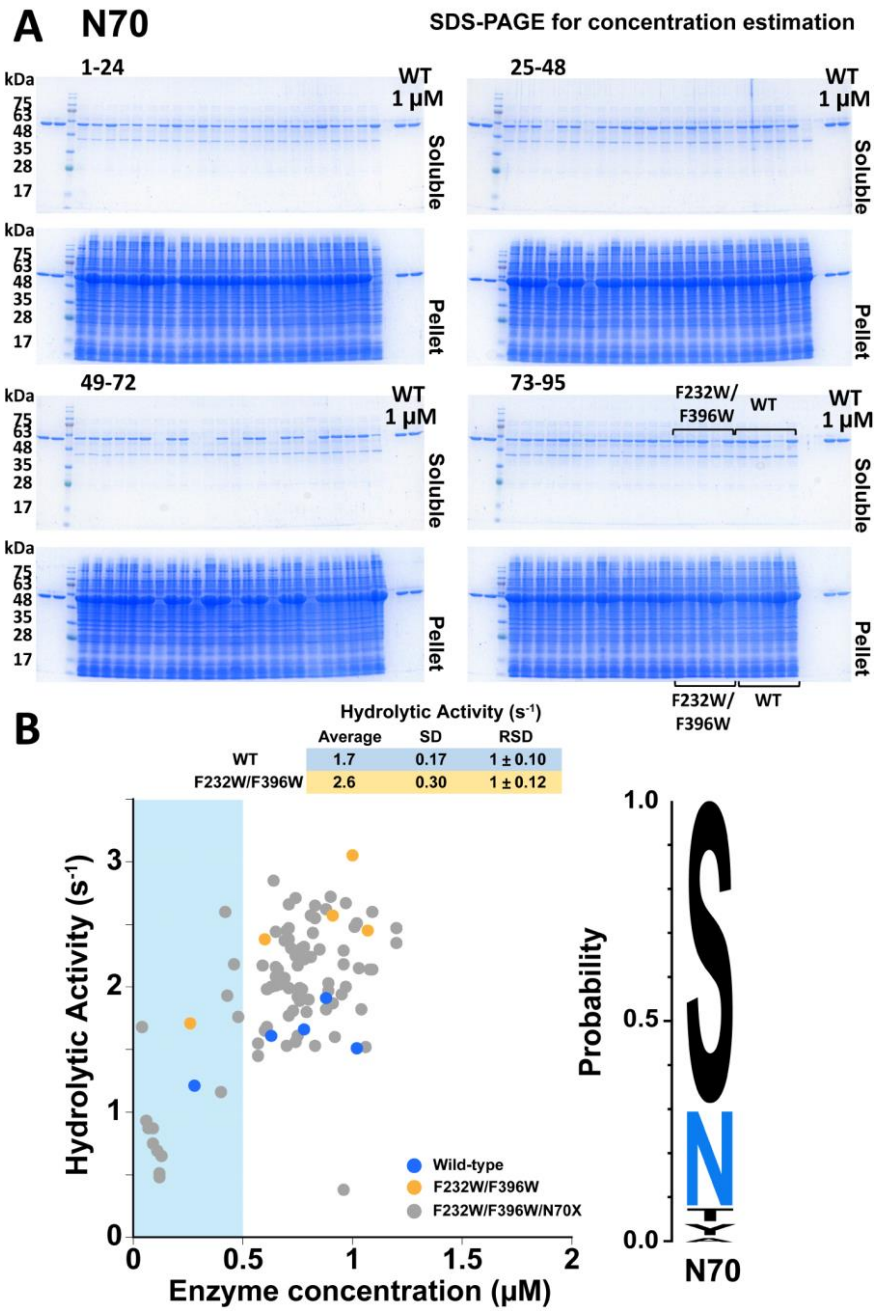

Figure 23. Screening result of N70 site.
(A) SDS-PAGE of purified protein (top, soluble) and cell pellet (bottom, pellet). The concentrations of the purified enzyme were estimated form the band intensity by comparing with that of the wild-type (WT) purified separately. Note that the truncated mutants generated by stop codon incorporation could not be identified due to its small size (5 kDa). (B) Hydrolytic activity against purified enzyme concentration for each sample. Blue, orange, and gray dots represent the WT, F232W/F396W, and F232W/F396W/N70X mutants, respectively. Crystalline chitin concentration was 0.5 mg/mL. Note that the enzyme concentration estimation is deemed unreliable at a concentration below 0.5 μM (region indicated by light blue box), and samples located in this region were excluded from further analysis.

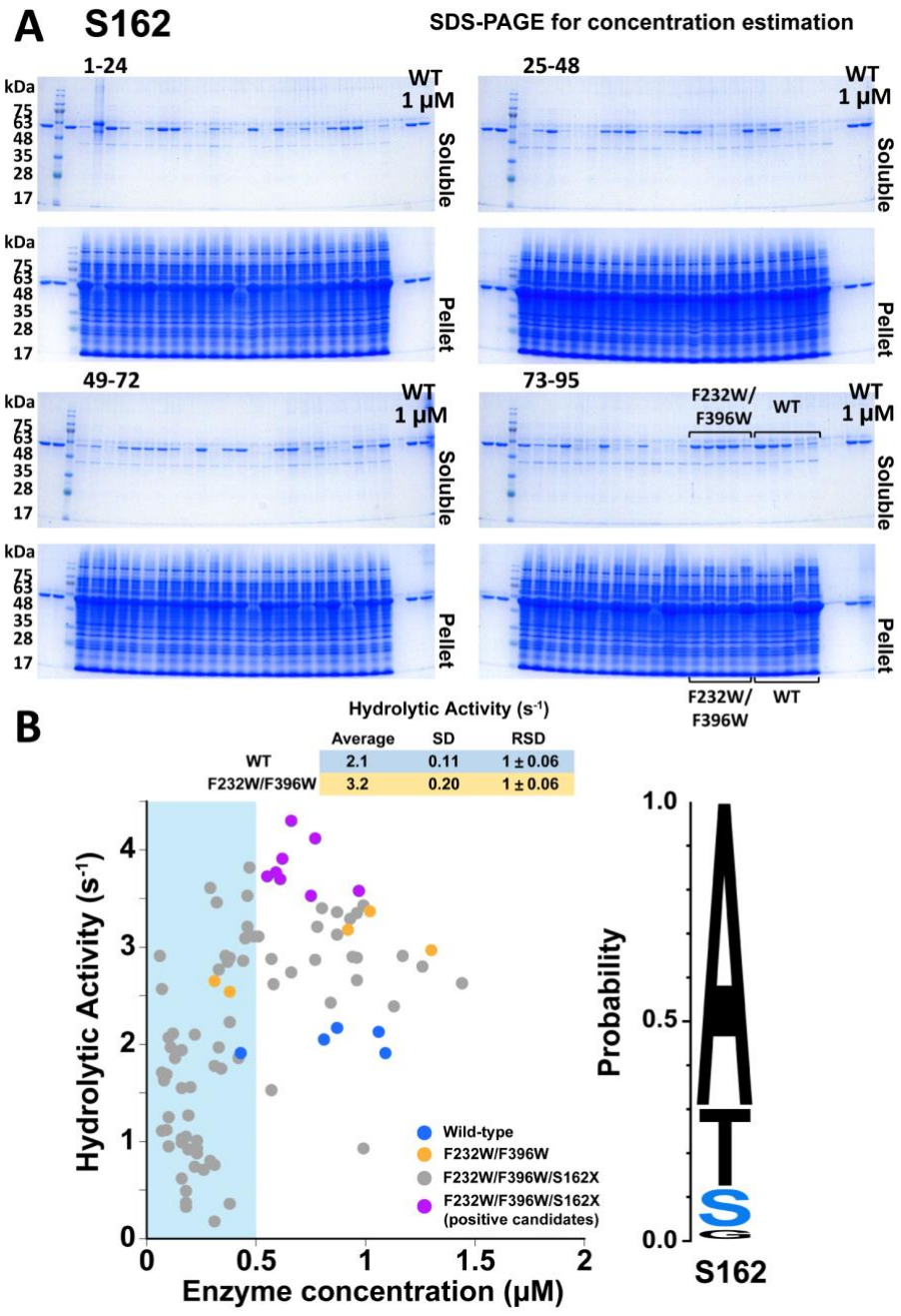

Figure 24. Screening result of S162 site.
(A) SDS-PAGE of purified protein (top, soluble) and cell pellet (bottom, pellet). The concentrations of the purified enzyme were estimated form the band intensity by comparing with that of the wild-type (WT) purified separately. Note that the truncated mutants generated by stop codon incorporation could not be identified due to its small size (14.5 kDa). (B) Hydrolytic activity against purified enzyme concentration for each sample. Blue and orange dots represent the WT and F232W/F396W, respectively. Gray and purple dots represent F232W/F396W/S162X mutants and their high activity candidates, respectively. Crystalline chitin concentration was 0.5 mg/mL. Note that the enzyme concentration estimation is deemed unreliable at a concentration below 0.5 μM (region indicated by light blue box), and samples located in this region were excluded from further analysis.

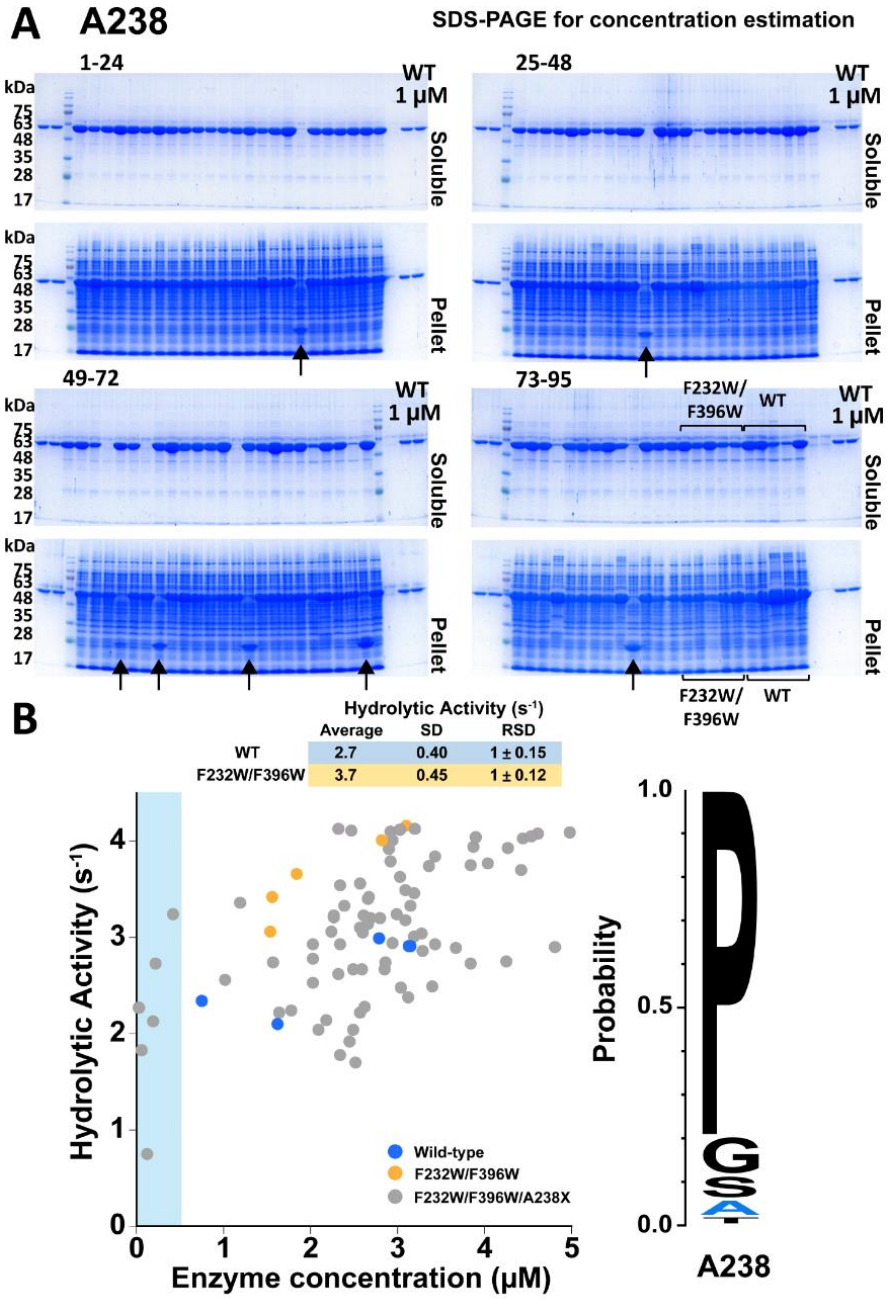

Figure 25. Screening result of A238 site.
(A) SDS-PAGE of purified protein (top, soluble) and cell pellet (bottom, pellet). The concentrations of the purified enzyme were estimated form the band intensity by comparing with that of the wild-type (WT) purified separately. The arrows indicate the truncated mutants in which the stop codons were incorporated. The stop codon ratio was 8.2% and higher than the expected one (2.1%). (B) Hydrolytic activity against purified enzyme concentration for each sample. Blue, orange, and gray dots represent the WT, F232W/F396W, and F232W/F396W/A238X mutants, respectively. Crystalline chitin concentration was 0.5 mg/mL. Note that the enzyme concentration estimation is deemed unreliable at a concentration below 0.5 μM (region indicated by light blue box), and samples located in this region were excluded from further analysis.

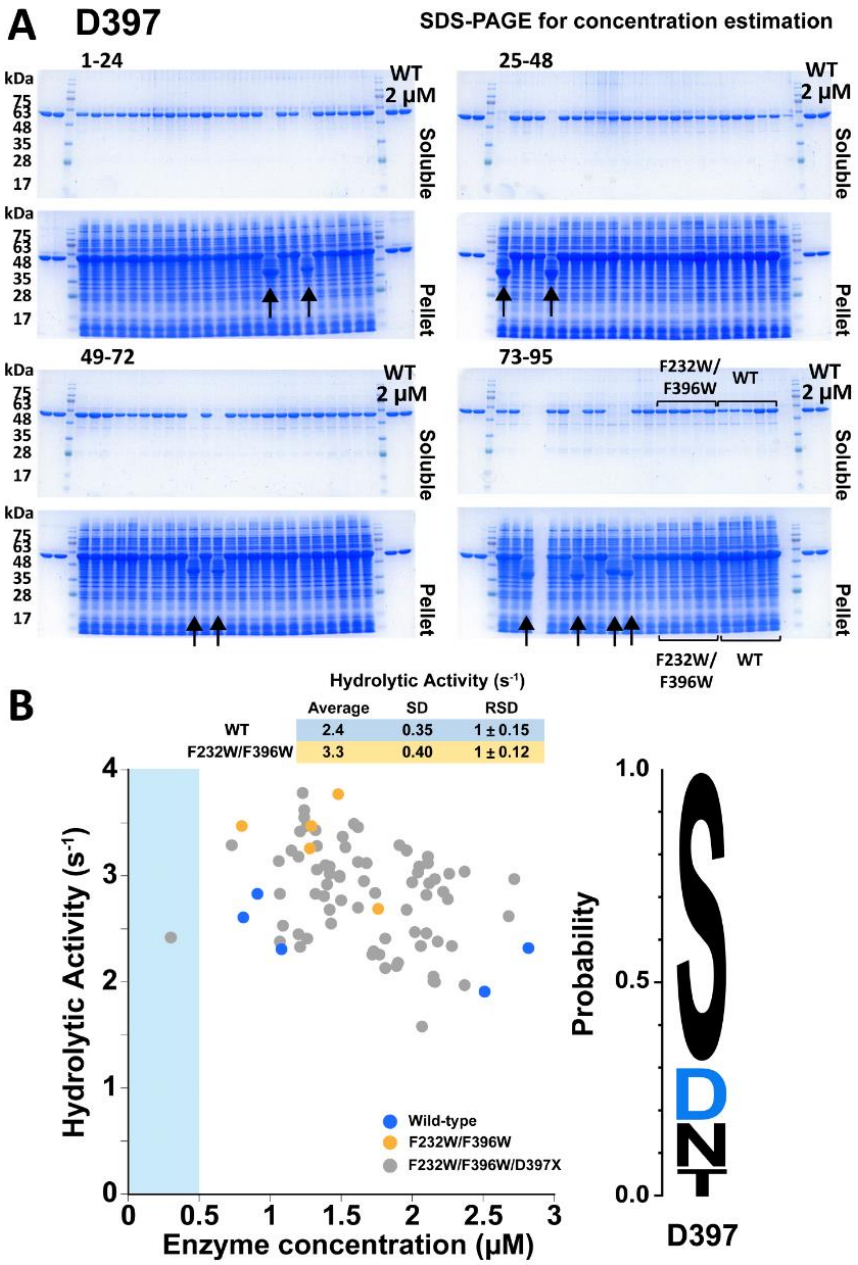

Figure 26. Screening result of D397 site.
(A) SDS-PAGE of purified protein (top, soluble) and cell pellet (bottom, pellet). The concentrations of the purified enzyme were estimated form the band intensity by comparing with that of the wild-type (WT) purified separately. The arrows indicate the truncated mutants in which the stop codons were incorporated. The stop codon ratio was 11.8% and higher than the expected one (2.1%). (B) Hydrolytic activity against purified enzyme concentration for each sample. Blue, orange, and gray dots represent the WT, F232W/F396W, and F232W/F396W/D397X mutants, respectively. Crystalline chitin concentration was 0.5 mg/mL. Note that the enzyme concentration estimation is deemed unreliable at a concentration below 0.5 μM (region indicated by light blue box), and samples located in this region were excluded from further analysis.

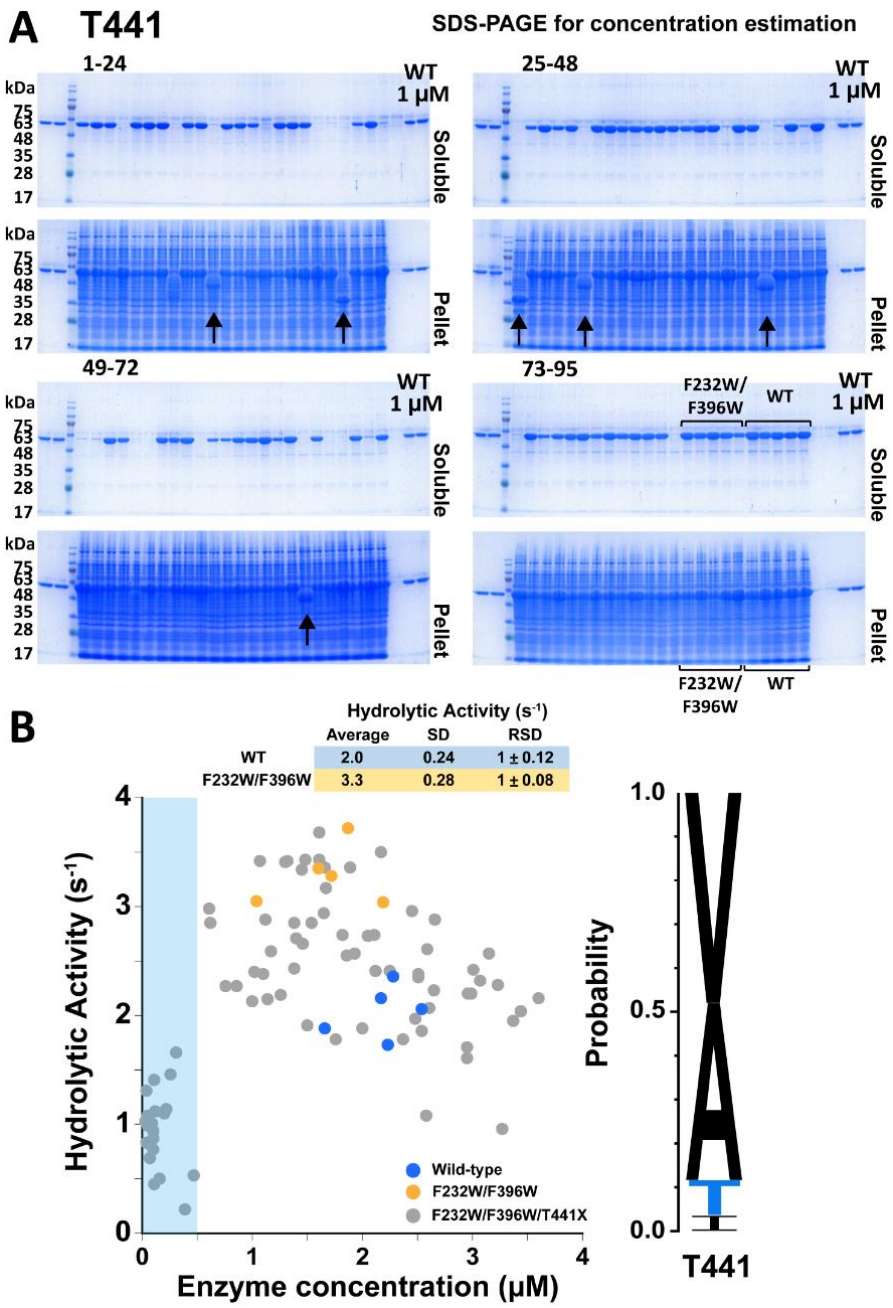

Figure 27. Screening result of T441 site.
(A) SDS-PAGE of purified protein (top, soluble) and cell pellet (bottom, pellet). The concentrations of the purified enzyme were estimated form the band intensity by comparing with that of the wild-type (WT) purified separately. The arrows indicate the truncated mutants in which the stop codons were incorporated. The stop codon ratio was 7.1% and higher than the expected one (2.1%). (B) Hydrolytic activity against purified enzyme concentration for each sample. Blue, orange, and gray dots represent the WT, F232W/F396W, and F232W/F396W/T441X mutants, respectively. Crystalline chitin concentration was 0.5 mg/mL. Note that the enzyme concentration estimation is deemed unreliable at a concentration below 0.5 μM (region indicated by light blue box), and samples located in this region were excluded from further analysis.

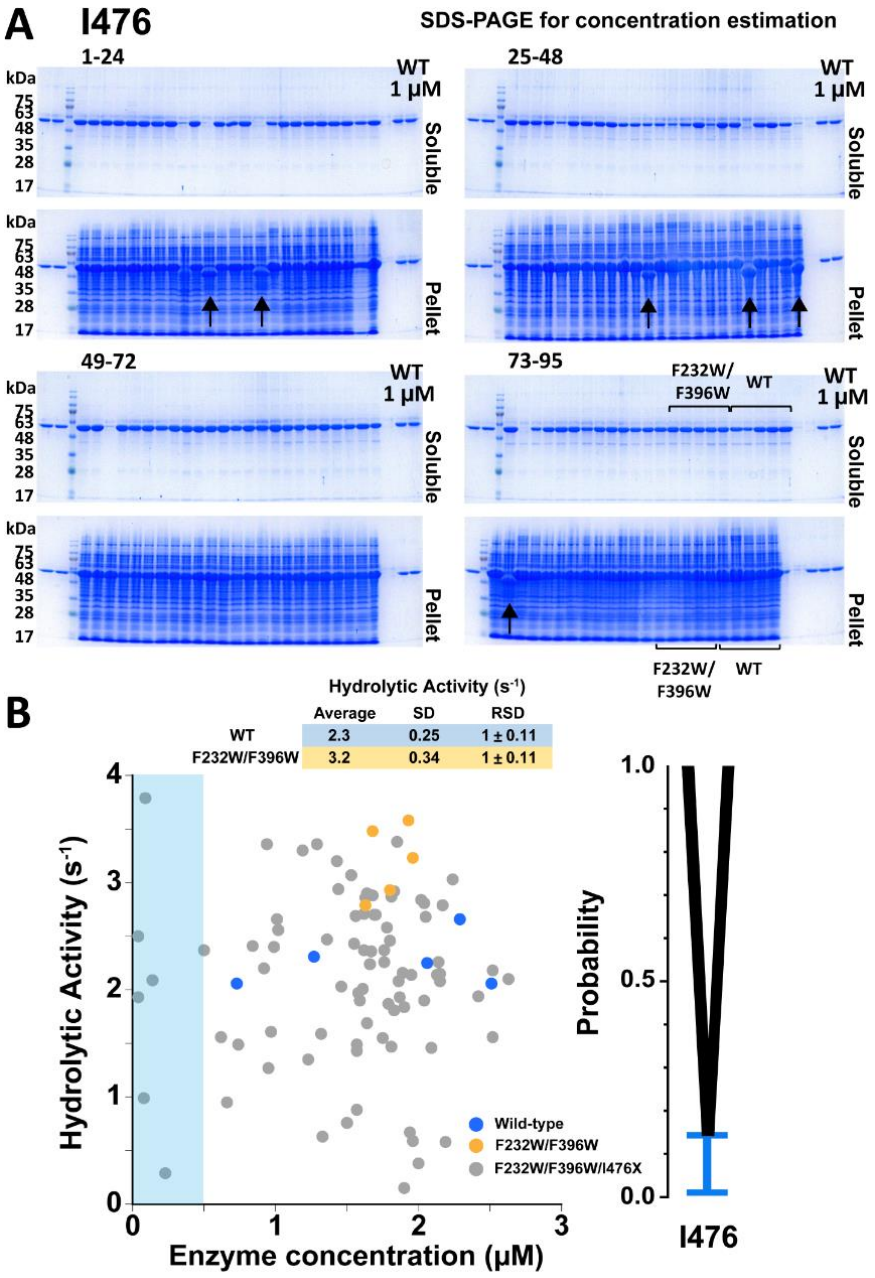

Figure 28. Screening result of I476 site.
(A) SDS-PAGE of purified protein (top, soluble) and cell pellet (bottom, pellet). The concentrations of the purified enzyme were estimated form the band intensity by comparing with that of the wild-type (WT) purified separately. The arrows indicate the truncated mutants in which the stop codons were incorporated. The stop codon ratio was 7.1% and higher than the expected one (2.1%). (B) Hydrolytic activity against purified enzyme concentration for each sample. Blue, orange, and gray dots represent the WT, F232W/F396W, and F232W/F396W/I476X mutants, respectively. Crystalline chitin concentration was 0.5 mg/mL. Note that the enzyme concentration estimation is deemed unreliable at a concentration below 0.5 μM (region indicated by light blue box), and samples located in this region were excluded from further analysis.

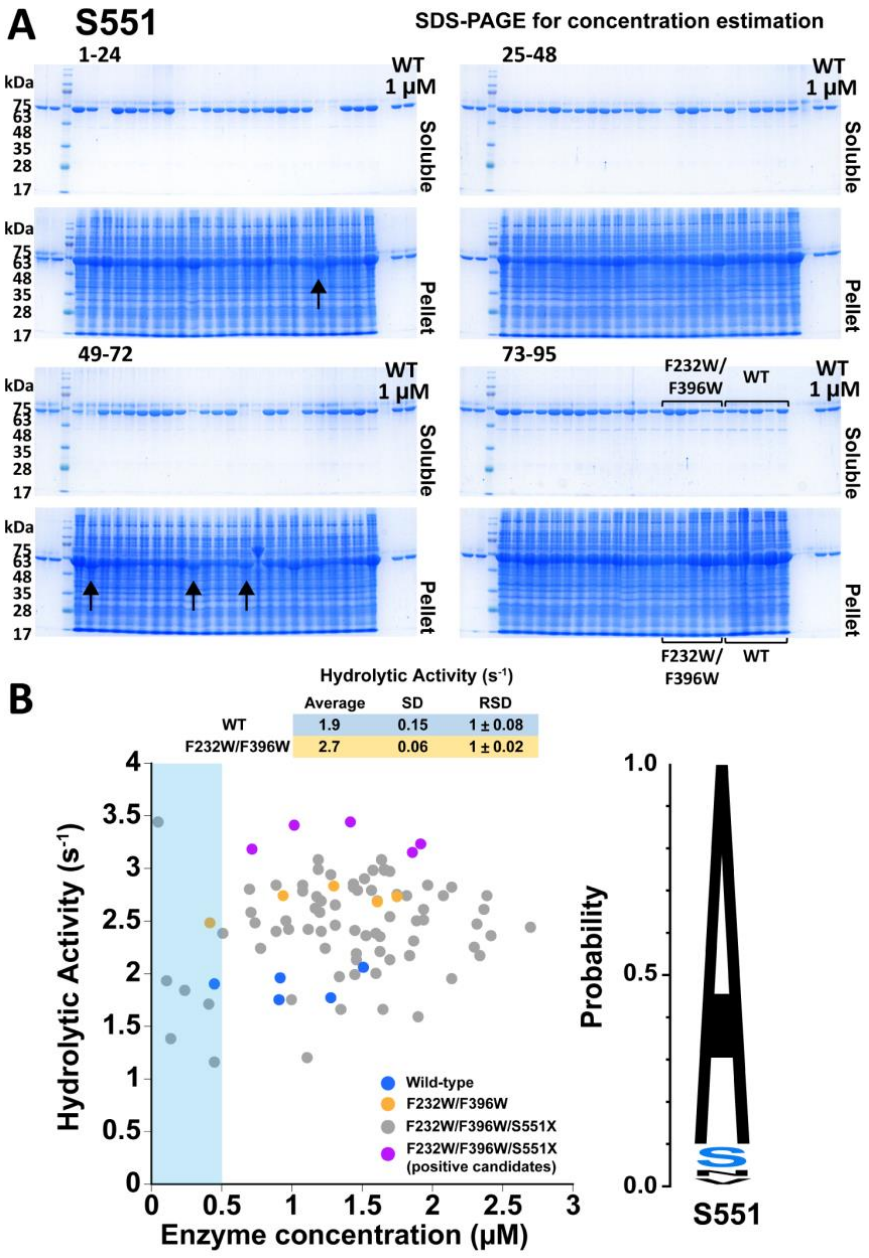

Figure 29. **Screening result of S551 site.**
(A) SDS-PAGE of purified protein (top, soluble) and cell pellet (bottom, pellet). The concentrations of the purified enzyme were estimated form the band intensity by comparing with that of the wild-type (WT) purified separately. The arrows indicate the truncated mutants in which the stop codons were incorporated. The stop codon ratio was 5.9% and higher than the expected ratio (2.1%). (B) Hydrolytic activity against purified enzyme concentration for each sample. Blue and orange dots represent the WT and F232W/F396W, respectively. Gray and purple dots represent F232W/F396W/S551X mutants and their high activity candidates, respectively. Crystalline chitin concentration was 0.5 mg/mL. Note that the enzyme concentration estimation is deemed unreliable at a concentration below 0.5 μM (region indicated by light blue box), and samples located in this region were excluded from further analysis.

After the SDS-PAGE, I estimated the protein concentration by comparing the band intensity with that of the wild-type purified separately from the large-scale culture of *E. coli*. Then, the protein concentration of each sample was adjusted to measure hydrolytic activity quantitatively. For measurement, 0.5 mg/mL crystalline chitin was used as a substrate. Among the eight positions I tried, I identified candidates of high-catalytic activity mutants for three, Ser162, Ser538, and Ser551 (Figure 22, 24, and 29, purple dots). After the determination of the amino acid sequence of the mutants, I repeated the experiments with twelve replications (12 colonies) of each candidate to confirm their hydrolytic activities (Figure 30 and 31).

For Ser538 site, I confirmed that additional S538V mutation actually results in higher hydrolytic activity than the F232W/F396W, whereas other candidates, S538A, S538G, and S538T showed lower activity (Figure 30). Interestingly, although alanine is a predominant amino acid at this position, S538A mutant did not improve the activity. More importantly, valine was not found in the multiple sequence alignment at this position. These results indicate that our method enables me to generate non-natural high activity enzymes, which cannot be identified only by the introduction of predominant amino acid in the multiple sequence alignment. For both the Ser162 and Ser551 sites, I found that the highest activity mutants (S162A and S551A) just show comparable hydrolytic activity with the F232W/F396W (Figure 31). For these positions, the best mutants were both alanine, a predominant amino acid in the multiple sequence alignment.

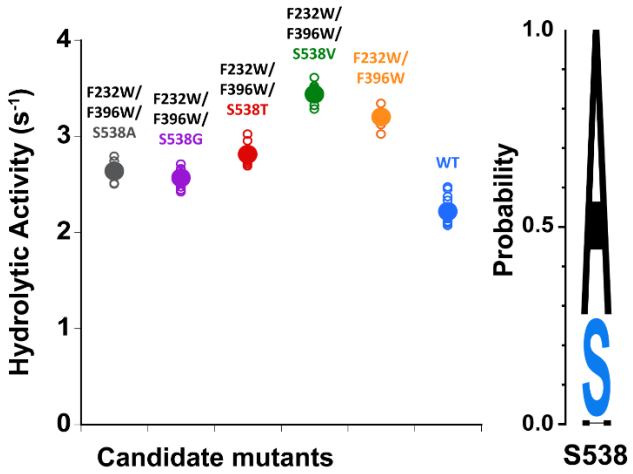

Figure 30. Re-examination of hydrolytic activity of F232W/F396W/S538X mutants.
After amino acid sequence determination, each candidate mutant was cultured again on agar plate and 12 colonies for each mutant were used to confirm their hydrolytic activities. The open circles represent the individual values for each colony, and the filled circles represent the average values. The F232W/F396W/S538V mutant (green) showed higher hydrolytic activity than the F232W/F396W. Crystalline chitin concentration was 0.5 mg/mL.

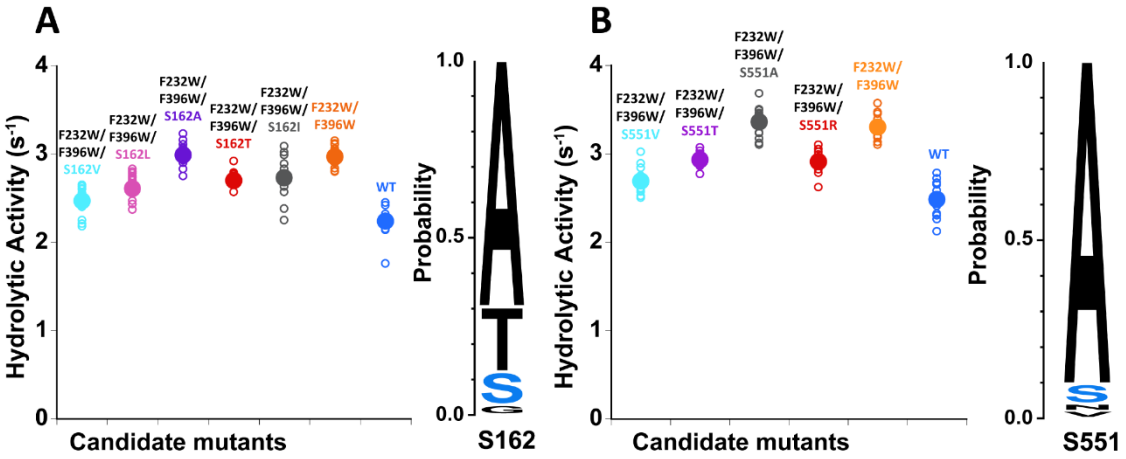

Figure 31. Re-examination of hydrolytic activity of F232W/F396W/S162X and F232W/F396W/S551X mutants.
After amino acid sequence determination, each candidate mutant was cultured again on an agar plate and 12 colonies for each mutant were used to confirm their hydrolytic activities. The open circles represent the individual values for each colony, and the filled circles represent the average values. At the S162 and S551 sites, F232W/F396W/S162A (purple) and F232W/F396W/S551A (gray) showed the highest but comparable hydrolytic activities to the F232W/F396W. Crystalline chitin concentration was 0.5 mg/mL.

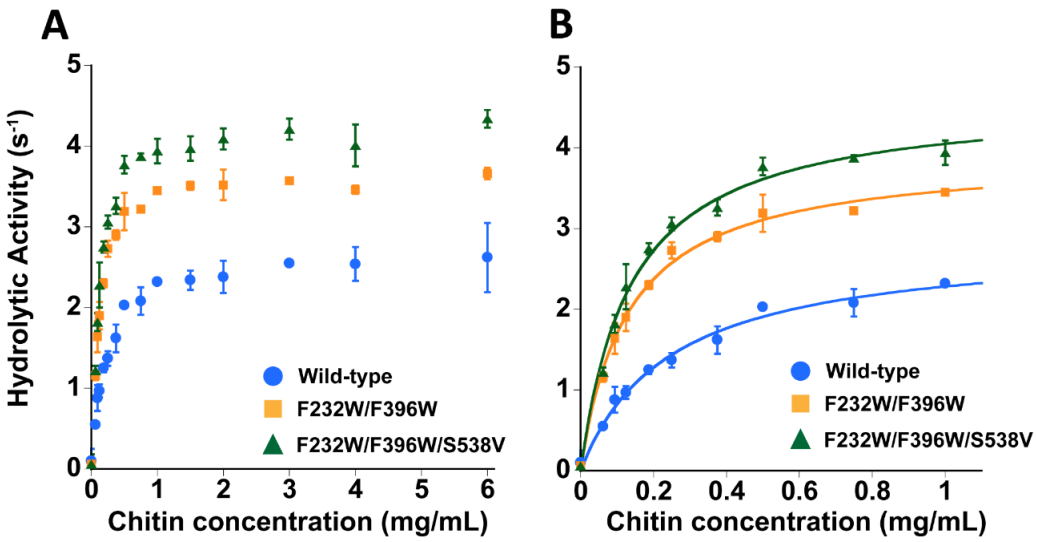

Figure 32. Crystalline chitin concentration dependence of hydrolytic activity of *Sm*ChiA. Hydrolytic activities of the F232W/F396W/S538V (green) were compared with those of the F232W/F396W (orange) and the wild-type (blue) at various crystalline chitin concentrations. (A) 0-6 mg/mL. (B) 0-1 mg/mL. The data points are fitted with the Michaelis-Menten equation to estimate the values of k_{cat} and K_m (shown in Table 10). Error bars represent the standard deviations of the triplicate measurements.

Table 10. Turnover number (k_{cat}) and Michaelis constant (K_m) estimated by biochemical activity measurement.

	k_{cat} (s^{-1})[1]	K_m (mg/mL)[1]	k_{cat}/K_m ($mL mg^{-1} s^{-1}$)
F232W/F396W/S538V	4.6	0.14	33
F232W/F396W	3.9	0.13	30
Wild-type	2.8	0.24	12

[1] k_{cat} and K_m values were determined by the fitting with the Michaelis-Menten equation at 0-1 mg/mL chitin concentration range.

Next, I measured the hydrolytic activities of the F232W/F396W/S538V at various crystalline chitin concentrations (0-6 mg/mL) and compared with those of the WT and F232W/F396W (Figure 32). The F232W/F396W/S538V showed higher hydrolytic activities than the F232W/F396W and WT at all chitin concentrations tried. The k_{cat} and the Michaelis constant (K_m) were estimated by the fitting of the data points at 0-1 mg/mL chitin concentration range with the Michaelis-Menten equation (Figure 32B and Table 10). The k_{cat} and K_m values for the F232W/F396W and WT were almost the same as those identified in Chapter 2[91] (Figure 7 and Table 1). The k_{cat} value for the F232W/F396W/S538V was 4.6 s^{-1}, and 1.2- and 1.6-times higher than those for the F232W/F396W (3.9 s^{-1}) and the WT (2.8 s^{-1}), respectively. The K_m value for the F232W/F396W/S538V was 0.14 mg/mL, and comparable to that for the F232W/F396W (0.13 mg/mL) and 1.7-times lower than that for the WT (0.24 mg/mL). These K_m values indicated that F232W/F396W/S538V could not affect the binding affinity from F232W/F396W mutant.

The Ser538 of the *Sm*ChiA is located next to Trp539, an aromatic residue inside the catalytic cleft important for substrate binding, and also near Asp313 and Glu315, the catalytic residues (Figure 19). Moreover, the Ser538 is also included in the one of the highly conserved motif among Glycoside hydrolase (GH)-18 family (GXXXWXXDXDD)[95], even Ser538 is not highly conserved residue in the motif. Since serine was mutated to valine in S538V, the number of surrounding hydrogen bonds could be reduced due to the removal of the hydroxyl group from the side chain. On the other hand, hydrophobicity could be increased through the introduction of two methyl groups, although the side chain of Ser538 is not facing to the substrate. Therefore, the S538V mutation can affect both the rate constants of processive catalysis and dissociation[91]. In addition, from our previously purposed model[91], the F232W/F396W/S538V mutation could affect both processive catalysis and productive dissociation, in which F232W/F396 affected productive

dissociation rate constant as described in our recent study and S538V could affect processive catalysis rate constant as this mutant affect only k_{cat} but not for K_m[91].

By using single-molecule imaging analysis in Chapter 2, I have revealed that the F232W/F396W shows higher k_{cat} than the WT because of lower dissociation rate constant of productively-bound enzyme and higher processivity than the WT[91]. In this Chapter, I found that the F232W/F396W/S538V shows higher k_{cat} than the F232W/F396W. To understand the mechanism of the F232W/F396W/S538V, the detailed single-molecule analysis will be required. Structural analysis with X-ray crystallography will be also helpful to understand the mechanism at the atomic level.

In summary, as demonstrated in this Chapter, my combination method allows the identification of a high-catalytic activity mutant of an enzyme within a few trial residues. My method will be applicable to other enzymes, although several points could be further improved. For instance, in the current procedure, I used the BugBuster reagent for cell disruption. However, a recent report showed that the BugBuster reagent can cause a high level of contamination of other proteins and decrease the thermostability of the cell extract solutions[96]. In that study, hypotonic extraction is suggested to be used instead of the BugBuster or other detergent containing chemical lysis reagents. In the near future, my group would like to apply further improved combination approach to engineer other enzymes such as the plastic-degrading emzyme, poly(ethylene tetraphthalate)-digestive enzyme or PETase[97], which directly decomposes recalcitrant solid polymer substrates.

Chapter 5

General Conclusion and Discussion

A previous study[55] reported that the catalytic activity of *Serratia mercescens* chitinase A (*Sm*ChiA) against crystalline chitin is improved by the mutation of two phenylalanine residues into tryptophan (F232W/F396W mutant), which are located at the entrance and exit of the substrate binding cleft of the catalytic domain. First I confirmed the hydrolytic activity of F232W/F396W mutant and WT. The k_{cat} value for F232W/ F396W (3.9 s^{-1}) was higher than that for WT (3.1 s^{-1}) (Table 1). The K_m value for F232W/F396W (0.19 mg/mL) was lower than for WT (0.32 mg/mL). Moreover, I performed single-molecule imaging analysis with fluorescence microscopy and high-speed atomic force microscopy to understand the mechanism of high catalytic activity of the F232W/F396W mutant. As a result, I found that high catalytic activity is caused by its high processivity (30 and 52 for WT and F232W/F396W, respectively (Figure 9 and Table 2)) and low productive dissociation rate constant (1.4 ± 0.26 and 0.82 ± 0.089 s^{-1} for WT and F232W/F396W, respectively (Figure 9 and Table 2)). I also proposed a reaction scheme in which processive catalysis is included, and determined all kinetic parameters experimentally. The turnover numbers for both wild-type and F232W/F396W mutant calculated from these kinetic parameters (2.9 and 4.1 s^{-1} for WT and F232W/F396W, respectively (Table 2)) showed excellent agreement with those determined by the biochemical analysis (3.1 and 3.9 s^{-1} for WT and F232W/F396W, respectively (Table 1)), indicating the validity of my reaction scheme. Furthermore, the alignment of amino acid sequences of 258 *Sm*ChiA-like proteins revealed that tryptophan is dominant at the corresponding positions (F232 and F396 for *Sm*ChiA).

In Chapter 3, in order to optimize the degenerate oligonucleotides for site-saturation mutagenesis, the loss-of-function mutant of green fluorescence protein, GFPMut3-Y66H, was used for introducing NNN or NNB codon. Although the ratios of gain-of-function mutant (H66Y) in both colony counting and deep sequencing analysis were similar, I found that the

ratios of nucleotides in the primers were highly biased among the suppliers. Basically, the PCR step does not cause bias, at least when pEDA5-GFPmut3-Y66H is used as a template. Biases for NNB were less severe than for NNN. The supplier which showed the least-bias for NNB primer was used in Chapter 4.

The alignment in Chapter 2 and 4 also showed that several amino acid residues in the catalytic domain are not conserved in *Sm*ChiA. This strongly suggests that although *Sm*ChiA is the most studied processive chitinase, the amino acid sequence is not optimized for high hydrolytic activity. In Chapter 4, I combined bioinformatics, site-saturation mutagenesis, and robot-based automated screening to further improve chitin hydrolytic activity of F232W/F396W mutant. This method allows us to reduce the number of mutation trials and shortens the screening time. As a result, I identified F232W/F396W/S538V mutant which shows further improved hydrolytic activity (k_{cat} = 4.6, 3.9, and 2.8 s^{-1}, for F232W/F396W/S538V, F232W/F396W, and WT, respectively (Figure 32 and Table 10)), just by trying 8 different positions. Interestingly, valine was not found in the multiple sequence alignment at the Ser538 site. This result indicates that my method can generate an active mutant that cannot be achieved only by the introduction of mutation which is predominant in the multiple sequence alignment.

My results highlight the importance of the combination of single-molecule analysis with biochemical analysis to understand the mechanism of *Sm*ChiA. Although I successfully identified F232W/F396W/S538V which shows high catalytic activity, the single-molecule fluorescence analysis and HS-AFM will be required in the future to understand its mechanism. In addition, the experiment of single-molecule analysis with gold-nanoparticle (AuNP) which is high-precision and high-temporal resolution also will be required to understand the mechanism of elementary steps within the processive catlysis process such as decrystallisation,

substrate assisted catalysis and product release for both F232W/F396W and F232W/F396W/S538V mutants (Figure 33). Not only the functional analysis with single-molecule analysis, structural analysis such as x-ray crystallography also will be required to completely understand this high catalytic activity of *Sm*ChiA mutant. This thesis will be helpful for understanding the kinetic mechanisms and further improvement of the crystalline chitin hydrolytic activity of *Sm*ChiA mutants. Both the single-molecule analysis and protein engineering method developed here will be also applicable to other enzymes especially the processive enzymes such as celluase[98] or the non-processive enzymes such as plastic-degrading emzyme, poly(ethylene tetraphthalate)-digestive enzyme or PETase[97] (Figure 34).

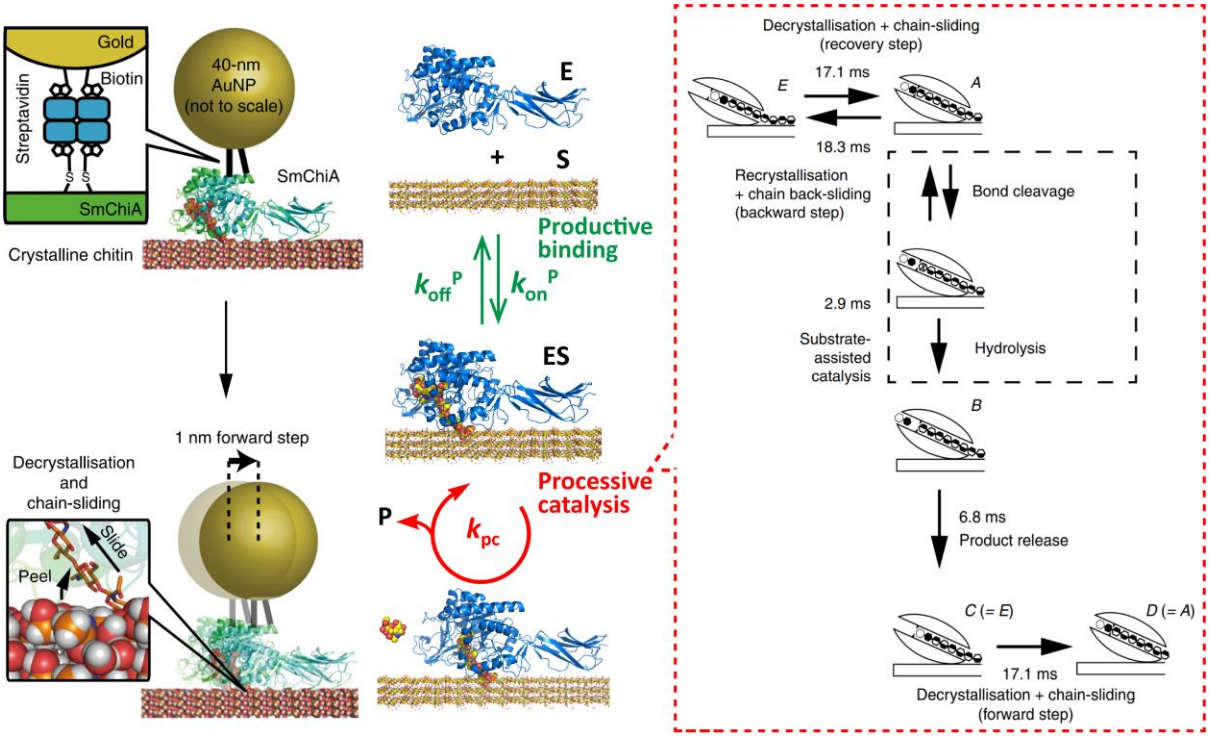

Figure 33. Schematic model of single-molecule analysis by AuNP for studying the elementary steps within processive catalysis of *Sm*ChiA. (modified from Akihiko Nakamura, et al., *Nat. Commun.* 2018 and Akasit Visootsat, et al., *J Biol Chem* 2020)[17, 91]

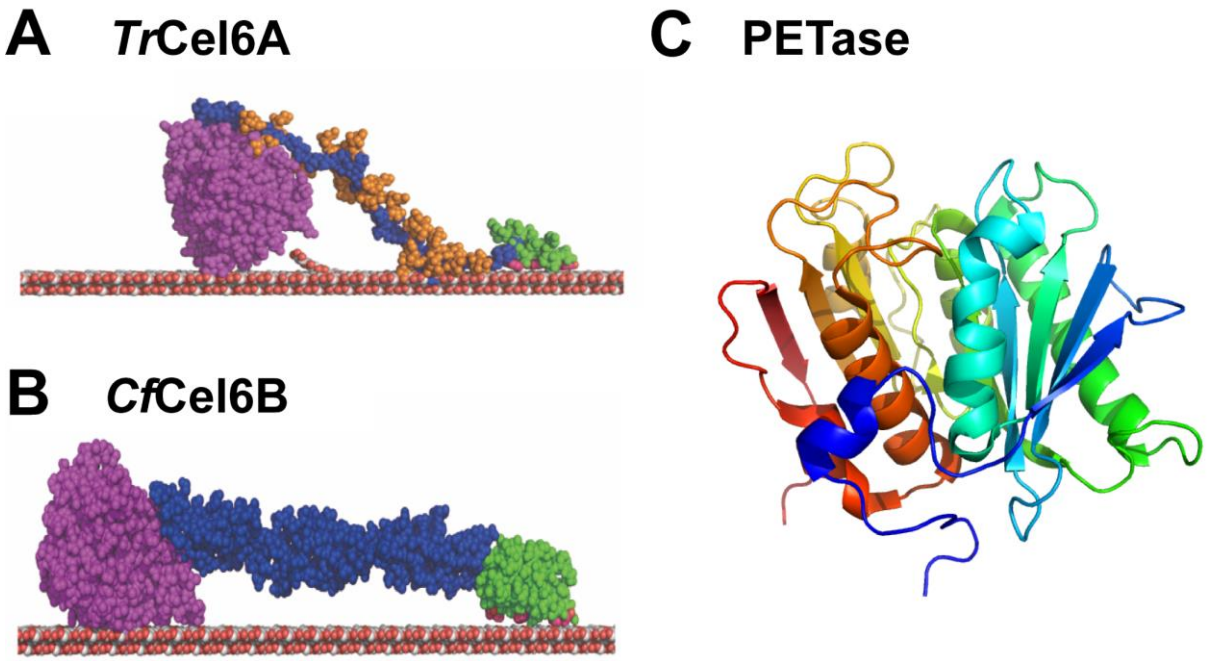

Figure 34. Schematic structures of applicable enzymes for developed methods such as (A) *Trichoderma reesei* cellulase (*Tr*Cel6A, model structure)[53], (B) *Cellulomonas fimi* cellulase (*Cf*Cel6B, model structure)[99] and (C) Poly(ethylene tetraphthalate)-digestive enzyme (plastic-degrading enzyme, PETase, PDB ID: 6EQE)[100]. For *Cf*Cel6B, the structure of CD is the x-ray crystal structure (PDB ID: 7CBD, and linker and cellulose binding domain are modeled by Swiss-model. Both *Tr*Cel6A and *Cf*Cel6B are shown in sphere model. The catalytic domain, linker and cellulose binding domain are represented by pink, blue and green spheres, respectively. The orange spheres in *Tr*Cel6A represent the estimated glycosylation modification on the linker. For PETase, the crystal structure is shown in the ribbon model.

Appendix

Purification of crystalline chitin from tubeworms (*Lamellibrachia Satsuma*)

The purification of crystalline chitin from *L. Satsuma* tube worms was followed the previous study[31].

*Tubes of the tubeworms have to be wet and keep in 4 °C in MilliQ

1. Take about 85 g wet weight of the tube and soak in the MilliQ

2. Cut the tube into about 3 cm pieces and cut along the long axis into half as shown in Figure 32

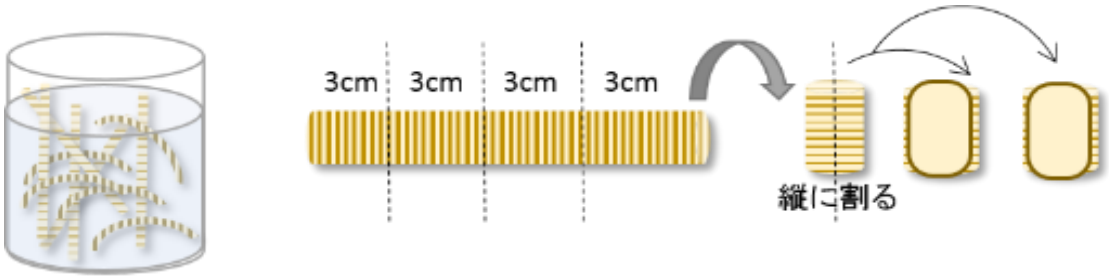

Figure 35. Schematic image of *L. Satsuma* tube worms. The dotted lines indicate the cutting lines.

3. Measure the 80 g of tube pieces, soak in 1 L of 1 M NaOH, and incubate at room temperature (~25 °C) overnight (~16 hours)

4. Wash the tubes with clean water until the pH of the wastewater become 7 (measure with Litmus paper)

5. Rinse with MilliQ for 3 times

6. Soak the tubes in 1 L of 0.1M NaAC (pH4.9) with 0.3% $NaClO_2$ and incubate 70 °C for 3 hours

7. Wash the tube with clean water until the pH of the wastewater become 7 (measure with Litmus paper) and Rinse with MilliQ for 3 times

8. Squeeze the tube to remove the excess water and soak the tube in 1 L of 0.1M HCl, then incubate at 80 °C for 20 min

9. Wash the tube with clean water until the pH of the wastewater become 7 (measure with Litmus paper) and Rinse with MilliQ for 3 times

10. Transfer one-tenth of acid-treated tubes to 300 mL MilliQ in 500 mL round bottom flask

11. Homogenize with Physcotron homogenizer at 10,000 rpm until the suspension become homogeneous (if the homogenizer blade get stuck, remove the aggregation tube and loosen with hand or scissors)

12. Repeat homogenization until finish all of the tubes

13. Centrifuge the suspension at 8,000 g for 20 min at 4 °C and discard the supernatant

14. Store the precipitated chitin fibers at 4 °C with tight sealing to prevent drying

15. Measure 30 g of the chitin fibers (wet weight) and transfer to the round bottom flask

16. Add 120 mL of 6 N HCl and 30 mL MilliQ

17. Cover the connector of the stir bar with parafilm and insert stirrer bar to the round bottom flask as shown in Figure 33.

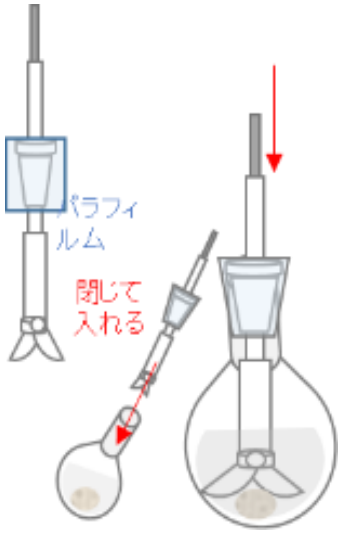

Figure 36. Schematic image how to set up the stir bar with round bottom flask.

18. Incubate 80 °C for 7 hours with stir mix at 300 rpm

19. Add 200 mL of MilliQ into the round bottom flask and incubate at room temperature (~25 °C) overnight

20. Centrifuge the chitin suspension at 10,000 g for 10 min at 4 °C then discard the supernatant and re-suspend the precipitant with 200 mL MilliQ

20. Add 300 mL of MilliQ and centrifuge at 10,000 g for 15 min at 4 °C

21. Discard the supernatant and re-suspend the precipitant with 200 mL MilliQ

22. Add 300 mL of MilliQ and centrifuge at 15,000 g for 30 min at 4 °C

23. Discard the supernatant and re-suspend the precipitant with 200 mL MilliQ

24. Add 300 mL of MilliQ and centrifuge at 15,000 g for 30 min at 4 °C
25. Discard the supernatant and re-suspend the precipitant with 200 mL MilliQ
26. Add 300 mL of MilliQ and centrifuge at 15,000 g for 30 min at 4 °C
(If the supernatant is not clear, increase the speed or time of centrifugation because chitin becomes more disperse when pH becomes neutral)
27. Discard the supernatant and check the pH of the supernatant, it should be neutral
28. Re-suspend the precipitant in 100 mL of MilliQ and divide into two 50 mL tubes
29. Centrifuge at 3,000 g for 5 min at 4 °C then collect the supernatant in a glass bottle
30. Discard the precipitant and wash the tubes with MilliQ
31. Transfer the supernatant in glass bottle back to tubes
32. Repeat centrifugation (Step 29 – 31) three times
33. Centrifuge at 6,000 g for 5 min at 4 °C then collect the supernatant in a glass bottle
34. Discard the precipitant and wash the tubes with MilliQ
35. Repeat centrifugation (Step 29 – 31) three times
36. Store the chitin suspension in an aluminum foil-covered glass bottle at 4 °C until use
37. Wash the glass container for measuring the weight with MilliQ and completely dry in the 70 °C oven
38. Measure the weight of the dried glass container
39. Add 10 mL of chitin suspension into the glass container and completely dry in the 70 °C oven (about 12-16 hours)
40. Measure the weight of dry chitin and calculate the concentration

References

1. Merzendorfer, H.; Zimoch, L., Chitin metabolism in insects: structure, function and regulation of chitin synthases and chitinases. *J Exp Biol* **2003,** *206* (Pt 24), 4393-412.
2. Hamed, I.; Özogul, F.; Regenstein, J. M., Industrial applications of crustacean by-products (chitin, chitosan, and chitooligosaccharides): A review. *Trends in Food Science & Technology* **2016,** *48*, 40-50.
3. Langner, T.; Gohre, V., Fungal chitinases: function, regulation, and potential roles in plant/pathogen interactions. *Curr Genet* **2016,** *62* (2), 243-54.
4. Beier, S.; Bertilsson, S., Bacterial chitin degradation-mechanisms and ecophysiological strategies. *Front Microbiol* **2013,** *4*, 149.
5. Moussian, B., Chitin: Structure, Chemistry and Biology. *Adv Exp Med Biol* **2019,** *1142*, 5-18.
6. Khor, E.; Lim, L. Y., Implantable applications of chitin and chitosan. *Biomaterials* **2003,** *24* (13), 2339-49.
7. Yan, N.; Chen, X., Sustainability: Don't waste seafood waste. *Nature* **2015,** *524* (7564), 155-7.
8. Songsiriritthigul, C.; Pantoom, S.; Aguda, A. H.; Robinson, R. C.; Suginta, W., Crystal structures of Vibrio harveyi chitinase A complexed with chitooligosaccharides: implications for the catalytic mechanism. *J Struct Biol* **2008,** *162* (3), 491-9.
9. Deguchi, S.; Tsujii, K.; Horikoshi, K., In situ microscopic observation of chitin and fungal cells with chitinous cell walls in hydrothermal conditions. *Sci Rep* **2015,** *5*, 11907.
10. Einbu, A.; Varum, K. M., Characterization of chitin and its hydrolysis to GlcNAc and GlcN. *Biomacromolecules* **2008,** *9* (7), 1870-5.

11. Rathore, A. S.; Gupta, R. D., Chitinases from Bacteria to Human: Properties, Applications, and Future Perspectives. *Enzyme Res* **2015,** *2015*, 791907.

12. Perrakis, A.; Tews, I.; Dauter, Z.; Oppenheim, A. B.; Chet, I.; Wilson, K. S.; Vorgias, C. E., Crystal structure of a bacterial chitinase at 2.3 A resolution. *Structure* **1994,** *2* (12), 1169-80.

13. Lombard, V.; Golaconda Ramulu, H.; Drula, E.; Coutinho, P. M.; Henrissat, B., The carbohydrate-active enzymes database (CAZy) in 2013. *Nucleic Acids Res* **2014,** *42* (Database issue), D490-5.

14. Toratani, T.; Shoji, T.; Ikehara, T.; Suzuki, K.; Watanabe, T., The importance of chitobiase and N-acetylglucosamine (GlcNAc) uptake in N,N'-diacetylchitobiose [(GlcNAc)2] utilization by Serratia marcescens 2,170. *Microbiology* **2008,** *154* (Pt 5), 1326-1332.

15. Oyeleye, A.; Normi, Y. M., Chitinase: diversity, limitations, and trends in engineering for suitable applications. *Biosci Rep* **2018,** *38* (4).

16. Itoh, T.; Kimoto, H., Bacterial Chitinase System as a Model of Chitin Biodegradation. *Adv Exp Med Biol* **2019,** *1142*, 131-151.

17. Nakamura, A.; Okazaki, K. I.; Furuta, T.; Sakurai, M.; Iino, R., Processive chitinase is Brownian monorail operated by fast catalysis after peeling rail from crystalline chitin. *Nat Commun* **2018,** *9* (1), 3814.

18. Vaaje-Kolstad, G.; Horn, S. J.; Sorlie, M.; Eijsink, V. G., The chitinolytic machinery of Serratia marcescens--a model system for enzymatic degradation of recalcitrant polysaccharides. *FEBS J* **2013,** *280* (13), 3028-49.

19. Nakagawa, Y. S.; Eijsink, V. G.; Totani, K.; Vaaje-Kolstad, G., Conversion of alpha-chitin substrates with varying particle size and crystallinity reveals substrate preferences of the chitinases and lytic polysaccharide monooxygenase of Serratia marcescens. *J Agric Food*

Chem **2013,** *61* (46), 11061-6.

20. Mekasha, S.; Byman, I. R.; Lynch, C.; Toupalová, H.; Anděra, L.; Næs, T.; Vaaje-Kolstad, G.; Eijsink, V. G. H., Development of enzyme cocktails for complete saccharification of chitin using mono-component enzymes from Serratia marcescens. *Process Biochemistry* **2017,** *56*, 132-138.
21. Uchiyama, T.; Katouno, F.; Nikaidou, N.; Nonaka, T.; Sugiyama, J.; Watanabe, T., Roles of the exposed aromatic residues in crystalline chitin hydrolysis by chitinase A from Serratia marcescens 2170. *J Biol Chem* **2001,** *276* (44), 41343-9.
22. Zakariassen, H.; Aam, B. B.; Horn, S. J.; Varum, K. M.; Sorlie, M.; Eijsink, V. G., Aromatic residues in the catalytic center of chitinase A from Serratia marcescens affect processivity, enzyme activity, and biomass converting efficiency. *J Biol Chem* **2009,** *284* (16), 10610-7.
23. Uchihashi, T.; Kodera, N.; Ando, T., Guide to video recording of structure dynamics and dynamic processes of proteins by high-speed atomic force microscopy. *Nat Protoc* **2012,** *7* (6), 1193-206.
24. Ando, T., High-speed AFM imaging. *Curr Opin Struct Biol* **2014,** *28*, 63-8.
25. Ando, T.; Uchihashi, T.; Scheuring, S., Filming biomolecular processes by high-speed atomic force microscopy. *Chem Rev* **2014,** *114* (6), 3120-88.
26. Neuman, K. C.; Block, S. M., Optical trapping. *Rev Sci Instrum* **2004,** *75* (9), 2787-809.
27. Joo, C.; Balci, H.; Ishitsuka, Y.; Buranachai, C.; Ha, T., Advances in single-molecule fluorescence methods for molecular biology. *Annu Rev Biochem* **2008,** *77*, 51-76.
28. Kudalkar, E. M.; Davis, T. N.; Asbury, C. L., Single-Molecule Total Internal Reflection Fluorescence Microscopy. *Cold Spring Harb Protoc* **2016,** *2016* (5).
29. Chiu, S. W.; Leake, M. C., Functioning nanomachines seen in real-time in living bacteria

using single-molecule and super-resolution fluorescence imaging. *Int J Mol Sci* **2011,** *12* (4), 2518-42.

30. Igarashi, K.; Uchihashi, T.; Koivula, A.; Wada, M.; Kimura, S.; Penttila, M.; Ando, T.; Samejima, M., Visualization of cellobiohydrolase I from Trichoderma reesei moving on crystalline cellulose using high-speed atomic force microscopy. *Methods Enzymol* **2012,** *510*, 169-82.
31. Igarashi, K.; Uchihashi, T.; Uchiyama, T.; Sugimoto, H.; Wada, M.; Suzuki, K.; Sakuda, S.; Ando, T.; Watanabe, T.; Samejima, M., Two-way traffic of glycoside hydrolase family 18 processive chitinases on crystalline chitin. *Nat Commun* **2014,** *5*, 3975.
32. Bambara, R. A.; Uyemura, D.; Choi, T., On the processive mechanism of Escherichia coli DNA polymerase I. Quantitative assessment of processivity. *J Biol Chem* **1978,** *253* (2), 413-23.
33. Bonderoff, J. M.; Lloyd, R. E., Time-dependent increase in ribosome processivity. *Nucleic Acids Res* **2010,** *38* (20), 7054-67.
34. Rock, R. S.; Ramamurthy, B.; Dunn, A. R.; Beccafico, S.; Rami, B. R.; Morris, C.; Spink, B. J.; Franzini-Armstrong, C.; Spudich, J. A.; Sweeney, H. L., A flexible domain is essential for the large step size and processivity of myosin VI. *Mol Cell* **2005,** *17* (4), 603-9.
35. Shastry, S.; Hancock, W. O., Neck linker length determines the degree of processivity in kinesin-1 and kinesin-2 motors. *Curr Biol* **2010,** *20* (10), 939-43.
36. Schrader, E. K.; Harstad, K. G.; Matouschek, A., Targeting proteins for degradation. *Nat Chem Biol* **2009,** *5* (11), 815-22.
37. Snoberger, A.; Anderson, R. T.; Smith, D. M., The Proteasomal ATPases Use a Slow but Highly Processive Strategy to Unfold Proteins. *Front Mol Biosci* **2017,** *4*, 18.

38. Rouvinen, J.; Bergfors, T.; Teeri, T.; Knowles, J. K.; Jones, T. A., Three-dimensional structure of cellobiohydrolase II from Trichoderma reesei. *Science* **1990,** *249* (4967), 380-6.

39. Henrissat, B.; Davies, G., Structural and sequence-based classification of glycoside hydrolases. *Curr Opin Struct Biol* **1997,** *7* (5), 637-44.

40. Sørlie, M.; Zakariassen, H.; Norberg, A. L.; Eijsink, V. G. H., Processivity and substrate-binding in family 18 chitinases. *Biocatalysis and Biotransformation* **2012,** *30* (3), 353-365.

41. Von Hippel, P. H.; Fairfield, F. R.; Dolejsi, M. K., On the processivity of polymerases. *Ann N Y Acad Sci* **1994,** *726*, 118-31.

42. Breyer, W. A.; Matthews, B. W., A structural basis for processivity. *Protein Sci* **2001,** *10* (9), 1699-711.

43. Beckham, G. T.; Crowley, M. F., Examination of the alpha-chitin structure and decrystallization thermodynamics at the nanoscale. *J Phys Chem B* **2011,** *115* (15), 4516-22.

44. Divne, C.; Stahlberg, J.; Teeri, T. T.; Jones, T. A., High-resolution crystal structures reveal how a cellulose chain is bound in the 50 A long tunnel of cellobiohydrolase I from Trichoderma reesei. *J Mol Biol* **1998,** *275* (2), 309-25.

45. A., Q. F., Protein-carbohydrate interactions : basic molecular features. *Pure & Appl. Chem* **1989,** *61* (7), 1293-1306.

46. Meyer, J. E.; Schulz, G. E., Energy profile of maltooligosaccharide permeation through maltoporin as derived from the structure and from a statistical analysis of saccharide-protein interactions. *Protein Sci* **1997,** *6* (5), 1084-91.

47. Williams, S. J.; Davies, G. J., Protein--carbohydrate interactions: learning lessons from nature. *Trends Biotechnol* **2001,** *19* (9), 356-62.

48. Hu, G.; Oguro, A.; Li, C.; Gershon, P. D.; Quiocho, F. A., The "cap-binding slot" of an mRNA cap-binding protein: quantitative effects of aromatic side chain choice in the double-stacking sandwich with cap. *Biochemistry* **2002,** *41* (24), 7677-87.

49. Kurasin, M.; Valjamae, P., Processivity of cellobiohydrolases is limited by the substrate. *J Biol Chem* **2011,** *286* (1), 169-77.

50. Jalak, J.; Kurasin, M.; Teugjas, H.; Valjamae, P., Endo-exo synergism in cellulose hydrolysis revisited. *J Biol Chem* **2012,** *287* (34), 28802-15.

51. Kurasin, M.; Kuusk, S.; Kuusk, P.; Sorlie, M.; Valjamae, P., Slow Off-rates and Strong Product Binding Are Required for Processivity and Efficient Degradation of Recalcitrant Chitin by Family 18 Chitinases. *J Biol Chem* **2015,** *290* (48), 29074-85.

52. Cruys-Bagger, N.; Tatsumi, H.; Ren, G. R.; Borch, K.; Westh, P., Transient kinetics and rate-limiting steps for the processive cellobiohydrolase Cel7A: effects of substrate structure and carbohydrate binding domain. *Biochemistry* **2013,** *52* (49), 8938-48.

53. Nakamura, A.; Tasaki, T.; Ishiwata, D.; Yamamoto, M.; Okuni, Y.; Visootsat, A.; Maximilien, M.; Noji, H.; Uchiyama, T.; Samejima, M.; Igarashi, K.; Iino, R., Single-molecule Imaging Analysis of Binding, Processive Movement, and Dissociation of Cellobiohydrolase Trichoderma reesei Cel6A and Its Domains on Crystalline Cellulose. *J Biol Chem* **2016,** *291* (43), 22404-22413.

54. Nakamura, A.; Tasaki, T.; Okuni, Y.; Song, C.; Murata, K.; Kozai, T.; Hara, M.; Sugimoto, H.; Suzuki, K.; Watanabe, T.; Uchihashi, T.; Noji, H.; Iino, R., Rate constants, processivity, and productive binding ratio of chitinase A revealed by single-molecule analysis. *Phys Chem Chem Phys* **2018,** *20* (5), 3010-3018.

55. Liu, T.; Chen, L.; Zhou, Y.; Jiang, X.; Duan, Y.; Yang, Q., Structure, Catalysis, and Inhibition of OfChi-h, the Lepidoptera-exclusive Insect Chitinase. *J Biol Chem* **2017,** *292*

(6), 2080-2088.

56. Papanikolau, Y.; Prag, G.; Tavlas, G.; Vorgias, C. E.; Oppenheim, A. B.; Petratos, K., High resolution structural analyses of mutant chitinase A complexes with substrates provide new insight into the mechanism of catalysis. *Biochemistry* **2001,** *40* (38), 11338-43.

57. Nielsen, H., Predicting Secretory Proteins with SignalP. *Methods Mol Biol* **2017,** *1611*, 59-73.

58. Li, W.; Cowley, A.; Uludag, M.; Gur, T.; McWilliam, H.; Squizzato, S.; Park, Y. M.; Buso, N.; Lopez, R., The EMBL-EBI bioinformatics web and programmatic tools framework. *Nucleic Acids Res* **2015,** *43* (W1), W580-4.

59. Crooks, G. E.; Hon, G.; Chandonia, J. M.; Brenner, S. E., WebLogo: a sequence logo generator. *Genome Res* **2004,** *14* (6), 1188-90.

60. Kawai, F.; Nakamura, A.; Visootsat, A.; Iino, R., Plasmid-Based One-Pot Saturation Mutagenesis and Robot-Based Automated Screening for Protein Engineering. *ACS Omega* **2018,** *3* (7), 7715-7726.

61. Hudson, K. L.; Bartlett, G. J.; Diehl, R. C.; Agirre, J.; Gallagher, T.; Kiessling, L. L.; Woolfson, D. N., Carbohydrate-Aromatic Interactions in Proteins. *J Am Chem Soc* **2015,** *137* (48), 15152-60.

62. Pantoom, S.; Songsiriritthigul, C.; Suginta, W., The effects of the surface-exposed residues on the binding and hydrolytic activities of Vibrio carchariae chitinase A. *BMC Biochem* **2008,** *9*, 2.

63. Jana, S.; Hamre, A. G.; Wildberger, P.; Holen, M. M.; Eijsink, V. G.; Beckham, G. T.; Sorlie, M.; Payne, C. M., Aromatic-Mediated Carbohydrate Recognition in Processive Serratia marcescens Chitinases. *J Phys Chem B* **2016,** *120* (7), 1236-49.

64. Zakariassen, H.; Hansen, M. C.; Joranli, M.; Eijsink, V. G.; Sorlie, M., Mutational effects

on transglycosylating activity of family 18 chitinases and construction of a hypertransglycosylating mutant. *Biochemistry* **2011,** *50* (25), 5693-703.

65. Madhuprakash, J.; Dalhus, B.; Rani, T. S.; Podile, A. R.; Eijsink, V. G. H.; Sorlie, M., Key Residues Affecting Transglycosylation Activity in Family 18 Chitinases: Insights into Donor and Acceptor Subsites. *Biochemistry* **2018,** *57* (29), 4325-4337.
66. Moran-Mirabal, J. M.; Bolewski, J. C.; Walker, L. P., Reversibility and binding kinetics of Thermobifida fusca cellulases studied through fluorescence recovery after photobleaching microscopy. *Biophys Chem* **2011,** *155* (1), 20-8.
67. Jung, J.; Sethi, A.; Gaiotto, T.; Han, J. J.; Jeoh, T.; Gnanakaran, S.; Goodwin, P. M., Binding and movement of individual Cel7A cellobiohydrolases on crystalline cellulose surfaces revealed by single-molecule fluorescence imaging. *J Biol Chem* **2013,** *288* (33), 24164-72.
68. Luterbacher, J. S.; Walker, L. P.; Moran-Mirabal, J. M., Observing and modeling BMCC degradation by commercial cellulase cocktails with fluorescently labeled Trichoderma reseii Cel7A through confocal microscopy. *Biotechnol Bioeng* **2013,** *110* (1), 108-17.
69. Kari, J.; Olsen, J.; Borch, K.; Cruys-Bagger, N.; Jensen, K.; Westh, P., Kinetics of cellobiohydrolase (Cel7A) variants with lowered substrate affinity. *J Biol Chem* **2014,** *289* (47), 32459-68.
70. Nakamura, A.; Watanabe, H.; Ishida, T.; Uchihashi, T.; Wada, M.; Ando, T.; Igarashi, K.; Samejima, M., Trade-off between processivity and hydrolytic velocity of cellobiohydrolases at the surface of crystalline cellulose. *J Am Chem Soc* **2014,** *136* (12), 4584-92.
71. Shibafuji, Y.; Nakamura, A.; Uchihashi, T.; Sugimoto, N.; Fukuda, S.; Watanabe, H.; Samejima, M.; Ando, T.; Noji, H.; Koivula, A.; Igarashi, K.; Iino, R., Single-molecule imaging analysis of elementary reaction steps of Trichoderma reesei cellobiohydrolase I

(Cel7A) hydrolyzing crystalline cellulose Ialpha and IIII. *J Biol Chem* **2014,** *289* (20), 14056-65.

72. Buettner, K.; Hertel, T. C.; Pietzsch, M., Increased thermostability of microbial transglutaminase by combination of several hot spots evolved by random and saturation mutagenesis. *Amino Acids* **2012,** *42* (2-3), 987-96.

73. Reetz, M. T., Biocatalysis in organic chemistry and biotechnology: past, present, and future. *J Am Chem Soc* **2013,** *135* (34), 12480-96.

74. Zhang, X. F.; Yang, G. Y.; Zhang, Y.; Xie, Y.; Withers, S. G.; Feng, Y., A general and efficient strategy for generating the stable enzymes. *Sci Rep* **2016,** *6*, 33797.

75. Yin, H.; Pijning, T.; Meng, X.; Dijkhuizen, L.; van Leeuwen, S. S., Engineering of the Bacillus circulans beta-Galactosidase Product Specificity. *Biochemistry* **2017,** *56* (5), 704-711.

76. Wu, N. C.; Grande, G.; Turner, H. L.; Ward, A. B.; Xie, J.; Lerner, R. A.; Wilson, I. A., In vitro evolution of an influenza broadly neutralizing antibody is modulated by hemagglutinin receptor specificity. *Nat Commun* **2017,** *8*, 15371.

77. Jiao, L.; Liu, Y.; Zhang, X.; Liu, B.; Zhang, C.; Liu, X., Site-saturation mutagenesis library construction and screening for specific broad-spectrum single-domain antibodies against multiple Cry1 toxins. *Appl Microbiol Biotechnol* **2017,** *101* (15), 6071-6082.

78. Sayous, V.; Lubrano, P.; Li, Y.; Acevedo-Rocha, C. G., Unbiased libraries in protein directed evolution. *Biochim Biophys Acta Proteins Proteom* **2020,** *1868* (2), 140321.

79. Kille, S.; Acevedo-Rocha, C. G.; Parra, L. P.; Zhang, Z. G.; Opperman, D. J.; Reetz, M. T.; Acevedo, J. P., Reducing codon redundancy and screening effort of combinatorial protein libraries created by saturation mutagenesis. *ACS Synth Biol* **2013,** *2* (2), 83-92.

80. Tang, L.; Gao, H.; Zhu, X.; Wang, X.; Zhou, M.; Jiang, R., Construction of "small-

intelligent" focused mutagenesis libraries using well-designed combinatorial degenerate primers. *Biotechniques* **2012,** *52* (3), 149-58.

81. Hughes, M. D.; Nagel, D. A.; Santos, A. F.; Sutherland, A. J.; Hine, A. V., Removing the redundancy from randomised gene libraries. *J Mol Biol* **2003,** *331* (5), 973-9.
82. Zhu, B.; Cai, G.; Hall, E. O.; Freeman, G. J., In-fusion assembly: seamless engineering of multidomain fusion proteins, modular vectors, and mutations. *Biotechniques* **2007,** *43* (3), 354-9.
83. Garcia-Nafria, J.; Watson, J. F.; Greger, I. H., IVA cloning: A single-tube universal cloning system exploiting bacterial In Vivo Assembly. *Sci Rep* **2016,** *6*, 27459.
84. Okegawa, Y.; Motohashi, K., A simple and ultra-low cost homemade seamless ligation cloning extract (SLiCE) as an alternative to a commercially available seamless DNA cloning kit. *Biochem Biophys Rep* **2015,** *4*, 148-151.
85. Okegawa, Y.; Motohashi, K., Evaluation of seamless ligation cloning extract preparation methods from an Escherichia coli laboratory strain. *Anal Biochem* **2015,** *486*, 51-3.
86. Gibson, D. G.; Young, L.; Chuang, R. Y.; Venter, J. C.; Hutchison, C. A., 3rd; Smith, H. O., Enzymatic assembly of DNA molecules up to several hundred kilobases. *Nat Methods* **2009,** *6* (5), 343-5.
87. Gibson, D. G.; Glass, J. I.; Lartigue, C.; Noskov, V. N.; Chuang, R. Y.; Algire, M. A.; Benders, G. A.; Montague, M. G.; Ma, L.; Moodie, M. M.; Merryman, C.; Vashee, S.; Krishnakumar, R.; Assad-Garcia, N.; Andrews-Pfannkoch, C.; Denisova, E. A.; Young, L.; Qi, Z. Q.; Segall-Shapiro, T. H.; Calvey, C. H.; Parmar, P. P.; Hutchison, C. A., 3rd; Smith, H. O.; Venter, J. C., Creation of a bacterial cell controlled by a chemically synthesized genome. *Science* **2010,** *329* (5987), 52-6.
88. Wrenbeck, E. E.; Klesmith, J. R.; Stapleton, J. A.; Adeniran, A.; Tyo, K. E.; Whitehead, T.

A., Plasmid-based one-pot saturation mutagenesis. *Nat Methods* **2016,** *13* (11), 928-930.

89. Firnberg, E.; Ostermeier, M., PFunkel: efficient, expansive, user-defined mutagenesis. *PLoS One* **2012,** *7* (12), e52031.

90. Nov, Y., When second best is good enough: another probabilistic look at saturation mutagenesis. *Appl Environ Microbiol* **2012,** *78* (1), 258-62.

91. Visootsat, A.; Nakamura, A.; Vignon, P.; Watanabe, H.; Uchihashi, T.; Iino, R., Single-molecule imaging analysis reveals the mechanism of a high-catalytic-activity mutant of chitinase A from Serratia marcescens. *J Biol Chem* **2020,** *295* (7), 1915-1925.

92. Goldenzweig, A.; Goldsmith, M.; Hill, S. E.; Gertman, O.; Laurino, P.; Ashani, Y.; Dym, O.; Unger, T.; Albeck, S.; Prilusky, J.; Lieberman, R. L.; Aharoni, A.; Silman, I.; Sussman, J. L.; Tawfik, D. S.; Fleishman, S. J., Automated Structure- and Sequence-Based Design of Proteins for High Bacterial Expression and Stability. *Mol Cell* **2018,** *70* (2), 380.

93. Fleishman, S. J.; Leaver-Fay, A.; Corn, J. E.; Strauch, E. M.; Khare, S. D.; Koga, N.; Ashworth, J.; Murphy, P.; Richter, F.; Lemmon, G.; Meiler, J.; Baker, D., RosettaScripts: a scripting language interface to the Rosetta macromolecular modeling suite. *PLoS One* **2011,** *6* (6), e20161.

94. Whitehead, T. A.; Chevalier, A.; Song, Y.; Dreyfus, C.; Fleishman, S. J.; De Mattos, C.; Myers, C. A.; Kamisetty, H.; Blair, P.; Wilson, I. A.; Baker, D., Optimization of affinity, specificity and function of designed influenza inhibitors using deep sequencing. *Nat Biotechnol* **2012,** *30* (6), 543-8.

95. Chen, W.; Qu, M.; Zhou, Y.; Yang, Q., Structural analysis of group II chitinase (ChtII) catalysis completes the puzzle of chitin hydrolysis in insects. *J Biol Chem* **2018,** *293* (8), 2652-2660.

96. Magnusson, A. O.; Szekrenyi, A.; Joosten, H. J.; Finnigan, J.; Charnock, S.; Fessner, W. D.,

nanoDSF as screening tool for enzyme libraries and biotechnology development. *FEBS J* **2019,** *286* (1), 184-204.

97. Yoshida, S.; Hiraga, K.; Takehana, T.; Taniguchi, I.; Yamaji, H.; Maeda, Y.; Toyohara, K.; Miyamoto, K.; Kimura, Y.; Oda, K., A bacterium that degrades and assimilates poly(ethylene terephthalate). *Science* **2016,** *351* (6278), 1196-9.

98. Payne, C. M.; Knott, B. C.; Mayes, H. B.; Hansson, H.; Himmel, M. E.; Sandgren, M.; Stahlberg, J.; Beckham, G. T., Fungal cellulases. *Chem Rev* **2015,** *115* (3), 1308-448.

99. Nakamura A., I. D., Visootsat A., Uchiyama T., Mizutani K., Kaneko S., Murata T., Igarashi K., Iino R. (in press), Domain architecture divergence leads to functional divergence in binding and catalytic domains of bacterial and fungal cellobiohydrolases. *J Biol Chem* **2020**.

100. Austin, H. P.; Allen, M. D.; Donohoe, B. S.; Rorrer, N. A.; Kearns, F. L.; Silveira, R. L.; Pollard, B. C.; Dominick, G.; Duman, R.; El Omari, K.; Mykhaylyk, V.; Wagner, A.; Michener, W. E.; Amore, A.; Skaf, M. S.; Crowley, M. F.; Thorne, A. W.; Johnson, C. W.; Woodcock, H. L.; McGeehan, J. E.; Beckham, G. T., Characterization and engineering of a plastic-degrading aromatic polyesterase. *Proc Natl Acad Sci U S A* **2018,** *115* (19), E4350-E4357.

Acknowledgement

This thesis summarizes my Ph.D. research from October 2017 to May 2020 at the IINO-Group, Department of Functional Molecular Science, School of Physical Science, The Graduate University for Advanced Studies (SOKENDAI) under the supervision of Professor IINO Ryota with the support from The Ministry of Education, Culture, Sports, Science, and Technology (MEXT) of Japan.

First of all, I would like to appreciate and gratefully thank my advisor, Professor IINO Ryota, for the greatest opportunity he gave me since my internship in IMS (IMS-IIPA, September 2015 – January 2016) and also his advice, patience, and continuous support for my Ph.D. study and research. I also would like to thank Associate Professor NAKAMURA Akihiko (Assistant Prof. during my Ph.D.) for his kindly advice and helping in my Ph.D. research. I could not imagine how I can survive my Ph.D. life without both of them.

I especially would like to thank all of the lab members in IINO Group; Assistant Prof. ANDO Jun, Dr. KAWAI Fumihiro, Dr. TAKEDA Kimitoshi, Dr. OTOMO Akihiro, OKUNI Yasuko, YAMAMOTO Mayuko, NAKANE Kaori, and IIDA Tatsuya, for encouraging me and their kindly support during I stayed in Japan. I would also like to thank all international internship students in our lab for their supports and great friendship during their stays; VIGNON Paul, BOORLA Veda Sheersh, MOHAMAD ZAKARIA Siti Mastura Binti, WANG Tak-Wai, YANG Ling, and HONSA Monique.

I am indebted to Professor UCHIHASHI Takayuki (Nagoya University) and Dr. WATANABE Hiroki (EXCELLS) for their kindly providing the instruments and advice in conducting HS-AFM experiments.

I would like to thank all of my friends for their cheerful, helpful, support and friendship

during I stay in Japan; Dr. JONGWOHAN Chanantida, Ms. HIRANYAKORN Methanee, Dr. CHOOPPAWA Tianchai, Dr. GUANSHUO Shen, Ms. RATTANAJEARAKUL Nawarattana (NIPS), Dr. ZENG Chih Wei (NIBB), ISHIWATA Daiki and all of the internship student in IMS-IIPA program.

I would like to thank my previous supervisor; Associate Prof. PANJAWORAYAN T. THIENPRASERT Nattanan (Biochemistry, Science, Kasetsart University), for her advice and cheerful.

Last but not least, this Ph.D. would not achieve if there were no supports from my FAMILY. Thanks to my SUPERMOM for giving birth and always supporting me throughout the way I choose. I would like to dedicate this Ph.D. thesis to her.

VISOOTSAT Akasit

June 2020

List of Publications

Publications related to PhD Thesis

1. Visootsat A, Nakamura A, Vignon P, Watanabe H, Uchihashi T, *Iino R

   Single-molecule imaging analysis reveals the mechanism of a high-catalytic-activity mutant of chitinase A from *Serratia marcescens*

   J Biol Chem 295, 1915-1925 (2020) DOI: 10.1074/jbc.RA119.012078

2. Kawai F, Nakamura A, Visootsat A, *Iino R

   Plasmid-based one-pot saturation mutagenesis and robot-based automated screening for protein engineering

   ACS Omega 3: 7715–7726 (2018) DOI: 10.1021/acsomega.8b00663

3. Visootsat A, Nakamura A, Wang TW, *Iino R

   Combined approach to engineer highly-active mutant of processive chitinase hydrolyzing crystalline chitin

   Submitted to ***ACS Omega***

Other publications

1. Ando J, Nakamura A, Visootsat A, Yamamoto M, Song C, Murata K, *Iino R

   Single-nanoparticle tracking with angstrom localization precision and microsecond time resolution

   Biophysical Journal 115: 2413-2427 (2018) DOI: 10.1016/j.bpj.2018.11.016

2. Nakamura A, Ishiwata D, Visootsat A, Uchiyama T, Mizutani K, Kaneko S, Murata T, Igarashi K, Iino R

   Domain architecture divergence leads to functional divergence in binding and catalytic domains of bacterial and fungal cellobiohydrolases".

   J Biol Chem (2020) published online DOI: 10.1074/jbc.RA120.014792

List of Presentations

Poster Presentations

2018

1. **Biophysical Society of Japan Chubu Branch Annual meeting** (Nagoya University, March 5th)

   Construction of recombinant expression system of a heterodimer kinesin-14 Kar3-Cik1/Vik1

   Akasit VISOOTSAT, Akihiko NAKAMURA, Jun ANDO, Ryota IINO

2. **Biophysical Society of Japan Annual meeting** (Okayama University, September 15th - 17th)

   Single-molecule fluorescence imaging analysis of *Serratia marcescens* ChitinaseA (*Sm*ChiA) Trp-active mutant

   Akasit VISOOTSAT, Paul VIGNON, Akihiko NAKAMURA, Ryota IINO

3. **Okazaki Conference** (Okazaki Conference Center, August 31st – September 2nd)

   Single-molecule fluorescence imaging analysis of *Serratia marcescens* ChitinaseA (*Sm*ChiA) Trp-active mutant

   Akasit VISOOTSAT, Paul VIGNON, Akihiko NAKAMURA, Ryota IINO

2019

1. **Biophysical Society of Japan Annual meeting** (Seagaia Convention Center, Miyazaki, September 24th – 26th)

   Kinetic parameters and reaction scheme of high and low activity mutants of *Serratia marcescens* chitinase A

   Akasit VISOOTSAT, Paul VIGNON, Akihiko NAKAMURA, Hiroki WATANABE,

Takayuki UCHIHASHI, Ryota IINO

2. **Molecular Engine Area meeting** (Kyushu University, Fukuoka, May 24th – 25th)

   Characteristics of high and low activity mutants of *Serratia marcescens* chitinase A

   Akasit VISOOTSAT, Paul VIGNON, Akihiko NAKAMURA, Hiroki WATANABE, Takayuki UCHIHASHI, Ryota IINO

3. **The 2nd NIBB-Princeton Joint Symposium "Imaging and Quantitative Biology"** (Okazaki Conference Center, October 28th – 30th)

   The mechanism of *Serratia marcescens* chitinase A high activity mutant revealed by single-molecule analysis

   Akasit VISOOTSAT, Paul VIGNON, Akihiko NAKAMURA, Hiroki WATANABE, Takayuki UCHIHASHI, Ryota IINO

4. **2019 Japan-Korea Molecular Science Symposium** (Hotel Sunroute Plaza, Nagoya, July 29th - 31st)

   Processive reaction scheme of high and low activity mutants of *Serratia marcescens* chitinase A

   Akasit VISOOTSAT, Paul VIGNON, Akihiko NAKAMURA, Hiroki WATANABE, Takayuki UCHIHASHI, Ryota IINO

2020

1. **Molecular Engine Area meeting** (Chiba University, January 9th – 10th)

   Single-molecule imaging analysis reveals the mechanism of a high-catalytic-activity mutant of chitinase A from *Serratia marcescens*

   Akasit VISOOTSAT, Paul VIGNON, Akihiko NAKAMURA, Hiroki WATANABE, Takayuki UCHIHASHI, Ryota IINO

Oral Presentation

2019

1. **Biophysical Society of Japan Chubu Branch Annual meeting** (Okazaki Conference Center, March 26th)

   Biochemical and single-molecule imaging analyses of high and low activity mutants of *Serratia marcencens* chitinase A

   Akasit VISOOTSAT, Paul VIGNON, Akihiko NAKAMURA, Hiroki WATANABE, Takayuki UCHIHASHI, Ryota IINO